Nuclear magnetic moment of neutron-rich nucleus ^{21}O

Yoko Ishibashi

February 2019

Nuclear magnetic moment of neutron-rich nucleus ^{21}O

Yoko Ishibashi

Submitted to the Graduate School of
Pure and Applied Sciences
in Partial Fulfillment of the Requirements
for the Degree of Doctor of Philosophy in
Science

at the
University of Tsukuba

Abstract

The nuclear structure in stable nuclei is well understood, and nuclei become spherical and stable when protons and neutrons take a "magic number". However, recent studies have reported that magic numbers disappear in areas of light neutron-rich nuclei and new magic numbers appear. Further, nuclei with unique structures, such as nuclear deformation and spin anomalies, have been discovered. Oxygen isotopes suitable for investigating the effect of neutrons that ignore the effect of proton number Z because $Z = 8$ are suitable for nuclear structure studies. In this study, we systematically investigated the nuclear structure of the ^{21}O nucleus, which is a stable line.

The β-ray detected nuclear magnetic resonance (β-NMR) method is useful for measuring the nuclear magnetic moment, for which it requires a spin-polarized radioactive isotope (RI) beam. Prior to the magnetic moment measurement, nuclear spin polarization was measured using the adiabatic field rotation (AFR) method. In the AFR method, it is possible to measure the degree of polarization without a frequency search; thus, the parameters (e.g., emission angle, momentum selection, measurement sequence, target thickness) required to produce polarization can be optimized beforehand. Therefore, we can focus on frequency search under optimum polarization and yield conditions. The newly developed AFR device can reversely rotate a permanent Nd magnet ($B_0 \sim 500$ mT) mechanically using a Halbach array; thus, it is possible to invert the nuclear spin adiabatically. A nuclear spin polarization of ^{21}O was produced using the projectile fragmentation reaction and nucleon pick-up reaction. Spin-polarized ^{21}O beams were implanted into the CaO crystal placed in the static magnetic field, polarization is measured by performing AFR measurement. In the case of ^{21}O, the asymmetry parameter can only obtain the upper limit value and the lower limit value because there are excitation levels where the spin of the daughter nucleus ^{21}F is not decided. Therefore, $|P| > 4.9\%$ is the lower limit value, which can potentially yield even greater polarization.

Furthermore, ^{21}O has no determined spin, and it is necessary to search across a wide range of resonance frequencies when performing β-NMR. Therefore, we improved the efficiency of the resonant frequency search by introducing a fast switching system. In the proposed system, the number of variable capacitors in the LCR circuit can be increased from one to three, capacitors can be switched sequentially using the relay circuit, and a single wide frequency search can be performed. Therefore, the introduction of this system is very useful to perform the measurement efficiently in a limited time.

By introducing these systems, we successfully measured the ground-state magnetic moment of ^{21}O for the first time. From the obtained resonance frequency, the g-factor of the ground state of ^{21}O was $|g_{\mathrm{exp}}| = 0.6036 \pm 0.0014$. Experimental results indicating $I^{\pi}(^{21}\mathrm{O}_{\mathrm{g.s.}}) = 5/2^{+}$ have been reported; however, that result has not been determined. Then, the g factors corresponding to two possible configurations, i.e., $|[(sd)^4]^{0^+}(d_{5/2})\rangle^{I^{\pi}=5/2^+}$ and $|[(sd)^4]^{0^+}(s_{1/2})\rangle^{I^{\pi}=1/2^+}$, calculated

using the effective g factors are given as $g_{\rm eff}(d_{5/2}) = -0.729$ and $g_{\rm eff}(s_{1/2}) = -3.449$, respectively. Although a sign was not assigned to the experimental g factor determined in the present study, we can definitely assign $I^\pi = 5/2^+$ to the ^{21}O ground state even only from the comparison of the absolute value to the effective g factors values, due to the large difference (as much as 4.6 fold) in $g_{\rm eff}(d_{5/2})$ and $g_{\rm eff}(s_{1/2})$. Now that we are certain that the $I^\pi(^{21}{\rm O}_{\rm g.s.})$ is $5/2^+$, the ground-state nuclear magnetic moment of ^{21}O can be determined as $|\mu_{\rm exp}(^{21}{\rm O}_{\rm g.s.})| = (1.5090 \pm 0.0035)\ \mu_{\rm N}$. Furthermore, considering the ambiguity of 0.1 $\mu_{\rm N}$ due to the accuracy of the effective g-factor, the magnetic moment $\mu_{\rm SM} = -1.41\ \mu_{\rm N}$ obtained using shell model calculation and magnetic moment $\mu_{\rm RPA(D1M)} = -1.487\ \mu_{\rm N}$ obtained using random phase approximation (RPA) calculation were consistent with the experimental results. From these results, I^π of the ground state of ^{21}O was $5/2^+$, and ^{21}O was found to be a "normal" nucleus.

Contents

List of Figures

List of Tables

Chapter 1

Introduction

1.1 Structure of neutron-rich oxygen isotopes

Nuclei, which exist at the center of an atom, comprise protons and neutrons. Depending on the combination of protons and neutrons, nuclei demonstrate various features. For example, with a certain "magic number" of protons and neutrons, nuclei become spherical and stable. Currently, for naturally existent nuclei, the magic numbers are 2, 8, 20, 28, 50, 82, and 126. For approximately half a century, magic numbers have been considered a universal constant in the fundamental law of physics that is used to explain material formation. However, recent studies using radioactive isotope (RI) beams have obtained data that overturn the theory that the magic number remains unchanged. Figure 1.1 shows a nuclear chart with magic number [1]. With some RIs, magic numbers disappear in the region of light neutron-rich nuclei and new magic numbers appear [2, 3]. This implies that all known and conceptual nuclide are arranged with proton number Z on the vertical axis and neutron number N on the horizontal axis. In Fig. 1.1, the black and white squares represent stable and unstable nuclei,respectively. In this figure, new magic numbers ($N = 6, 16, 32, 34$) are reported in neutron-rich regions.

A nucleon enters a discontinuous energy orbit in terms of quantum mechanics. A group of orbits close to the energy between these orbits is referred to as a shell, and the number of nucleons differs from shell to shell. The magic numbers appear at places where the energy between shells is large. New magic numbers are thought to appear owing to change in the energy of a specific orbit and shell structure.

In our group, because it has the magic number $Z = 8$, we focused on the oxygen isotopes that are suitable for investigating the effect of neutrons while ignoring the effect of the proton number Z. Figure 1.2 shows a partial nuclear chart around oxygen isotopes. In the oxygen isotopes, ^{24}O with $N = 16$ as the new magic number is the nucleus of the neutron drip line. However, in a fluorine isotope with one proton added to the oxygen, the neutron drip line moves to ^{31}F of $N = 22$ [4]. The gap energy spread of $N = 16$ is due to the widening energy gap of $1s_{1/2}$ and $0d_{3/2}$ neutron orbits. How these orbital energies change is important relative to the prediction of the position of the neutron drip line and the characteristics of nuclei beyond the neutron drip line.

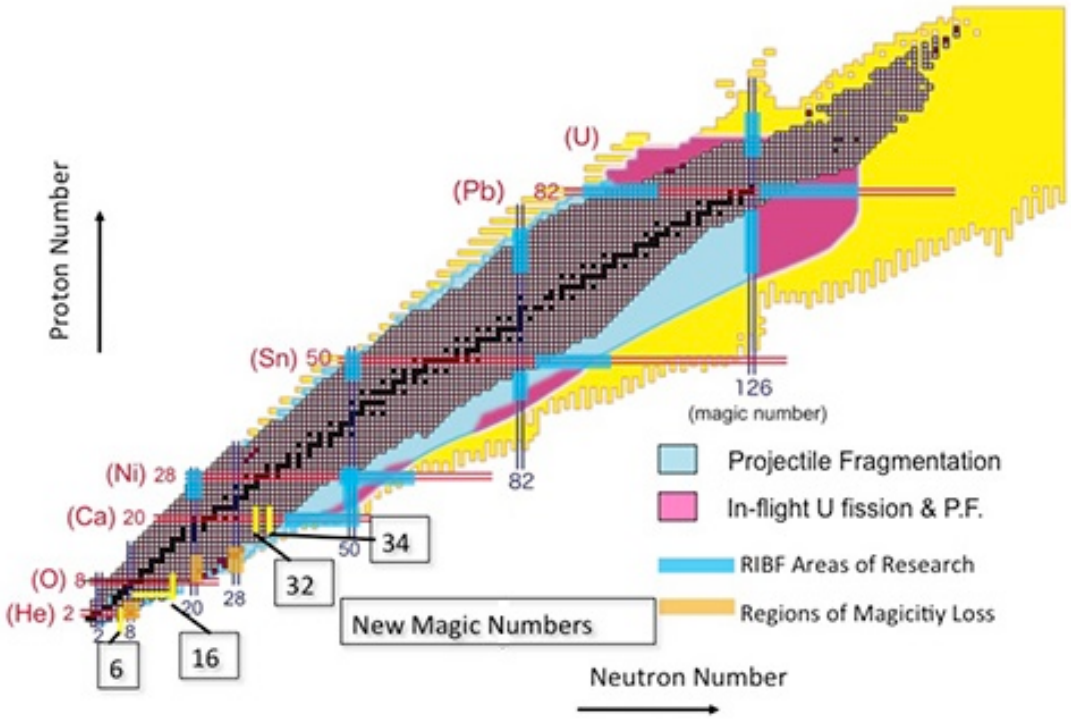

Figure 1.1: View of the nuclear chart with traditional and new magic numbers.

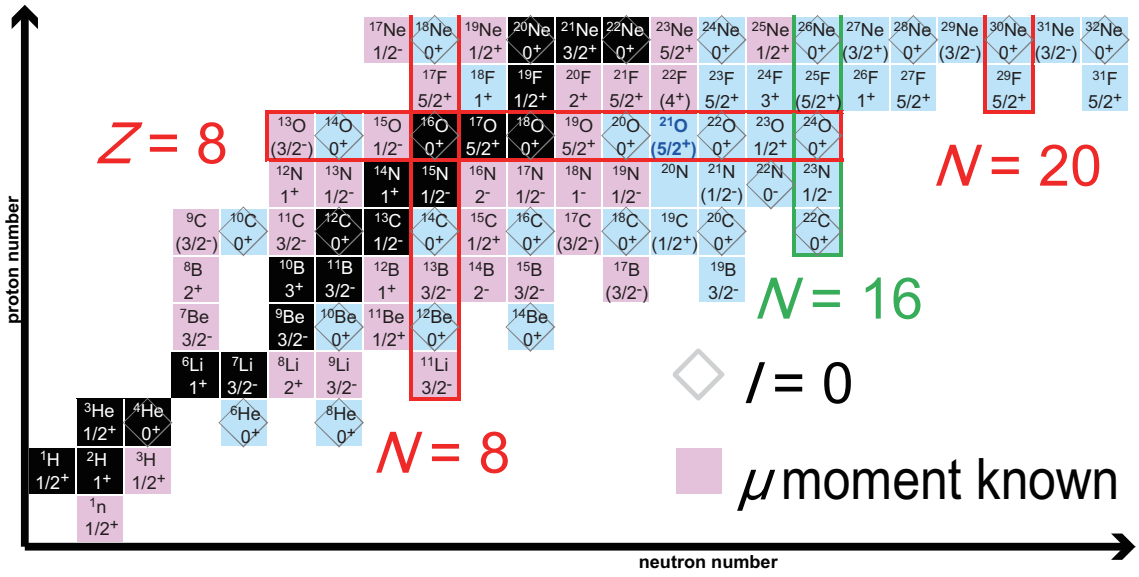

Figure 1.2: The nuclear chart around oxygen isotopes with its spin-parity of ground state. Red squares are the nuclei that a magnetic moment is known and blue ones are the unknown nuclei. The nuclei in which the diamond are written inside, the spin of the ground state is 0 and it has no magnetic moment.

The gaps with $N = 16$ open at low Z and are predicted to evolve with the oxygen isotopes [5, 6, 7]. This is evident in the interaction of both USD [5] and SDPF-M [7]; however, the gap size is significantly larger in the latter. The only experimental estimates of this gap are provided by a ^{23}O measurement using the ^{22}O(d,p) transfer reaction [8], which favors the USDA interaction [6] (a modified version of the USD interaction), and a measurement of the ground state in ^{25}O [9], which agrees with the USD calculations that predict ^{26}O to be bound, which contradicts previous experimental results [10].

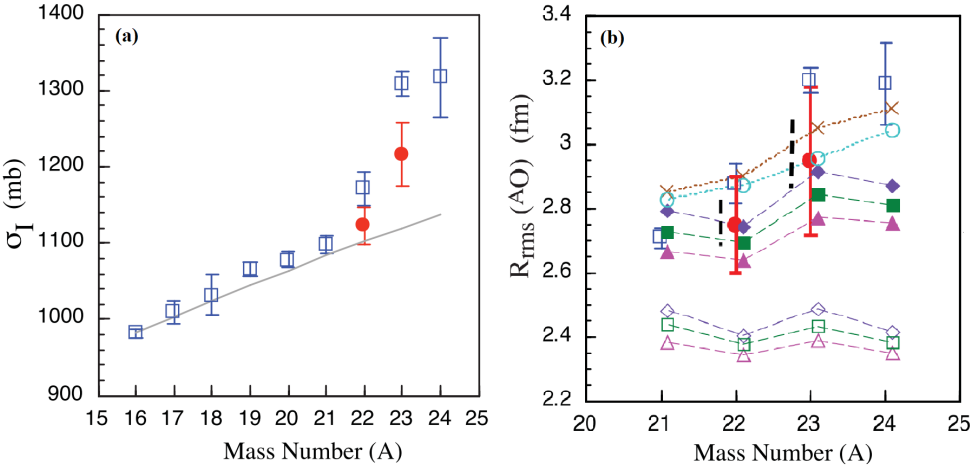

Figure 1.3: (a) Interaction cross section of ^{A}O + C as a function of the mass number. The circles are from Ref. [12] and the squares are from Ref. [11]. The line shows the $A^{1/3}$ dependence normalized to ^{16}O. (b) Matter radii of the oxygen isotopes. The diamond/square/triangle indicates coupled-cluster calculation with a cutoff parameter = 4.0/3.8/3.6 fm-1. Here, filled point is $R_{\rm rms}$, open point is proton rms radii. (Taken from Ref. [12])

Figure 1.3(a) shows the measurement result of the interaction cross section of oxygen isotope ($E/A \sim 900$ MeV) ^{A}O + C [10]. The squares represent data measured in 2001 [11], and the circles represent 2011 measurements [12]. The solid line is an $A^{1/3}$ line normalized with ^{16}O. Figure 1.3(b) shows the matter radii of the oxygen isotope, where the diamonds, squares, and triangles indicate coupled-cluster calculations with cutoff parameters of 4.0, 3.8, and 3.6 fm-1, respectively. Here, the filled point is $R_{\rm rms}$ and the open point is the proton rms radii. This result indicates the neutron skin grows as the mass number increases. Although no subsequent remeasurement has been conducted, further investigation is required because a large cross section has been observed for ^{24}O. In fact, since the size of the gap of $N = 16$ depends relatively weakly on the number of neutrons, it is possible to obtain more detailed information by examining the more easily accessible nucleus (e.g. ^{21}O).

Figure 1.4 shows the nuclear moment of the oxygen isotope. The magnetic moments measured to date are ^{13,15,17,19}O and the Q moment is ^{13,17,19}O. From the Q moment of ^{19}O, it is evident that the value is small, and it is a normal nucleus. Nuclear moment is very sensitive to internal structure; thus it may be possible to discover spin abnormalities and nuclear deformations. Therefore, measuring the nuclear moment of ^{21,23}O becomes important relative to discussion of nuclear structure.

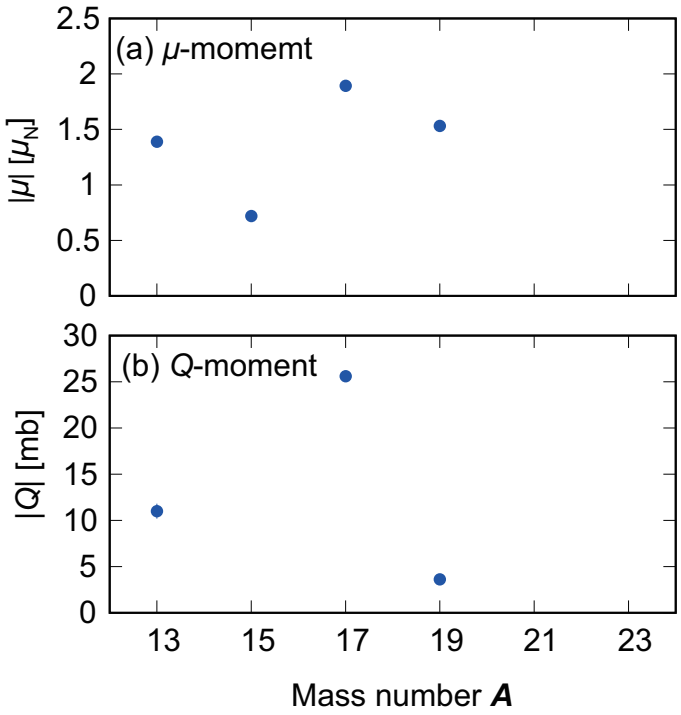

Figure 1.4: (a) Nuclear magnetic moment of oxygen isotopes, and (b) electric quadrupole moments of the oxygen isotope

The ^{21}O nucleus has $N = 13$, and the spin is expected to be $I^{\pi} = (5/2)^{+}$. As shown in Fig. 1.5, the expected coordination is five valence neutrons enter the $d_{5/2}$ orbital with ^{16}O as the core. From Fig. 1.2, looking at the isotone of $N = 13$, ^{23}Ne ($Z = 10$) is $I^{\pi} = 5/2^{+}$, while ^{19}C ($Z = 6$) is predicted to be $I^{\pi} = (1/2)^{+}$. It is considered that the $d_{5/2}$ and $s_{1/2}$ orbitals are reversed between ^{19}C and ^{23}Ne. Further, we are interested in where this reversal begins. Therefore, we measured the ^{21}O which is located in the middle and the magnetic moment is unknown.

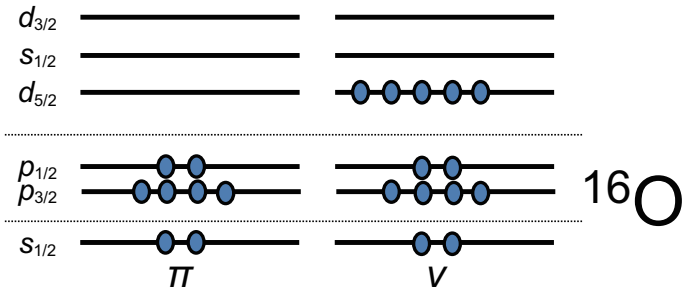

Figure 1.5: Configuration in the ^{21}O ground state. The expected configuration is five valence neutrons enter the $d_{5/2}$ orbital with ^{16}O as the core.

1.2 Nuclear electromagnetic moment

The nuclear electromagnetic moment is a physical quantity that functions as an important probe when investigating nuclei structures because nuclear electromagnetic measurements reveal information regarding nuclear spin, shape, and configuration. In particular, the magnetic dipole moment described in the following text is a physical quantity that is sensitive to the orbital angular momentum and spin of nuclei, and the electric quadrupole moment is a physical quantity that is sensitive to nuclei deformation. Therefore, by measuring the nuclear electromagnetic moment, it is possible to identify the structure and shape inside the nucleus microscopically. The interaction energy between the electromagnetic field and nucleus is expressed as follows:

$$H_{\rm em} = \int \rho(\boldsymbol{r})\phi(\boldsymbol{r})d\boldsymbol{r} - \frac{1}{c}\int \boldsymbol{j}(\boldsymbol{r})\cdot\boldsymbol{A}(\boldsymbol{r})d\boldsymbol{r} \tag{1.1}$$

Here, $\rho(\boldsymbol{r})$ and $\boldsymbol{j}(\boldsymbol{r})$ are charge and current density, respectively. $\phi(\boldsymbol{r})$ and $\boldsymbol{A}(\boldsymbol{r})$ are the scalar and vector potential describing the electromagnetic field, respectively. Expanding this $H_{\rm em}$ around the origin $\boldsymbol{r} = 0$ yields:

$$H_{\rm em} = q\phi(0) - \boldsymbol{P}\cdot\boldsymbol{E}(0) - \boldsymbol{\mu}\cdot\boldsymbol{B}(0) - \frac{1}{6}\sum_{ij} Q_{ij}\left(\frac{\partial E_j}{\partial x_i}\right)_0 + \cdots \tag{1.2}$$

Here, q, $\boldsymbol{P}$, $\boldsymbol{\mu}$, and Q_{ij} denote a nuclear charge, an electric-dipole moment vector, a magnetic moment vector and an electric quadrupole tensor, respectively, and are given as follows:

$$\begin{aligned} q &= \int \rho(\boldsymbol{r})d\boldsymbol{r}, \\ \boldsymbol{P} &= \int \rho(\boldsymbol{r})\boldsymbol{r}d\boldsymbol{r}, \\ \boldsymbol{\mu} &= \frac{1}{2c}\int \boldsymbol{r}\times\boldsymbol{j}(\boldsymbol{r})d\boldsymbol{r}, \\ Q_{ij} &= \int \rho(\boldsymbol{r})(3x_ix_j - \sigma_{ij}\boldsymbol{r}^2)d\boldsymbol{r}. \end{aligned} \tag{1.3}$$

1.2.1 Nuclear magnetic moment

The nuclear magnetic dipole moment is determined by the current distribution in the nucleus. In the single particle model, the spin, parity, and magnetic moment of a nucleus the mass number of which is odd, are determined from the spins and parities of the remaining outermost shell nuclei when an even number of protons and neutrons develop an angular momentum of 0. Using nuclear magneton $\mu_{\rm N}$, nuclear spin, and g-factor, the magnetic moment μ of nuclei in a single particle model can be expressed as follows:

$$\begin{aligned} \boldsymbol{\mu} &= g\mu_{\rm N}\boldsymbol{I}, \\ \mu_{\rm N} &= \frac{e\hbar}{2M_{\rm p}c}. \end{aligned} \tag{1.4}$$

Here, e is the elementary charge, $\hbar$ is the Dirac constant, M_{p} is the rest mass of the proton, and c is the speed of light. In this experiment, the magnetic moment is calculated using Eq. 1.5 when nuclear spin is found by measuring the g factor. We can consider the physical properties of nuclei by determining the magnetic moment.

Using the orbital angular momentum $\boldsymbol{l}$ of the nucleon and the intrinsic nuclear spin $\boldsymbol{s}$, nuclear spin I can be expressed as follows:

$$\boldsymbol{I} = \boldsymbol{j} = \boldsymbol{l} + \boldsymbol{s}. \tag{1.5}$$

If the orbital angular momentum of the nucleon and the g factor in the intrinsic nucleon spin are g_l and g_s, respectively, the magnetic moment can be expressed as follows:

$$\boldsymbol{\mu} = (g_l \boldsymbol{l} + g_s \boldsymbol{s})\, \mu_{\mathrm{N}} \tag{1.6}$$

From Eqs. 1.5 to 1.6, $g\boldsymbol{j}$ is given by

$$g\boldsymbol{j} = g_l \boldsymbol{l} + g_s \boldsymbol{s}. \tag{1.7}$$

Here, when sorting out using $s = 1/2$ and $j = \pm 1/2$, g can be expressed as follows:

$$\begin{aligned} g &= \frac{g_l \boldsymbol{l}\cdot\boldsymbol{j} + g_s \boldsymbol{s}\cdot\boldsymbol{j}}{\boldsymbol{j}\cdot\boldsymbol{j}} \\ &= \frac{1}{2}(g_l + g_s) + \frac{l(l+1) - s(s+1)}{2j(j+1)}(g_l - g_s) \\ &= g_l \pm \frac{g_s - g_l}{2l+1}. \end{aligned} \tag{1.8}$$

Where, g_l, g_s take different values for protons and neutrons.

$$g_l = \begin{cases} 1 & (\text{proton}) \\ 0 & (\text{neutron}) \end{cases}, g_s = \begin{cases} 5.58569478(14) & (\text{proton}) \\ -3.8260855(9) & (\text{neutron}) \end{cases} \tag{1.9}$$

Note that the value obtained by Eq. 1.8 is referred to as the Schmidt value. The magnetic moment of nucleus whose nucleon number is the magic number and magic number ± 1 can be well represented by the Schmidt value. However, with an unstable nucleus distant from the closed shell, there are many cases where the magnetic moment value cannot be explained by a single particle model. In this case, the wave function of the entire nucleus must be represented using a linear combination of multiple nucleon configurations, which is referred to as configuration mixing. In such a case, the Schmidt value, which is the predicted value of the single particle model and the g-factor which is observed in the experiment are deviated. By comparing the experimental and Schmidt values, it can be confirmed that configuration mixing occurs in the shell structure of the nucleus. On the other hand, some g-factor measurement results can determine spin and parity. This is due to the fact that g-factor has orbital angular momentum and spin sensitive responses of valence nucleon. Thus, the magnetic moment is an important physical quantity when investigating structures that characterize individual nuclear properties.

1.2.2 Nuclear electric quadrupole moment

The nuclear electric quadrupole moment is a physical quantity representing deviation in the charge distribution of the nucleus from the spherical shape.The electric-quadrupole moment shows deformation of the nucleus, particularly deformation of the proton distribution. Here, for simplicity, consider a nucleus in which the charge of Z_e is distributed uniformly and is symmetrical around the space-fixed z-axis. The charge density can be expressed as follows.

$$\rho = \frac{Z_e}{V}. \tag{1.10}$$

Here $V = 4\pi a^2 b/3$ is the volume of the nucleus, where a and b denote the length of the z axis and the axis of perpendicular to z axis, respectively. From $r^2 = x^2 + y^2 + z^2$,

$$Q = \frac{\rho}{e} \int \left\{ 3z^2 - (x^2 + y^2 + z^2) \right\} dV. \tag{1.11}$$

When Eq. 1.11 is calculated by introducing the cylindrical coordinate system (R, θ, z) as

$$\left\{ \begin{array}{lcl} x & = & R\cos\theta \\ y & = & R\sin\theta \\ z & = & z \end{array} \right. , \tag{1.12}$$

it becomes

$$\begin{aligned} Q &= \frac{\rho}{e} \int \left(2z^2 - R^2 \right) dV \\ &= \frac{4\pi\rho}{e} \int_{-b}^{b} dz \int_{0}^{r} R \left(z^2 - \frac{R^2}{2} \right) dR \\ &= \frac{4\pi\rho}{e} \int_{-b}^{b} \left(\frac{z^2 r^2}{2} - \frac{r^4}{8} \right) dz, \end{aligned} \tag{1.13}$$

where $r = \sqrt{a^2 - (a/b)^2 z^2}$. Then,

$$\begin{aligned} Q &= \frac{2}{15} \frac{4\pi\rho}{e} \left(a^2 b^3 - a^4 b \right) \\ &= \frac{2}{5} Z \left(b^2 - a^2 \right). \end{aligned} \tag{1.14}$$

From Eq. 1.14, it is evident that the nucleus is a spheroid when $Q \neq 0$. If $Q > 0$, then $b > a$. Conversely if $Q < 0$, then $b < a$. In other words, if $Q > 0$, nuclei are prolate deformation, and if $Q < 0$, nuclei are oblate deformation. Here, we considered the charge distribution of the nucleus, i.e., the proton distribution. However, there is a strong attractive force between neutrons and protons, and if one of the distributions is deformed, it is conceivable that the other distribution is also deformed. Therefore, the electric quadrupole moment is a static observation quantity representing nuclei deformation.

To this point, the discussion has assumed that the charge distribution is symmetrical. However, in an actual nucleus, the charge distribution is not necessarily symmetric with respect to the spatial

fixed z axis. Therefore, assuming that the charge distribution of the nucleus is symmetrical with respect to the newly set rotational symmetric axis z' axis. Considering that the charge distribution rotates around the space-fixed z axis, we consider the physical meaning of the electric-quadrupole moment. At this time, let the z' axis be the quantization axis of nuclear spin I.

Here, the electric-quadrupole moment operator can be defined as follows.

$$\begin{aligned} \hat{Q} &= \sum_{k=1}^{Z} r_k^2 Y_2^0(\theta, \phi) \\ &= \sqrt{\frac{5}{16\pi}} \sum_k r_k^2 \left(3\cos^2\theta_k - 1\right) \end{aligned} \tag{1.15}$$

However, (r, θ, ϕ) represents polar coordinates, and $Y_2^0(\theta, \phi)$ is a spherical harmonic function. In this paper, the electric-quadrupole moment Q is the expected value in state $|I, m = I>$ and is defined as follows.

$$\begin{aligned} Q(I) &= \sqrt{\frac{5}{16\pi}} < I, m = I|\hat{Q}|I, m = I > \\ &= \sum_{k=1}^{Z} \int r_k^2 \left(3\cos^2\theta_k - 1\right) |\Phi_{Im}|^2 dV \end{aligned} \tag{1.16}$$

Here, m is the eigenvalue of the projection component I_z in the z direction of I, and Φ_{Im} is the wave function representing the quantum state $|I, m>$ of the nucleus. First, Q is calculated from the Eq. 1.3 with respect to the z axis as follows:

$$\begin{aligned} Q &= \int \left(3z^2 - r^2\right) \rho dV \\ &= \int \left(3\cos^2\theta - 1\right) r^2 \rho dV. \end{aligned} \tag{1.17}$$

Here, the integral variable is converted from (r, θ, ϕ) to (r', θ', ϕ').

$$\cos\theta = \cos\theta' \cos\beta + \sin\theta' \sin\beta \cos\left(\phi' - \varphi\right) \tag{1.18}$$

Here, the z' axis is assumed to point in the direction of $\theta = \beta, \phi = \varphi$. Substituting Eq. 1.18 into Eq. 1.17, Q becomes as shown below:

$$Q = \int \left[3\left(\cos^2\theta' \cos^2\beta + \sin^2\theta' \sin^2\beta \cos^2\left(\phi' - \varphi\right) + 2\cos\theta' \cos\beta \sin\theta' \sin\beta \cos\left(\phi' - \varphi\right)\right) - 1\right] r^2 \rho dV' \tag{1.19}$$

Considering that ρ is not dependent on ρ', the integral of $\int_0^{2\pi} \cdots d\phi'$ can be performed immediately, and the third term of the integrand of Eq. 1.19 becomes zero. Given that $\int_0^{2\pi} \cos^2\left(\phi' - \varphi\right) d\phi' = \frac{1}{2}\int_0^{2\pi} d\phi'$, Q is expressed as follows.

$$\begin{aligned} Q &= \int \left[3\left(\cos^2\theta' \cos^2\beta + \frac{1}{2}\sin^2\theta' \sin^2\beta\right) - 1\right] r^2 \rho dV' \\ &= \frac{1}{2}\left(3\cos^2\beta - 1\right) \int \left(3\cos^2\theta' - 1\right) r^2 \rho dV' \\ &= \frac{1}{2}\left(3\cos^2\beta - 1\right) Q_0 \end{aligned} \tag{1.20}$$

Here, Q_0 is the value of Q when the z' axis coincides with the z axis. In quantum theory, m takes a discrete value and becomes $\cos\beta = m/\sqrt{I(I+1)}$. Therefore, using Eqs. 1.16 and 1.20, the relationship between Q and different m is obtained:

$$\begin{aligned}\frac{Q\,(m=m_1)}{Q\,(m=m_2)} &= \frac{<I,m_1|\hat{Q}|I,m_1>}{<I,m_2|\hat{Q}|I,m_2>} \\ &= \frac{3\cos^2\beta_1 - 1}{3\cos^2\beta_2 - 1} \\ &= \frac{3m_1^2 - I(I+1)}{3m_2^2 - I(I+1)} \end{aligned} \tag{1.21}$$

In particular, when $m_2 = I$, the following is obtained.

$$\begin{aligned} Q(m) &= \frac{3m^2 - I(I+1)}{I(2I-1)}Q(I) \\ Q(I) &= \frac{2I-1}{2(I+1)}Q_0 \end{aligned} \tag{1.22}$$

In the actual measurement, Q_0 defined in the direction of nuclear spin is not directly observed, Q is observed with $\frac{2I-1}{2(I+1)}$. This occurs due to the uncertainty of vector $\boldsymbol{I}$ from quantum mechanical uncertainty.

1.2.3 Nuclear electromagnetic moment measurements of far-unstable nuclei

The nuclear electromagnetic moment is a fundamental observation that reflects the structure of stable nuclei i.e., energy, spin, and parity. However, few studies have investigated unstable nuclei. In particular, the magnetic moment has a feature that reflects the configuration of nucleons in a single particle state in a shell model and the way of their configuration mixing sharply. In Fig. 1.2, the red and blue squares indicate nuclei where the magnetic moment is known and unknown, respectively. In addition, diamonds indicate that the spin of the ground state is 0 and has no magnetic moment. As can be seen, some of the unstable nuclei have unknown magnetic moments. Despite the development of unstable nuclear beam production technology, the production of neutron-rich nuclei distant from the stable line is difficult because the cross section is very small. For such neutron-rich nuclei, it is difficult to apply a conventional polarization method. For example, it is impossible to produce nuclei distant from the stable line with polarized production by recoil, as in a (d, p) reaction at low energy. In the optical pumping method, the nuclear moment of ^{11}Li distant from the stable line could be measured: however, the optical pumping method cannot be applied to isotopes of elements other than alkali metals. It is difficult to apply unstable nucleus production and polarization production, simultaneously; thus it is difficult to apply above methods to a short-lived nucleus.

Therefore, a method to produce polarization by projectile fragmentation reaction has been developed to address these difficulties. This method has three advantages over the above method. The first is beam production by nuclear fragmentation reaction, such that any fragment can be produced and polarized independent of its physical and chemical properties. Second, the degree of polarization

is typically only a few percent; however it can sometimes exceed 10%, which is sufficient for nuclear moment measurement. Third, since the velocity of the fragment is close to the beam velocity, it can be produced with enough energy to deeply embed in the stopped sample. Therefore, the β-NMR method can be applied to nuclear moment measurement.

Chapter 2

Principles of Experiment

In this chapter, the principles of the method used in this research are described. First, we explain the method used to produce neutron-rich nuclei and the accompanying spin polarizations. Next, the β-NMR method will be described as a method of magnetic moment measurement for spin-polarized unstable nuclei. In the β-NMR method, if the magnetic moment of the unstable nucleus to be measured is unknown, spin polarization cannot be confirmed. Therefore, the adiabatic field rotation (AFR) method is employed to separate the nuclear spin operation and measure the degree of polarization. In addition, we describe the control of a fast switching system used to perform frequency sweeping over a wide range at the time of magnetic moment search.

2.1 Spin polarization in projectile fragmentation and nucleon pick-up reactions

In order to measure nuclear moments using the β-NMR method, it is essential to produce a spin-polarized ^{21}O beam. In this section, we describe the method to obtain spin-polarized fragments.

2.1.1 Projectile fragmentation reaction

The projectile fragmentation reaction produces an unstable nuclear beam by stripping the nucleus of the overlapping part of the projectiles and the target nucleus by bombarding the target with a heavy ion beam ($E/A > 30$ MeV). When projectiles accelerated to an intermediate energy of $E/A > 30$ MeV collide with a target nucleus, only the area in which nuclei geometrically overlap reacts and is stripped from the projectiles. This part can be considered a "participant" in the reaction. Here, the momentum of the nucleus accelerated to the intermediate energy becomes greater than the Fermi momentum of the nucleon in the nucleus. Therefore, collision time is less than the movement time of nucleons in the nucleus, and the crushed pieces of the remaining incoming nucleus can be approximated as "spectators" that do not participate in the reaction. As shown in Fig. 2.1, a significant feature of this fragmentation reaction is that the fragments continue to move at nearly the incident velocity. The number of nuclei stripped from the projectiles is given by the product of the volume of the geometrical overlap volume and the nucleon density, and, if the projectiles and

target nucleus are determined, it is determined by the collision parameter.

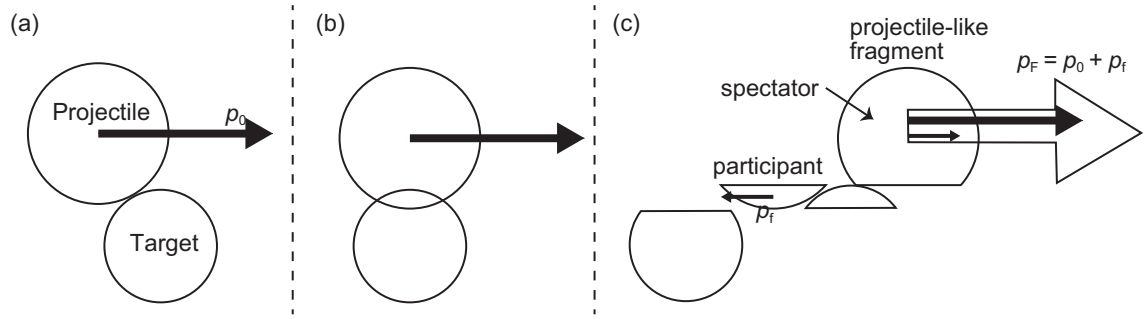

Figure 2.1: Schematic diagram of projectile fragmentation reaction; (a) Projectiles were made to bombard the target nucleus with momentum p_0. (b) Only the region where the projectile overlaps with the target nucleus reacts, and the other region does not participate in the reaction and moves; (c) the momentum is preserved in the whole system, the momentum p_F of the fragment represented by the white arrow is the difference between the momentum of the projectile and the momentum to be stripped. Here, an example in which the direction of the momentum to be peeled off is opposite the traveling direction is shown.

When the projectile fragmentation reaction occurs, the nucleon is removed instantaneously; therefore, the stripped nucleon brings out its original exercise amount. Since nucleons exhibit Fermi motion on a nuclear surface, the Fermi momentum also has distribution. The momentum of fragment p_F, which did not participate in the reaction, retains the exercise state produced at the time of stripping, and the fluctuation Δp of the internal motion in the nucleus of the fragment with momentum p_0 of the fragment corresponding with the incoming velocity has been added.

$$p_f = p_0 + \Delta p. \tag{2.1}$$

Assuming that the nucleus is extracted randomly from the projectile where the nucleon is moving independently, the distribution of Δp and its width σ can be obtained as follows.

$$f(p) = \exp\left(-\frac{(p-p_0)^2}{2\sigma_F^2}\right) \tag{2.2}$$

$$\sigma_F = \sqrt{\frac{A_f(A_p - A_f)}{A_p - 1}\sigma_0^2} \tag{2.3}$$

Here, A_f and A_p are the number of nucleons of the fragment and the nucleon number of the projectile, respectively. Also, σ_0 is the standard deviation of the momentum that the nucleon has in the nucleus. Similarly, considering that σ_0 is $1/\sqrt{5}$ of the Fermi momentum, it is experimentally found that $\sigma_0 \approx 90$ MeV/c. However, the momentum distribution is slightly different, i.e., the tail is drawn to the low energy side. On the low energy side, the one represented by a collision reaction, such as a projectile fragmentation reaction, and a complicated reaction occurring multiple times between nucleons in the nucleus at the time of collision, it is thought that the energy of fragments has decayed.

2.1.2 Production of spin-polarization

Spin polarization refers to a state in which the spin state of individual particles is biased toward a specific direction when viewed as a group. In the β-NMR method used for magnetic moment measurement, it is necessary to produce this spin polarization state because it uses emission angle distribution of β-rays depending on the spin direction of nuclei.

A method to produce spin polarization that uses the projectile fragmentation reaction has been developed [13]. This method can also be understood by a simple kinematic consideration, i.e., a nucleon with internal motion in the projectile (Section 2.1.1) is removed without affecting others.

When the projectile fragmentation reaction occurs, the stripped nucleus i removes the momentum $\boldsymbol{p}_i$ associated with the Fermi motion. Simultaneously, it takes away the angular momentum obtained by the outer product of the position vector $\boldsymbol{r}_i$ and $\boldsymbol{p}_i$ with the center of the projectile as the origin. Therefore, the angular momentum taken up by the entire stripped off nucleon can be expressed by the sum of these nucleons.

$$\boldsymbol{L}_{\text{participant}} = \sum_i (\boldsymbol{r}_i \times \boldsymbol{p}_i) \tag{2.4}$$

By the law of conservation of angular momentum, the fragment obtains angular momentum, i.e., the source of the spin polarization, as follows.

$$\boldsymbol{L}_{\text{participant}} = -\sum_i (\boldsymbol{r}_i \times \boldsymbol{p}_i) \tag{2.5}$$

From Eq. 2.5, the momentum distribution of the fragment, which is the same as the momentum distribution p_i of the stripped nucleon, directly represents the characteristic of the spin polarization degree, as shown in Fig. 2.2.

2.1.3 Near-side and Far-side orbitals

Spin polarization depends on the emission angle of the fragment in the reaction. Depending on which orbit of the target nucleus the projectile passes, the sign of fragment is reversed; thus even if each fragment is spin-polarized, polarization will cancel out as a whole. To prevent this, we must select what passed through one of the left and right orbits. To make this choice, the emission angle can be determined based on the slit on the downstream of the target.

Here, we consider scattering of fragments by the target nuclei. The potential of the target nucleus, which includes both nuclear and Coulomb forces, affects the scattering. When the target nucleus is heavy, i.e., the proton number Z is large, the repulsive force due to the Coulomb force dominates and the fragment is bent away from the target nucleus (a near-side orbit). Conversely, if the target nucleus is light, due to the nuclear force, i.e., the influence of gravitational attraction, the fragment is bent in a direction approaching the target nucleus, i.e., a far-side orbit. Since the type of orbit depends on the target nucleus, if the emission angle is selected, the one that passed the right or left orbit can be selected, as shown in Fig. 2.3. The emission angle distribution $W(\theta_{\text{L}})$

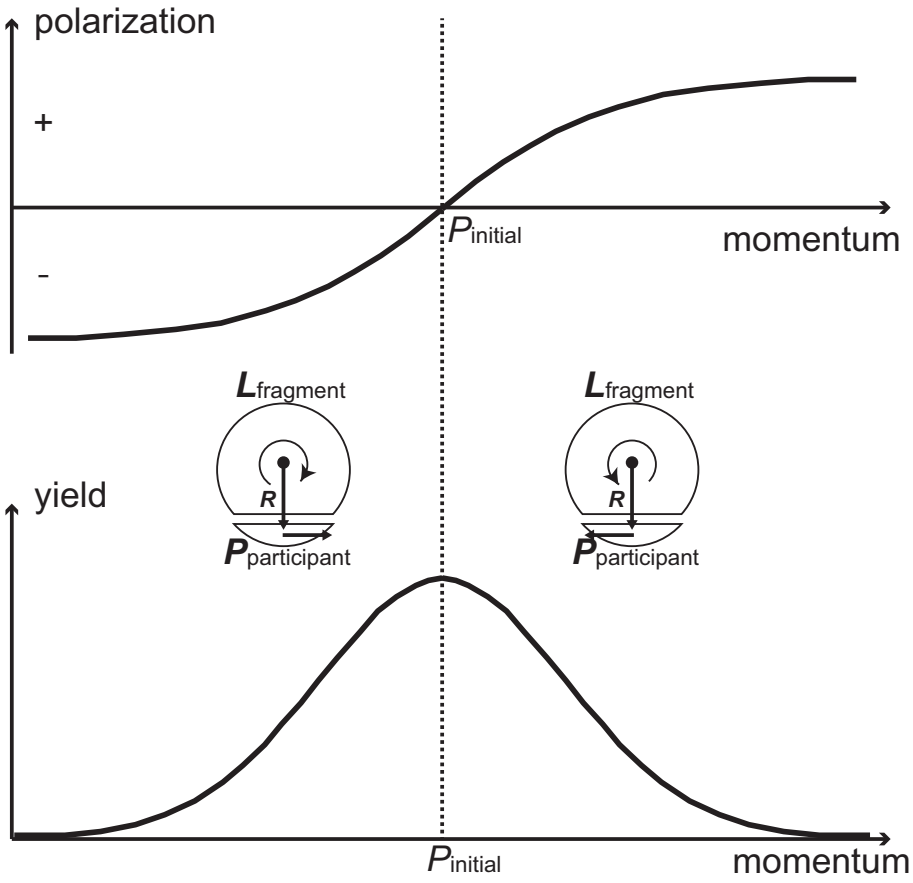

Figure 2.2: Momentum dependence of spin polarization degree of fragment

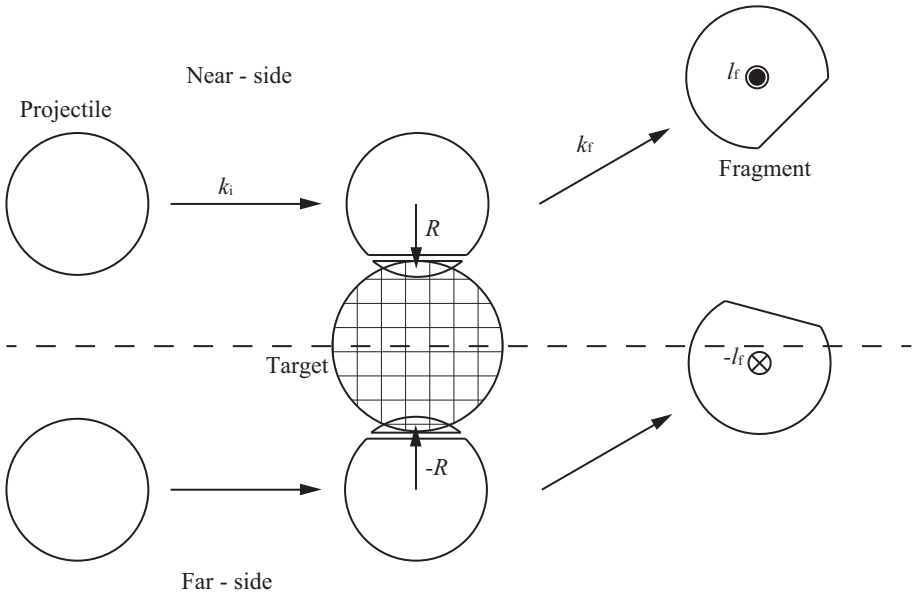

Figure 2.3: Near-and far-side orbitals

of the fragment can be decomposed into the contribution of each orbit. Emission angle distribution $W(\theta_{\rm L})$ is expressed as follows:

$$W(\theta_{\rm L}) \propto \exp\left(-\frac{\left(\theta_{\rm L}-\bar{\theta}_{\rm def}\right)^2}{2\Delta\theta_{\rm F}^2}\right)+\left(-\frac{\left(\theta_{\rm L}+\bar{\theta}_{\rm def}\right)^2}{2\Delta\theta_{\rm F}^2}\right). \tag{2.6}$$

Here, the first and second terms are the fragment distributions of the near- and far-side orbits, respectively, and $\bar{\theta}_{\rm def}$ is the average value of the orbital deflection of the fragments. Conventionally, this is calculated based on the nuclear forces acting between the projectile and the target nucleus and the Coulomb force. The sign of polarization is positive when the fragment is bent outward relative to the target nucleus and negative when it is bent inward. Generally, when the nuclear force is dominant, it becomes easy for the orbit to be bent inward, and, when the Coulomb force is dominant, it becomes easy for the orbit to be bent outward. The competitive relationship between near- and far-side orbits is determined by the magnitude of the proton number Z of the projectiles and the target nucleus. Here, $\Delta\theta_{\rm F}$ is the variance of the orbital deflection angle. From Eq. 2.6, the ratio of the number of fragments N that passed through the near-side orbit to the number of fragments F that passed through the far-side orbit is expressed as follows:

$$\frac{N}{F}=\exp\left(\frac{\theta_{\rm L}\bar{\theta}_{\rm def}}{\Delta\theta_{\rm F}^2}\right). \tag{2.7}$$

Here, R_{NF} is an index representing the competitive relationship between near- and far-side orbits:

$$R_{NF}\equiv\frac{\theta_{\rm L}\bar{\theta}_{\rm def}}{\Delta\theta_{\rm F}^2}. \tag{2.8}$$

When $R_{NF}\gg 1$, the near-side orbit dominates, and, when $R_{NF}\ll -1$, the far-side orbit dominates. In addition, when $R_{NF}\sim 0$, fragments passing through the near- and far-side orbits are equal. If the collision coefficient that contributes to the reaction also occurs due to stripping or merely by fluctuation in the internal motion of the nucleon, $\Delta\theta_{\rm F}$ can be expressed as follows using the fluctuation of the momentum in Eq. 2.3:

$$\Delta\theta_{\rm F}=\frac{\sigma_{\rm G}}{p_0}. \tag{2.9}$$

Furthermore, if $\bar{\theta}_{\rm def}$ is selected for $\theta_{\rm L}$, Eq. 2.8 is simply expressed as $(\bar{\theta}_{\rm def}/\Delta\theta_{\rm F})^2$, and $R_{\rm def}$ in Eq. 2.10 (an index representing the orbit's competitive relationship) is expressed as follows:

$$R_{\rm def}\equiv\frac{\bar{\theta}_{\rm def}}{\Delta\theta_{\rm F}}. \tag{2.10}$$

Therefore, a spin-polarized unstable nuclear beam can be obtained by selecting the momentum and its emission angle during the projectile fragmentation reaction.

2.1.4 Nucleon pick-up reaction

In a nucleon pick-up reaction, a projectile strips one or more nucleons from the target nucleus and moves to another nucleus. Similar to the projectile fragmentation reaction case, here, the nuclei produced by the pick-up reaction are emitted in the form of a beam; thus the target unstable nuclide can be taken out through a beam optical system. Changes in momentum in nucleon pick-up reactions have been measured by Souliotis *et* al. [15] and Turzo *et* al. [16]. Assuming that the nucleon that moves parallel to the projectile is stripped off during the reaction, written as follows:

$$\vec{p}_{\mathrm{f}*} = \frac{A_{\mathrm{f}*}}{A_{\mathrm{p}}}\vec{p}_{rmp} + \vec{k} \tag{2.11}$$

$$\vec{k} = \vec{K} - \frac{A_{\mathrm{f}*} - A_{\mathrm{p}}}{A_{\mathrm{p}}}\vec{p}_{\mathrm{p}} \tag{2.12}$$

$$\vec{p}_{\mathrm{f}} = \frac{A_{\mathrm{f}}}{A_{\mathrm{f}*}}\vec{p}_{\mathrm{f}*} \tag{2.13}$$

$\vec{p}_{\mathrm{f}*}$: the linear momenta of the pre-fragment

$A_{\mathrm{f}*}$: the number of nucleons of the pre-fragment

A_{p} : the number of nucleons of the projectile

$\vec{p}_{\mathrm{p}}$: the linear momenta of the projectile

$\vec{K}$: Fermi momentum of nucleon (~ 230 MeV/c)

A_{f} : the number of nucleons of the fragment

$\vec{p}_{\mathrm{f}}$: the linear momenta of the fragment

Moreover, expansion of the momentum distribution in pick-up reaction σ_{P} is expressed as follows:

$$\sigma_{\mathrm{P}} = \sigma_0\sqrt{\frac{A_{\mathrm{PF}}(A_{\mathrm{P}} - A_{\mathrm{PF}})}{A_{\mathrm{P}} - 1}}. \tag{2.14}$$

$A_{\mathrm{PF}} = A_{\mathrm{F}} - \Delta A_{\mathrm{t}}$: mass of the projectile part of the final product

ΔA_{t} : the number of nucleons picked up from the target

A_{P} : mass of projectile nuclei

σ_0 ~ 90 MeV/c

2.1.5 Production of spin polarization by nucleon pick-up reaction

Groh *et al.* reported that a large polarized RI could be produced by an intermediate energy pick-up reaction [18]. In their experiment, they successfully obtained polarization of $(8.5 \pm 0.6)\%$ by utilizing the reaction of ^{36}Ar (150 AMeV) + Be $\rightarrow$ ^{37}K.

It is also expected that spin polarization can be produced in a one-neutron pick-up reaction. From a projectile stationary system perspective, the target nucleus and pick-up nucleus come closer

to the projectile at a constant speed; thus nuclear accompanied by angular momentum is produced by nucleon trapping (Fig. 2.4). The magnitude of the expected angular momentum is given as follows.

$$\begin{aligned} l_z &\sim r_0 \cdot k_{\mathrm{Fermi}}. \\ r_0 &: \text{nuclear radius} \end{aligned} \tag{2.15}$$

Therefore, the sign of polarization is not dependent on the projectile momentum and the emission angular momentum. In this case, the spin polarization degree P is expected as follows:

$$P = \begin{cases} + & \text{(Far-side orbital)} \\ - & \text{(Near-side orbital).} \end{cases} \tag{2.16}$$

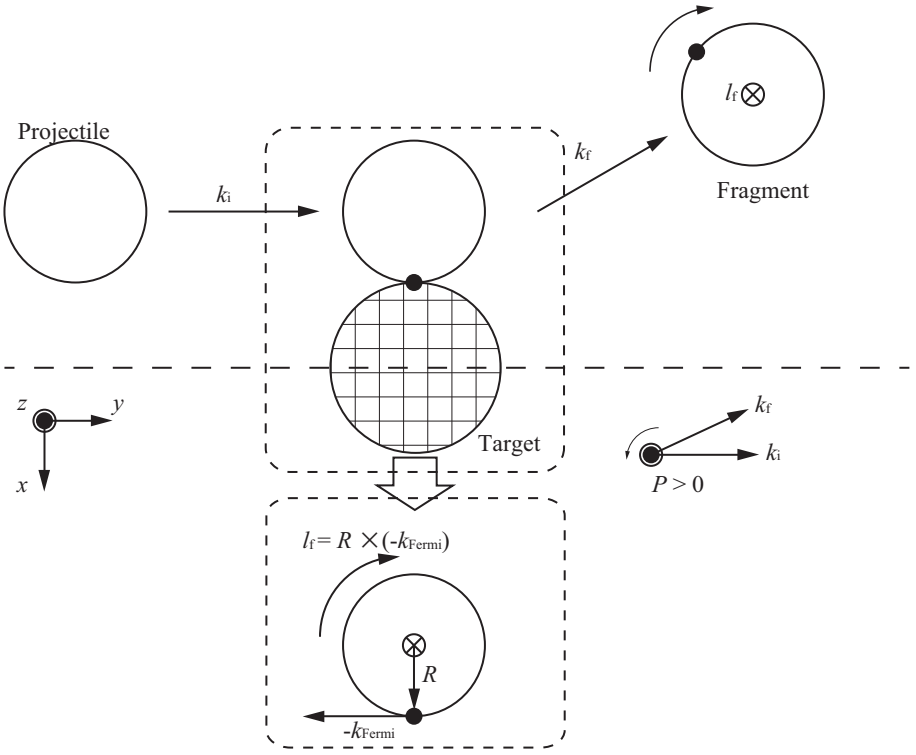

Figure 2.4: Production of spin polarization by nucleon pick-up reaction

2.2 Measurement of nuclear magnetic moment

2.2.1 Energy level and transition frequency

The nuclear Hamiltonian with magnetic moment μ, in static magnetic field B_0 is expressed as follows:

$$\mathcal{H} = -\boldsymbol{\mu} \cdot \boldsymbol{B}_0 = -g\mu_{\mathrm{N}} I_z B_0, \tag{2.17}$$

where g is the g-factor of the nucleus, μ_{N} is the nuclear magneton, and I_z is the z axis direction of nuclear spin. Here, energy levels $m = I, I-1, \ldots, -I+1, -I$ are expressed as follows:

$$E_m = -g\mu_{\mathrm{N}} B_0 m. \tag{2.18}$$

Thus, z direction components of spin I are separated at equal intervals to $2I+1$ according to the magnetic quantum number m. Then, energy levels are represented as follows:

$$E(m) = -g\mu_{\mathrm{N}} B_0 m \tag{2.19}$$

It is referred to as Zeeman splitting. The energy difference between adjacent levels is expressed as follows:

$$\begin{aligned} \Delta E &= -g\mu_{\mathrm{N}} B_0 (I-1) - (-g\mu_{\mathrm{N}} B_0 I) \\ &= g\mu_{\mathrm{N}} B_0 \\ &= h\nu_{\mathrm{L}}. \end{aligned} \tag{2.20}$$

Here, $\nu_{\mathrm{L}} = g\mu_{\mathrm{N}} B_0 / h$ is the Larmor frequency.

Nuclei with electric-quadrupole moment Q in electric field gradient eq are affected by electric quadrupole interaction in addition to magnetic dipole interaction. The Hamiltonian of this system is expressed as follows:

$$\mathcal{H} = -g\mu_{\mathrm{N}} I_{\mathrm{Z}} B_0 + \frac{eqQ\left(3\cos^2\theta_{c-\mathrm{axis}} - 1\right)}{8I(2I-1)}\left[3I_{\mathrm{Z}}^2 - I(I+1)\right], \tag{2.21}$$

where eq is the electric field gradient, Q is the quadrupole moment and $\theta_{c-\mathrm{axis}}$ is the angle between the B_0 axis and the crystalline c-axis. The transition frequency $\nu_{m,m+1}$ between the magnetic sublevels m and $m+1$ under a combined Zeeman and electric-quadrupole interaction is expressed as follows:

$$\begin{aligned} V_{m,m+1} &= (E_m - E_{m+1})/h \\ &= \frac{g\mu_{\mathrm{N}} B_0}{h} - \frac{3eqQ}{h}\frac{\left(3\cos^2\theta_{c-\mathrm{axis}} - 1\right)}{8I(2I-1)}(2m+1) \\ &= \nu_{\mathrm{L}} - \nu_Q \frac{3\left(3\cos^2\theta_{c-\mathrm{axis}} - 1\right)}{8I(2I-1)}(2m+1), \end{aligned} \tag{2.22}$$

where $\nu_Q = eqQ/h$ denotes the quadrupole coupling constant. In the case of ^{21}O, nuclear spin I is expected to be $5/2$. As a result, $\nu_{m,m+1}$ can be rewritten as follows:

$$\nu_{m,m+1} = \nu_{\mathrm{L}} - \nu_Q \frac{3\left(3\cos^2\theta_{c-\mathrm{axis}} - 1\right)}{80}(2m+1). \tag{2.23}$$

Figure 2.5 shows the changes in energy levels for ^{21}O. In this experiment, because we chose a CaO crystal that have no electrical field gradient eq, so the width of energy level is constant as center figure of Fig. 2.5 and

$$\nu_{m,m+1} = \nu_L. \tag{2.24}$$

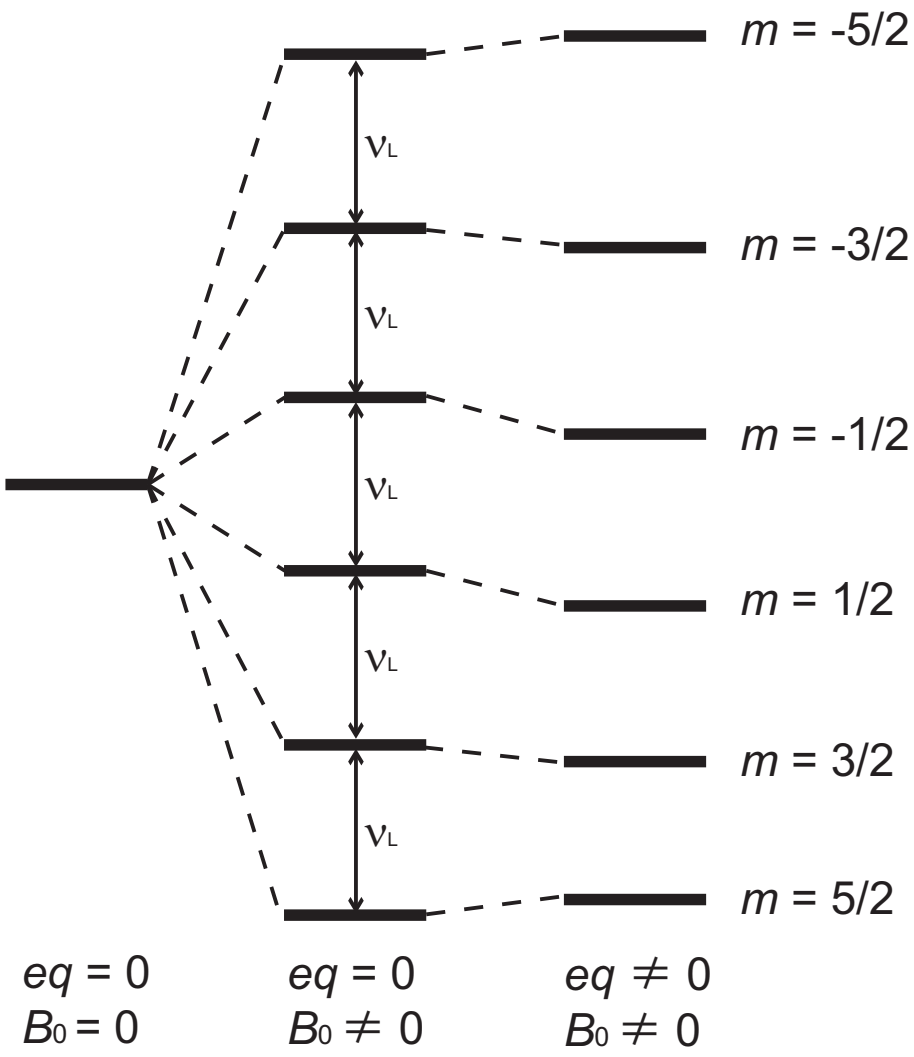

Figure 2.5: Energy level changes for ^{21}O

2.2.2 Hyperfine interaction of implanted nuclei

The selection of host materials is very important for β-NMR measurements because the preserved polarization, resonance frequency shift, and the broadening of the width of the NMR spectrum depend on the hyperfine interaction between the implanted nuclei and the stopper materials. In this section, the hyperfine interactions of impurities in stopper materials, such as spin-lattice relaxation, broadening resonance width, and resonance frequency shift, are discussed. Since these items differ for metallic and non-metallic stoppers, the differences are also described.

Spin-lattice relaxation

Interactions between implanted nuclei and electrons in a crystal can cause relaxation. Generally, the Hamiltonian for the electromagnetic interaction between nuclei and electrons is expressed as follows:

$$\mathcal{H} = 2\mu_{\mathrm{B}}\gamma\hbar\boldsymbol{I}\left[\frac{\mathrm{l}}{r^3} - \frac{\boldsymbol{s}}{r^3} + 3\frac{\boldsymbol{r}(\boldsymbol{s}r)}{r^5} + \frac{3}{8}\pi\boldsymbol{s}\delta(r)\right], \tag{2.25}$$

where μ_{B} is the Bohr magneton, $\boldsymbol{I}$ is the nuclear spin, and $\boldsymbol{l}$ and $\boldsymbol{s}$ are the orbital and intrinsic spins of electrons, respectively [19]. In free space, this interaction becomes very large; however, in a diamagnetic sample, it is reduced the orbital angular momentum disappears.

The spin-lattice relaxation and resonance frequency shift, i.e., the Knight shift, in metals are caused by the conduction S electrons. They are associated with the following well-known Korringa relation:

$$T_1\left(\frac{\Delta H}{H}\right)^2 = \frac{\hbar}{4\pi kT}\frac{\gamma_{\mathrm{e}}^2}{\gamma_{\mathrm{n}}^2}, \tag{2.26}$$

where γ_{e} and γ_{n} denote the spin g factors of the electrons and nuclei, respectively, $\Delta H/H$ is the Knight shift, and T_1 is spin-lattice relaxation time. From this relation, relaxation time T_1 is expected to be inversely proportional to temperature T. Note that the temperature must be decreased to increase the relaxation time.

In the case of insulators, spin-lattice relaxation time is not given by a simple relation, such as Eq. 2.26. Spin-lattice relaxation time in pure metal is greater than 10^2 s at room temperature [20]. The paramagnetic impurity in the crystal is the primary cause of relaxation. In this study, lattice defects produced in crystals during the implantation process may also have caused the relaxation because defects may cause fluctuation in local magnetic and/or electric fields, thereby destroying the nuclear polarization [21].

Line broadening

The implanted nucleus is surrounded by multiple host nuclei that cause a local magnetic field. Fluctuation in the local magnetic field causes the resonance width to increase.

As reported in the literature [19], the magnetic dipole interaction is expressed as follows:

$$\mathcal{H}_{12} = \frac{\gamma_1\gamma_2\hbar^2}{\boldsymbol{r}_{12}^3}\left[\boldsymbol{I}_1\boldsymbol{I}_2 - 3\frac{(\boldsymbol{I}_1\boldsymbol{r}_{12})(\boldsymbol{I}_2\boldsymbol{r}_{12})}{\boldsymbol{r}_{12}^2}\right], \tag{2.27}$$

where $\boldsymbol{r}_{12}$ is the vector connecting two spins. Thus dipolar broadening ($\bar{\Delta}\bar{\omega}$) is expressed as follows:

$$(\bar{\Delta}\bar{\omega})^2 = \frac{1}{3}\gamma_l^2\gamma_s^2\hbar^2 S(S+1)\sum_i \frac{\left(3\cos^2\theta_i - 1\right)^2}{\boldsymbol{r}_i^6}, \tag{2.28}$$

where γ_l and γ_s are the gyromagnetic ratios of the implanted and host nuclei, respectively, θ_i is the angle between their direction and the magnetic field B_0, and $\boldsymbol{r}_i$ is the distance between them. A sum should be taken over the surrounding nuclei [22]. Dipolar broadening is associated with spin-spin relaxation time T_2 as follows:

$$\frac{1}{\pi T_2} = \bar{\Delta}\bar{\omega}. \tag{2.29}$$

In addition to the magnetic interaction between the implanted nuclei and surrounding nuclei, eqQ causes line broadening if implanted nuclei have a quadrupole moment. There are some causes to generate a local electric field gradient, such as the creation of lattice defects during the implantation processes and a local lattice effect caused by impurities. However, estimating the broadening is difficult.

Chemical shift

An implanted nucleus is affected by many local magnetic and electric fields in addition to the experimental magnetic field for the β-NMR measurements. These fields can cause a shift in the resonance frequency.

In the case of a metallic sample, the primary cause of the shift is the magnetic field generated by conduction electrons, i.e., the Knight shift, which depends on the concentration of implanted nuclei. The measured Knight shift is in order of 0.01–1%

Even in the case of an insulator, we must still consider diamagnetic effects due to the rotation of electrons around the nuclei [23]. The contribution from polarization of the atomic spin induced by the external magnetic field, known as paramagnetic shielding, also causes a shift. Due to these magnetic fields, the total magnetic field is expressed as follows:

$$B = B_0(1-\sigma), \tag{2.30}$$

where B_0 is the external magnetic field and σ, which is equivalent to the shift of resonance frequency, σ, i.e., the chemical shift, is independent of the external magnetic field and is of the order of $10^{-4} \sim 10^{-2}$.

2.2.3 β-NMR method

The β-ray-detected nuclear magnetic resonance (β-NMR) method [24] is an experimental method to detect nuclear magnetic resonance by observing the change in the β-ray emission angle distribution from nuclear spin-polarized unstable nucleus. Among them, the β-ray-detected nuclear quadrupole resonance method (β-NQR method) [25] refers to the observation of nuclear magnetic resonance frequency separation by electric quadrupole interaction. The β-NMR method and the β-NQR method are characterized by having sensitivity $\sim 10^{10}$ times or more compared to ordinary NMR methods since one unstable nucleus (RI) emits one signal called β-ray, and the yield is an excellent method capable of measuring at least nuclear moment. The β-NMR method is very effective for investigating the structure of unstable nuclei.

Observation of spin polarization

A method to obtain the spin-polarized radioactive nucleus is discussed in section 2.1. The β-ray angular distribution $W(\theta)$ for the β ray emitted from nuclei with spin polarization P [26] is expressed as follows:

$$W(\theta) = 1 + \frac{v}{c} A_\beta P \cos\theta, \tag{2.31}$$

where θ is the angle between the direction of the β-ray emission and the axis of the nuclear polarization, $\frac{v}{c}$ is the velocity of the β particle. A_β denotes the β-ray asymmetry parameter. The sign of P is positive when the spins are preferentially directed in the z axis. In the case of ^{21}O, a decay Q value $Q_{\beta^-} = 8110$ keV [27]. A β particle loses energy when penetrating materials around the stopper prior to entering the β-ray detectors; thus only β particles with $E_\beta \geq 1600$ keV [28] (or $\frac{v}{c} \geq 0.97$) were counted. As a result, $W(\theta)$ in Eq. 2.31 is well approximated by the second expression $\frac{v}{c} \approx 1$. Note that the asymmetry parameter is described in Section 8.2.

The spin-polarized fragments are implanted in a stopper crystal, to which a static magnetic field is applied in order to preserve the spin polarization. Because the energy of β-rays emitted is sufficiently large, it can be considered as $v/c = 1$. When the difference in the number of β rays is maximized in the 0° and 180° directions relative to the direction of polarization of nuclear spin. Thus, the detector is set in the $\theta = 0°$ and $\theta = 180°$ directions, and, by comparing the counts of these β-rays it is possible to detect the amount of nuclear polarization. Here, the β-ray counts in the up and down detectors are denoted N_u and N_d, respectively. The up/down ratio R of the β-ray counts is expressed as follows:

$$R = \frac{N_\mathrm{u}}{N_\mathrm{d}} = a\frac{1 + A_\beta P}{1 - A_\beta P}, \tag{2.32}$$

where a is the ratio of β-ray detection efficiency between the up and down detectors.

Observation of resonance by nuclear spin operation

An RF coil is placed on both sides of the stopper, and the nuclear spin of the unstable nucleus can be manipulated by applying a high frequency magnetic field B_1 in a direction perpendicular to

the external static magnetic field B_0. When an external magnetic field exists, the nuclear spin wraps around an external magnetic field and precesses at the Larmor frequency (ν_{L}) around the external static magnetic field B_0. The movement of free spins with magnetic moments in the electrostatic field is expressed as follows:

$$\frac{d\vec{\mu}}{dt} = \gamma\vec{\mu} \times \vec{B}_0 \quad \left(\gamma = \frac{g\mu_{\mathrm{N}}}{\hbar}\right). \tag{2.33}$$

Then, by applying a high frequency magnetic field B_1 (angular frequency ω) in the direction perpendicular to the external static magnetic field B_0, the effective magnetic field changes and the nuclear spin precesses around the vector sum of B_0 and B_1. Assuming that the B_0 direction is the z axis and the B_1 direction is the x axis, Eq. 2.33 can be written as follows:

$$\frac{d\vec{\mu}}{dt} = \gamma\vec{\mu} \times \left\{\left(B_0 - \frac{\omega}{\gamma}\right)\vec{e}_Z + B_1\vec{e}_X\right\}. \tag{2.34}$$

Thus, the effective magnetic field changes as follows:

$$\vec{B}_{\mathrm{eff}} = \left(B_0 - \frac{\omega}{\gamma}\right)\vec{e}_Z + B_1\vec{e}_X, \tag{2.35}$$

and, as shown in Fig. 2.6, nuclear spins precess around this magnetic field.

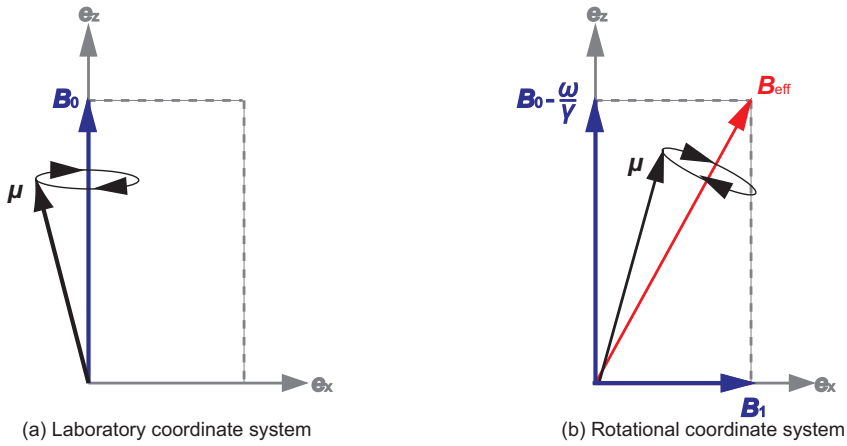

Figure 2.6: Precession of nuclear spin

Nuclear spin is associated with magnetic moment with the relation $\mu = g\mu_{\mathrm{N}}I$. Thus, spin polarization can be manipulated via a magnetic field. The depolarization and adiabatic fast passage (AFP) [19] spin operation methods are described in the following.

1. Depolarization method

A radio frequency magnetic field with frequency that is equal to the resonance frequency (Larmor frequency) ν_{L} is applied to destroy nuclear spin polarization. When the angular frequency ω of the radio frequency magnetic field B_1 is equal to $\omega_{\mathrm{L}} = \gamma B_0$ $(= 2\pi\nu_{\mathrm{L}})$, the B_0 component in the rotating coordinate system is canceled and the effective magnetic field B_{eff} is equal to B_1. Here, the

magnetic moment precesses around the x' axis; thus, the component in the quantizing axis direction of the nuclear spin, i.e., the static magnetic field direction, becomes zero on time average and the polarization disappears (Fig. 2.7). Therefore, the degree of asymmetry of the detector at $\theta = 0°$ and $\theta = 180°$ changes, and the spin polarization can be obtained from the amount of this change.

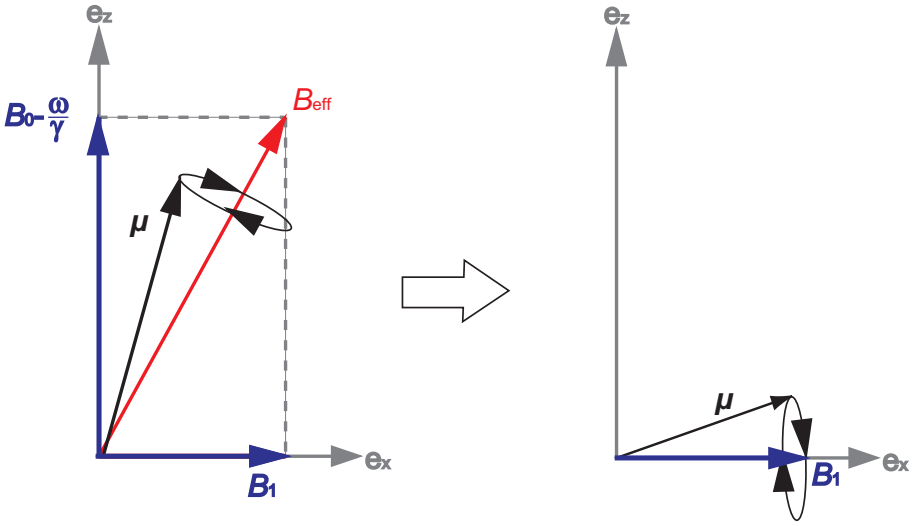

Figure 2.7: Nuclear spin motion in depolarization method

2. AFP method

The AFP method reverses the spin by adiabatically (slowly) changing the frequency ω of the radio-frequency magnetic field before and after ω_{L}. In the case of applying the radio frequency magnetic field B_1 as shown in Fig. 2.6, nuclear spin precesses around the effective magnetic field B_{eff} in the rotating coordinate system of frequency ω. Here, when B_{eff} is changed at a sufficiently slow rate compared to the angular frequency of nuclear spin precession, the nuclear spin follows precession movement with B_{eff}. If ω is changed slowly before and after the angular frequency at which resonance occurs, the nuclear spin can be inverted completely (Fig. 2.8). Therefore, the degree of asymmetry of the detector at $\theta = 0°$ and $\theta = 180°$ changes and nuclear polarization can be observed from the change amount.

The adiabatic condition is expressed as follows:

$$\frac{d\omega}{dt} \ll (\gamma B_1)^2. \tag{2.36}$$

Here, $d\omega$ is the full width of frequency modulation (FM) and dt is RF time. Using only this conditional expression, it is said that it is better if it compares both, and it is better that it is not clear how much it should be increased quantitatively. Therefore, factor K is introduced as an index to compare $d\omega$ and dt.

$$B_1 = \frac{K\sqrt{\frac{d\omega}{dt}}}{\gamma} \tag{2.37}$$

Spin reversal using this K value as an indicator has been studied experimentally and via simulations. The reversal rate is approximately 99% if the K value is 2.7 or greater, and the change in the reversal rate is small if K is 2.0 or greater. However, spin relaxation will occur if the frequency sweep rate is too slow to satisfy the adiabatic condition. Therefore, the sweep rate must be faster than the spin relaxation time in the stopper sample.

Moreover, when the radio frequency magnetic field B_1 is not sufficiently large compared with the oscillating magnetic field at the embedded position of polarized nuclei in the crystal, the nucleus polarization collapses when the direction of nuclear polarization is parallel to B_1. In order to prevent this, the following conditions are required.

$$\frac{2\pi}{D} < \gamma B_1 \tag{2.38}$$

where D is dipolar broadening, which represents expansion of the resonance line by the oscillating magnetic field. The spin-spin relaxation (longitudinal relaxation) time T_2 becomes:

$$D \propto 1/T_2$$

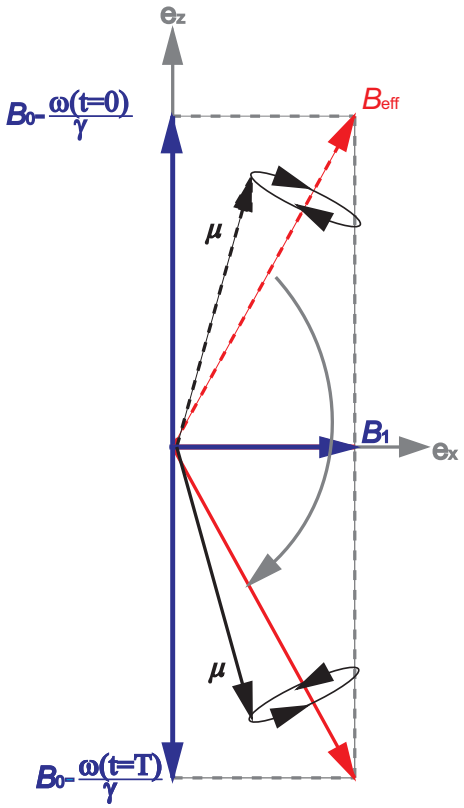

Figure 2.8: Nuclear spin motion in AFP method

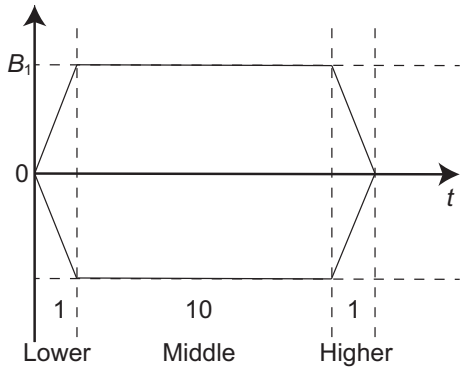

Figure 2.9: Example of amplitude control of oscillating magnetic field. The horizontal axis represents time and the vertical axis represents the oscillating magnetic field strength.

In frequency sweeping, there is another problem to consider. Frequency sweeping searches the resonance with a certain width, but when the resonance frequency exists at the end of the sweep width, the angle θ of the effective magnetic field suddenly changes. As a result, the spin can not keep up with the rapid change of the effective magnetic field, and the spin polarization destroy. To solve this problem, there is a method of making the amplitude of the oscillating magnetic field trapezoidal as shown in Fig. 2.9. Here, the frequency of the oscillating magnetic field to be applied over time also changes so as to be proportional to time. The region that realizes a spin reversal rate of 100% is a flat part in the center, and 100% spin reversal is not realized at both ends of the trapezoid. In this study, the ratio of the edge part to the flat part of the trapezoid was set to be 1 : 10 : 1. By suppressing the sudden change of the oscillating magnetic field by this method, the spin polarization is prevented from collapsing.

The NMR method using an AFP technique is referred to as the 4AP method. In this method, the up/down ratio $R_{\rm off}$ of the detector at $\theta = 0^\circ$ and $\theta = 180^\circ$ when no radio frequency magnetic field is applied is expressed as same as Eq. 2.32,

$$R_{\rm off} = \frac{N_{\rm u}}{N_{\rm d\,off}} = a\frac{1 + A_\beta P}{1 - A_\beta P}. \tag{2.39}$$

Then, the spin is inverted using the AFP method, polarization P becomes $-P$, and Eq. 2.39 can be written as follows:

$$R_{\rm on} = \frac{N_{\rm u}}{N_{\rm d\,on}} = a\frac{1 + A_\beta(-P)}{1 - A_\beta(-P)} = a\frac{1 - A_\beta P}{1 + A_\beta P}. \tag{2.40}$$

Here, we define r as follows:

$$r = \frac{R_{\rm on}}{R_{\rm off}}. \tag{2.41}$$

When the radio frequency magnetic field is applied when $R_{\rm on}$ satisfies the resonance condition, the

nuclear polarization is inverted and r is written by

$$\begin{aligned} r &= \frac{a\frac{1-A_\beta P}{1+A_\beta P}}{a\frac{1+A_\beta P}{1-A_\beta P}} \\ &= \frac{(1-A_\beta P)^2}{(1+A_\beta P)^2} \\ &\approx 1-4A_\beta P. \end{aligned} \tag{2.42}$$

Then, $A_\beta P$ is expressed as follows:

$$A_\beta P = \frac{1-\sqrt{r}}{1+\sqrt{r}} \approx \frac{1}{4}(1-r). \tag{2.43}$$

The case where the applied oscillating magnetic field includes the resonance frequency has been considered. When an oscillating magnetic field that does not include the resonance frequency is applied, spin reversal does not occur and there is no change in the up/down counting ratio. Therefore, r becomes 1.

$$r = \frac{a\frac{1+A_\beta P}{1-A_\beta P}}{a\frac{1+A_\beta P}{1-A_\beta P}} = 1. \tag{2.44}$$

In other words, by determining if r has shifted from 1, we can identify whether resonance has occurred and the resonance frequency can be determined. In order to evaluate the figure of merit (FOM) for the detection β-ray asymmetry change, we define a quantity D_σ which means the deviation of the ration r from unity as

$$D_\sigma = \frac{1-r}{\Delta r} \tag{2.45}$$

Here, Δr is the statistical error stemming from the β-ray counting statistics. As β decay occurs randomly, β-ray counts follow a Poisson distribution. Note that errors in up/down counting are denoted $\sqrt{N_\mathrm{u}}$ and $\sqrt{N_\mathrm{d}}$, respectively. From the error propagation rule, the error of R can be expressed as follows:

$$\frac{\Delta R}{R} = \sqrt{\left(\frac{\sqrt{N_\mathrm{u}}}{N_\mathrm{u}}\right)^2 + \left(\frac{\sqrt{N_\mathrm{d}}}{N_\mathrm{d}}\right)^2} = \sqrt{\frac{1}{N_\mathrm{u}} + \frac{1}{N_\mathrm{d}}}. \tag{2.46}$$

From this equation, the r error is as follows:

$$\frac{\Delta r}{r} = \sqrt{\left(\frac{\Delta R_\mathrm{off}}{R_\mathrm{off}}\right)^2 + \left(\frac{\Delta R_\mathrm{on}}{R_\mathrm{on}}\right)^2}. \tag{2.47}$$

From Eqs. 2.46 and 2.47, we can see that Δr is computed as follows:

$$\Delta r = r\sqrt{\frac{1}{N_\mathrm{u-off}} + \frac{1}{N_\mathrm{u-on}} + \frac{1}{N_\mathrm{d-off}} + \frac{1}{N_\mathrm{d-on}}} = r\sqrt{\frac{4}{N}}. \tag{2.48}$$

Assuming that the value of $A_\beta P$ is much smaller than 1 and the solid angle of the upper and lower counters does not change significantly, and the $N_\mathrm{u-off}$, $N_\mathrm{u-on}$, $N_\mathrm{d-off}$, and $N_\mathrm{d-on}$ value remain

almost unchanged. By substituting Eqs. 2.42 and 2.48 into Eq. 2.45 and rearranging it, D_σ can be expressed as follows.

$$D_\sigma \approx 2A_\beta P\sqrt{N} \tag{2.49}$$

Solving for N, Eq. 3.8 can be rewritten as follows:

$$N = \frac{D_\sigma^2}{4\left(A_\beta P\right)^2} \tag{2.50}$$

Therefore, it is possible to know the count necessary to obtain the statistical error D_σ when the spin polarization degree is $A_\beta P$. If Y_β is the yield per unit time of β rays and $T_{\rm exp}$ is measurement time, we can obtain $4N = Y_\beta T_{\rm exp}$. Therefore, measurement time $T_{\rm exp}$ can be expressed as follows:

$$T_{\rm exp} = \frac{D_\sigma^2}{\left(A_\beta P\right)^2 Y_\beta} \tag{2.51}$$

The figure of merit is given by the denominator on the right side of Eq. 2.51 as

$$\mathrm{FOM} = (A_\beta P)^2 Y_\beta. \tag{2.52}$$

The time sequence of the AFP method is shown in Fig. 2.10. After irradiating the beam to the stopper, the up/down ratio is measured in the initial polarized state without applying the radio frequency magnetic field. Then, beam irradiation is performed again, and the measurement is performed with a radio frequency magnetic field of the frequency to be investigated. Here, to prevent the spin operation in this loop from influencing measurement of the next loop, a radio frequency magnetic field of the same frequency is applied after the count time. This is considered a single loop that repeats until sufficient statistics are obtained.

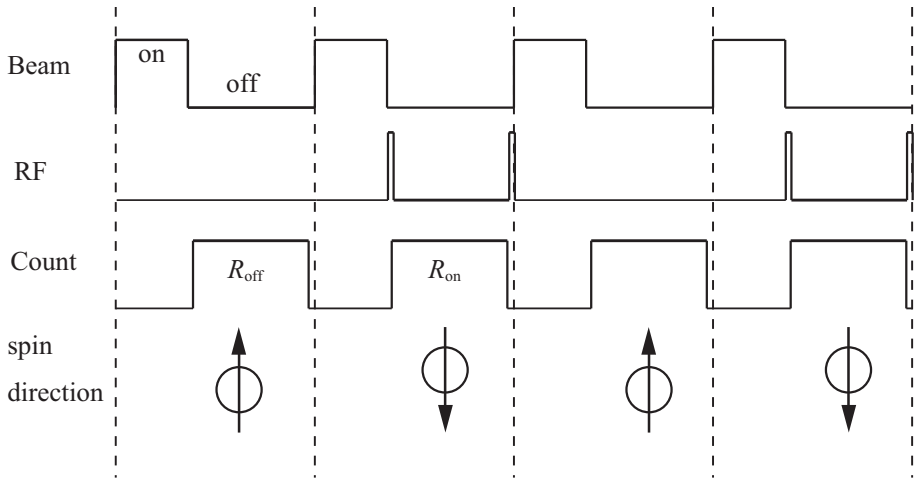

Figure 2.10: Time sequence of AFP method

Chapter 3

Development of β-NMR system

3.1 AFR method

The efficiency of the measurement using the β-NMR method primarily depends on the polarization degree P. In order to achieve resonance, it is necessary that a degree of polarization of sufficient magnitude is achieved. However, generally, predicting the polarization degree P of the nuclide obtained by the projectile fragmentation reaction and nucleon pickup reaction quantitatively is difficult. In the polarization degree measurement by the β-NMR method, however, a resonance can be observed only if all three conditions are satisfied simultaneously, i.e., production of spin-polarized RI beam, preservation of spin polarization in the stopper crystal, and a search for the resonance frequency, which makes the measurement difficult. To conduct this measurement in separate step-by-step procedures, we have developed a system in which spin polarization RI beams implanted in a crystal can be measured prior to NMR measurement. Therefore, the AFR method was developed to measure polarization. Note that the AFR method can handle a nuclide with unknown magnetic moment [29]. With the AFR method, it is possible to determine the polarization degree prior to carrying out the measurement by the β-NMR method. Figure 3.1 shows the initial experimental setup. In general, to preserve the spin polarization of nuclei with larger atomic numbers, a stronger B_0 field is required. To extend our study to neutron-rich *sd*-shell nuclei, $B_0 \geq 300$ mT is desirable; however this value is more than ten-times greater than the air-coil AFR system ($B_0 \sim 30$ mT). In the present study, an AFR system that can apply and rotate a field of $B_0 \sim 300$ mT has been developed. Details regarding the developed system will be provided in Chapter 4.

To measure the degree of polarization using the AFR method, the unstable nuclear beam is driven into the stopper crystal in the same way that the β-NMR method is carried out. The stopper is installed at the center of the static magnetic field B_0 to maintain the polarization, and the direction of the static magnetic field is applied in the z axis direction. Now, as the coordinate system, the incident direction of the beam is defined as the x axis. The adiabatic magnetic field rotating device creates a static magnetic field B_0 using permanent magnets above and below the stopper, and a detector for measuring β rays is installed inside each magnet. The setup is detailed in Fig. 4.1 in Section 4.1. By this static magnetic field nuclear spin precesses around B_0 in the stopper. Here,

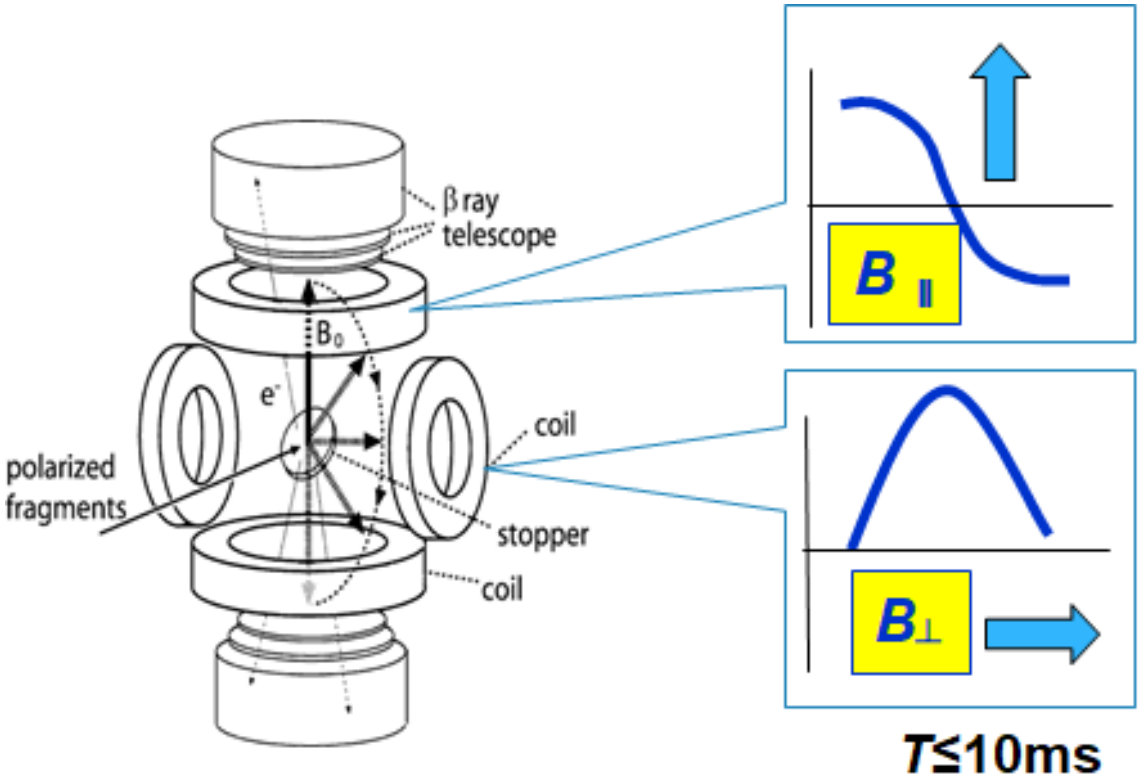

Figure 3.1: To study neutron-rich p-shell nuclei, two air coils were placed perpendicular to each other. The system can generate a rotating field as high as $B_0 \sim 30$ mT in a duration much shorter than β-decay lifetime.

when the holding magnetic field B_0 is rotated adiabatically, the nuclear spin I rotates with precession around B_0, and the nuclear spin I and B_0 are inverted 180°. Let T be the time required for a half turn of the magnetic field and t be the elapsed rotation time, the magnetic field B_0 can be expressed by the following equation.

$$\vec{B}_0(t) = \begin{pmatrix} 0 \\ B_{0y} \sin\left(\frac{\pi t}{T}\right) \\ B_{0z} \cos\left(\frac{\pi t}{T}\right) \end{pmatrix} \tag{3.1}$$

Here, in order to rotate the nuclear spin I adiabatically, nuclear spin must precess around the magnetic field faster than the rotational speed of the magnetic field. This condition is referred to as the adiabatic condition in the AFR method, and, for $B_{0z} \geq B_{0y}$, it can be expressed as follows [29].

$$\begin{aligned} (\gamma B_{0y}) B_{0y} &\gg \frac{\pi}{T} B_{0z} \\ \frac{B_{y0}^2}{B_{0z}} &\gg \frac{\pi}{T\gamma} \end{aligned} \tag{3.2}$$

In our AFR apparatus $B_{0y} = B_{0z}$ because the static magnetic field is reversed; thus Eq. 3.2 can be rewritten as follows.

$$T \gg \frac{\pi}{B_0 \gamma} \tag{3.3}$$

After performing adiabatic rotation of the magnetic field, we measure the up/down counting ratio of β rays with β ray detectors installed above and below the stopper. At this time, the up/down counting ratio when the static magnetic field B_0 is directed to a ($a =\uparrow$ or $\downarrow$) direction, and the spin is directed to b ($b =\uparrow$ or $\downarrow$) expressed as R_{ab}. In addition, the β ray counts of the upper and lower β ray detectors are denoted by N_{u} and N_{d}, respectively. Depending on the direction of the magnetic field, R_{ab} can be expressed as follow using the ratio ϵ_{det} of the detection efficiency of the upper and lower detectors and detection efficiency ϵ_{a}.

$$R_{ab} = \frac{N_{\mathrm{u}}}{N_{\mathrm{d}}}\epsilon_{\mathrm{det}}\epsilon_{\mathrm{a}} \tag{3.4}$$

A β-ray detector uses a photomultiplier tube, which is susceptible to the influence of a magnetic field. Since the AFR apparatus rotates and changes the static magnetic field that affects the photomultiplier, a difference in detection efficiency is concerned with the β ray detector depending on the direction of the magnetic field; thus ϵ_{a} is introduced. The vertical count ratio $R_{\uparrow\uparrow}$, $R_{\downarrow\downarrow}$, $R_{\uparrow\downarrow}$, $R_{\downarrow\uparrow}$ is measured by mechanically changing the up/down direction of the magnetic field and spin to determine these ratios r.

$$\begin{aligned} r &= \frac{R_{\downarrow\downarrow}}{R_{\uparrow\uparrow}}\frac{R_{\uparrow\downarrow}}{R_{\downarrow\uparrow}} = \left(\frac{1-A_\beta P}{1+A_\beta P}\right)^4 \\ &\approx 1 - 8A_\beta P \end{aligned} \tag{3.5}$$

Then, $A_\beta P$ is expressed as follows:

$$A_\beta P = \frac{1-\sqrt[4]{r}}{1+\sqrt[4]{r}} \approx \frac{1}{8}(1-r) \tag{3.6}$$

Next, we consider the time required for polarization degree measurement in the AFR method. As discussed in the Section 2.2.3, Δr can be expressed by the law of error propagation as follows.

$$\Delta r = r\sqrt{\frac{1}{N_{\mathrm{u}\uparrow\uparrow}} + \frac{1}{N_{\mathrm{d}\uparrow\uparrow}} + \frac{1}{N_{\mathrm{u}\downarrow\downarrow}} + \frac{1}{N_{\mathrm{d}\downarrow\downarrow}} + \frac{1}{N_{\mathrm{u}\uparrow\downarrow}} + \frac{1}{N_{\mathrm{d}\uparrow\downarrow}} + \frac{1}{N_{\mathrm{u}\downarrow\uparrow}} + \frac{1}{N_{\mathrm{d}\downarrow\uparrow}}} \tag{3.7}$$

Assuming now that the value of $A_\beta P$ is much smaller than 1 and the solid angles of upper and lower counters also do not change significantly, the $N_{\mathrm{u}\uparrow\uparrow}$, $N_{\mathrm{d}\uparrow\uparrow}$, $N_{\mathrm{u}\downarrow\downarrow}$, $N_{\mathrm{d}\downarrow\downarrow}$, $N_{\mathrm{u}\uparrow\downarrow}$, $N_{\mathrm{d}\uparrow\downarrow}$, $N_{\mathrm{u}\downarrow\uparrow}$, and $N_{\mathrm{d}\downarrow\uparrow}$ values almost unchanged. Then D_σ becomes as follows.

$$D_\sigma \approx 2A_\beta P\sqrt{2N} \tag{3.8}$$

Solving for N, Eq. 3.8 can be rewritten as follows.

$$N = \frac{D_\sigma^2}{8\left(A_\beta P\right)^2} \tag{3.9}$$

Then, $8N = Y_\beta T_{\mathrm{exp}}$; thus, the measurement time T_{exp} can be expressed as follows.

$$T_{\mathrm{exp}} = \frac{D_\sigma^2}{\left(A_\beta P\right)^2 Y_\beta}. \tag{3.10}$$

The time sequence of AFR method is shown in Fig. 3.2. After irradiating the beam to the stopper, measure the initial polarization state R without rotating the magnetic field. After the next beam irradiation, measurement is performed after rotating the magnetic field. To cancel the detection efficiency due to the direction of the magnetic field, measurement is performed in a state in which the magnetic field direction is reversed after the next beam irradiation. Finally, after beam irradiation, the magnetic field is rotated and measurement is performed in a state where the spin is reversed. This comprises a single loop that is repeated until sufficient statistics are obtained.

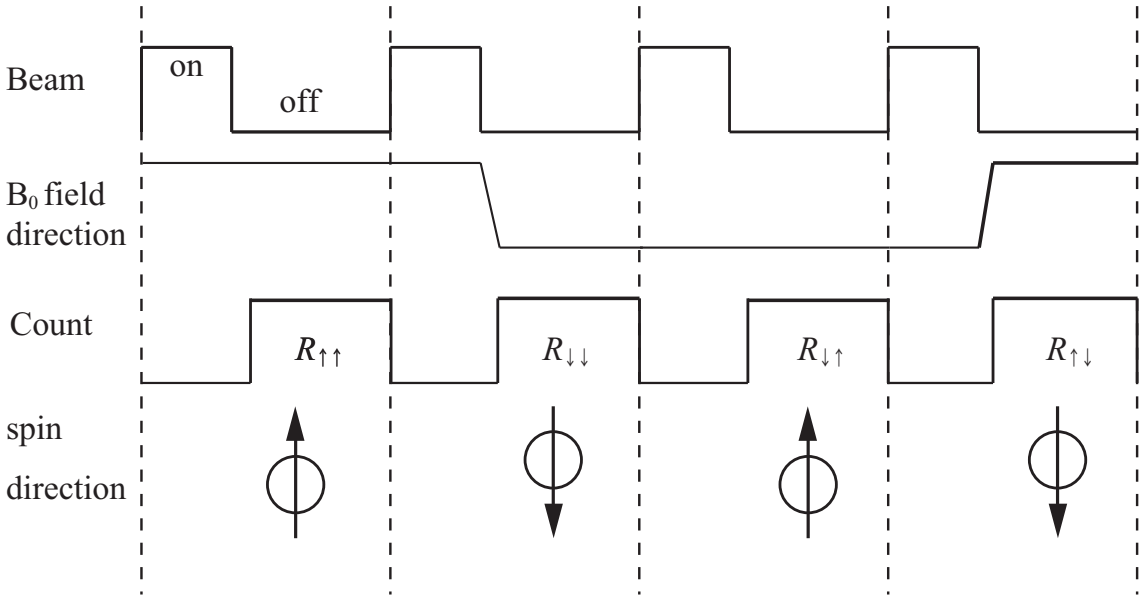

Figure 3.2: Time sequence of AFR method

3.2 RF oscillating magnetic field for β-NMR

The RF magnetic field is applied to the entire stopper by the coil in the LCR resonance circuit. Figure 3.3 shows the RF magnetic field generation circuit system. The RF magnetic field is output from function generator with control signal from programmable sequence generator (PSG) [31] as a trigger. The output RF is amplified using an RF preamplifier and a main amplifier. It is then transmitted to the LCR resonance circuit. Internal oscillation is less likely to occur due to the insertion of attenuators between the function generator and the RF preamplifier, and the RF preamplifier and the main amplifier.

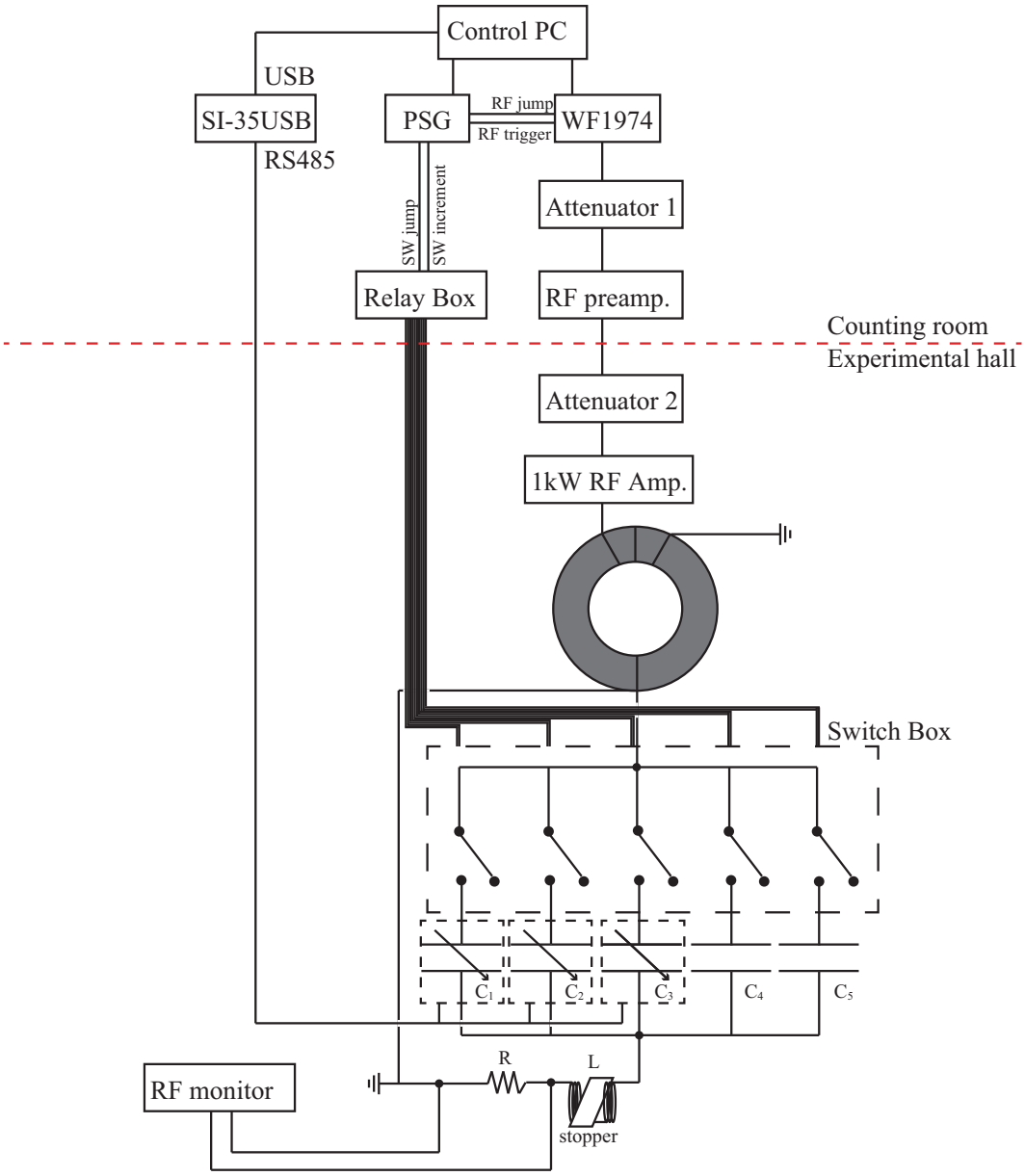

Figure 3.3: Circuit of RF magnetic field generation system

3.2.1 RF magnetic field system

Function generator

The function generator generates the RF magnetic field used in the NMR experiment. In this experiment, a WF1974 multi function generator (NF Co., Ltd.) was used. The RF was controlled using PSG control PC such that the voltage was output in synchronization with PSG. In addition, to output the necessary voltage, it is possible to calculate the frequency of the voltage according to the mode of the PSG, by the control PC, and by sending an instruction from the PC to the function generator. Note that the frequency that can be output is less than 10 MHz.

Attenuator

The attenuator was used to adjust the magnitude of the signal and prevent the function generator from being damaged due to reflection by the RF amplifier. Here, we used two TRA601D rotary attenuators (Tamagawa Electronics Co., Ltd.). By placing the first attenuator in the counting room, it is possible to adjust the RF magnitude without entering the experimental hall.

RF Amplifier

The RF amplifier was installed immediately before the coil to amplify the RF output. Here, the T145-6036A high-frequency amplifier (Thamway Co., Ltd.) was used as the main amplifier (maximum output : 1 kW; frequency band : 500 kHz to 15 MHz; power gain : 55 dB; input level : 0 dBm). When the reflection protection circuit was enable, if reflection occurred, an LED blinked to indicate that the input signal must be adjusted to avoid reflection.

Relay Box

The relay control box output the 24-V pulse required to operate the switch. In this experiment, a TCS-2110-0AU (Araki-eletec corp.) was used. This relay control switch has 10 output ports that output 24-V pulses and input port that receives SW increments and SW jumps via PSG control signals. Each time a signal enters SW increment, the switch connects nad then disconnects sequentially, i.e., "No 1 open" $\rightarrow$ "No 1 close" $\rightarrow$ "No 2 open". In addition, when a signal is input to SW jump, the switch number is reset to start from "No 1 open" even if it ends in the middle of the sequence.

Switch Box

A Kilovac K40P switch (TE Connectivity) was used in the fast switching system (Fig. 3.4). Fast switching systems must demonstrate satisfactory switching time and resistance to RF. Since the measurement target is an unstable nucleus with a lifetime of only several hundred milliseconds, it is impossible to obtain sufficient β-ray yield by collapsing if the switch time is long. In addition, since a frequency of several kW is added to the RF circuit, the switch must be robust against high

frequencies. The operation time of the Kilovac K40P switch is 1 ms, which is sufficiently short for our purpose. Figure 3.5 shows the schematic layout of a fast switching system [32]. As can be seen, five switches are arranged in parallel in the switch box. RF is input to the red terminal and output from one of the five black terminals. The BNC terminal is connected to the switch's open and close terminals, and a 24-V pulse is input to control the connection and disconnection of the switch output from the relay control box.

Variable capacitor

RF from the main amplifier is impedance matched by a toroidal core and transmitted to the LCR series resonance circuit. A variable capacitor that can adjust the capacitance whithin a certain range was used to adjust the resonance frequency of the LCR series resonance circuit. Here, three parallel capacitors were used such that the capacitors to be used could be selected by the PSG signal. The variable capacitor can be adjusted from 200–2000 pF remotely without entering the experimental room during beam irradiation.

RF Coil

The RF coil comprise two circular coils (coil diameter and distance between coils: 30 mm) arranged in a Helmholtz coil shape. A coil with six windings on one side was fabricated using a copper wire. Direct current was supplied to this coil, and the magnetic field in the stopper plane was measured using a Gauss meter. Here, the RF magnetic field strength (coil DC characteristic) per unit current of the coil was 2.2 Gauss/A. During the experiment, to monitor the current flowing through the coil, the voltage across the 0.5 Ω resistor was monitored using an oscilloscope. in addition, the RF magnetic field strength B_1 was obtained by converting the voltage into current to obtain the RF magnetic field intensity B_1 for AFP-NMR. Note that compliance with the adiabatic condition was evaluated.

Impedance matching

The RF magnetic field system was separated into high-frequency supply and resonance circuit sides. However, the RF pulse output from the main amplifier, i.e., the terminal on the high-frequency supply side, was 50 Ω for impedance Z_{in}, and the impedance Z_{out} at the resonance point on the resonance circuit side had resistance of 0.5 Ω, i.e., the impedance differed between the supply and resonance circuit sides. In addition, power loss due to reflection occurred at the connection point. To match impedances on both sides, both sides were connected by a toroidal core, and the number of turns to the core was adjusted to prevent power loss due to reflection at the connection point. The following relational expression represents winding ratio, where the number of turns on the high-frequency side and that on the resonance circuit side are denoted n_{in} and n_{out}, respectively.

$$\frac{Z_{\mathrm{in}}}{Z_{\mathrm{out}}} = \frac{n_{\mathrm{in}}^2}{n_{\mathrm{out}}^2} \tag{3.11}$$

Here, $Z_{\text{in}}/Z_{\text{out}} = 100$; thus $n_{\text{in}} : n_{\text{out}} = 10 : 1$. However, when the RF magnetic field strength applied to the coil was measured by adjusting the winding ratio of the RF voltage to approximately 2000 kHz to the toroidal core, the transmission rate was the best at $n_{\text{in}} : n_{\text{out}} = 3 : 1$. Therefore this ratio was set to 3 : 1. The waveform observed by the RF monitor is as shown in Fig. 3.6. Voltage was measured for each frequency range. Here, the winding ratio with the highest voltage was adopted, and V_i, V_m, and V_f represent the initial, middle, and end time voltages, respectively.

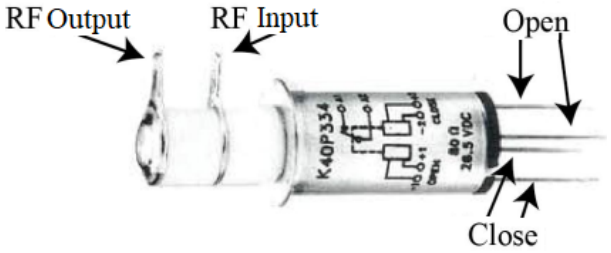

Figure 3.4: Fast switch

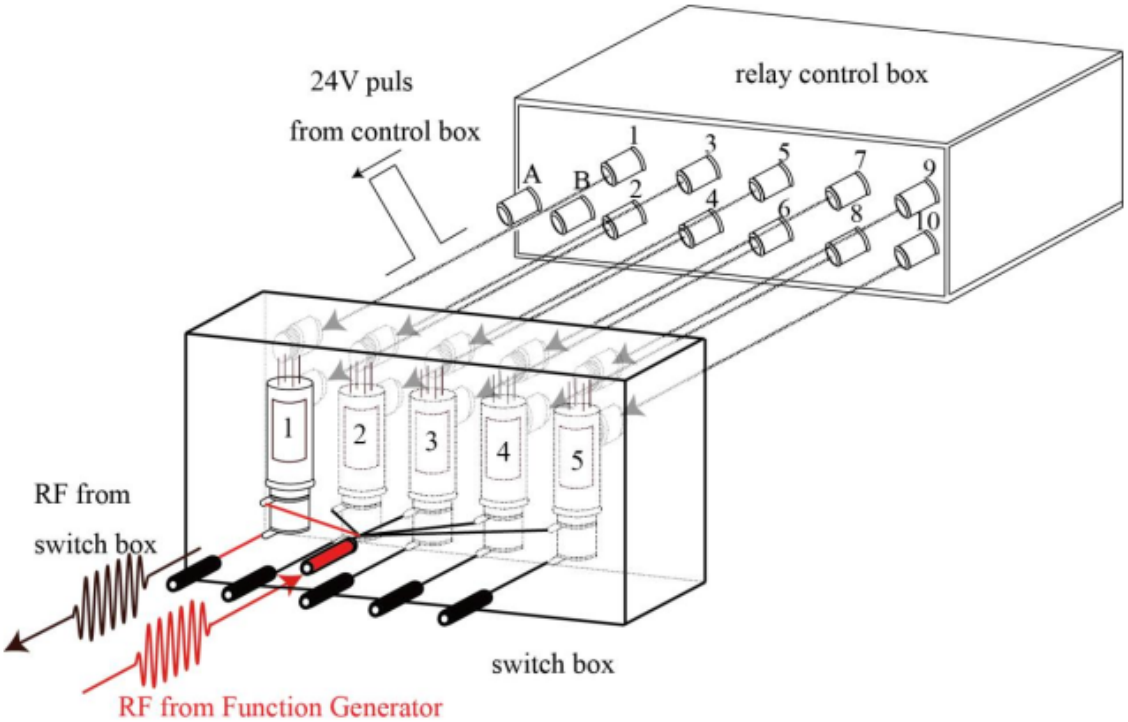

Figure 3.5: Schematic layout of fast switching system

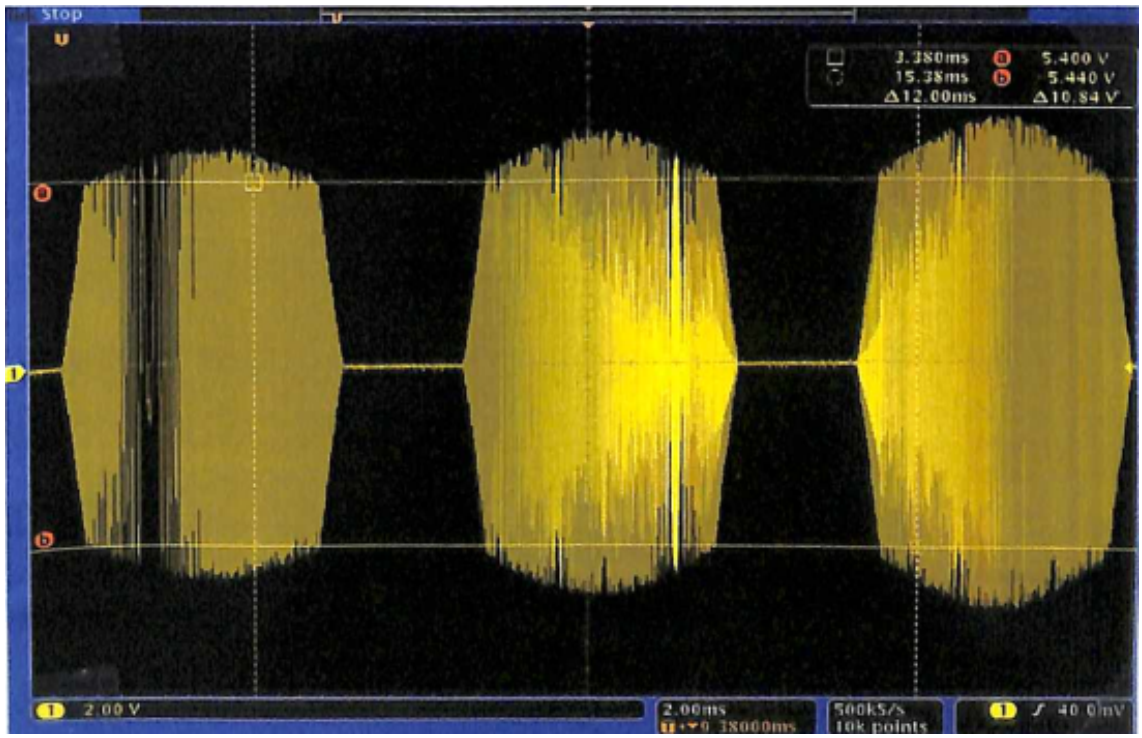

Figure 3.6: Waveform observed by the RF monitor

3.2.2 Fast switching system

In the β-NMR experiments, potential theoretical predictions are diverse when the spin-parity of the ground state of the target nucleus has not been determined. Therefore, the resonance frequency must be searched over a wide range. In addition, the time allocated for actual online experiments is limited; thus, the broadband resonance frequency region must be searched efficiently. Therefore, an RF magnetic field system equipped with multiple LCR series resonance circuits by the fast switching system was developed to search the frequency domain over a wide range in a single measurement and find the resonance point.

Note that coils with a small Q value must be used to sweep a wide frequency range using a RF magnetic field system with a conventional single LCR series resonance circuit (Fig. 3.7). However, in coils with small Q values, the RF magnetic field strength at resonance frequency cannot be obtained sufficiently, and as a result, it is necessary to lower the adiabatic condition. However, in a coil with a large Q value, even though the strength of the RF magnetic field at the resonance frequency is sufficient, the full width at half maximum of the resonance spectrum is narrowed; thus, ensuring that the adiabatic condition is satisfied over a wide frequency range is difficult. Therefore, in order to sweep a wide frequency region while satisfying the adiabatic condition, we use a coil with a large Q value by connecting a plurality of capacitors in parallel and switching using a switch shown in Fig. 3.8.

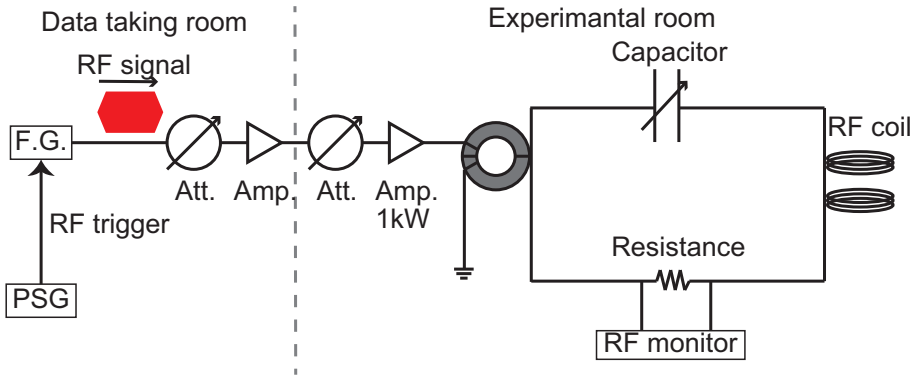

Figure 3.7: Conventional RF system

The hardware used to switch multiple capacitors in parallel is the switch and the relay box. Since the lifetime of the unstable nucleus to be measured is typically approximately 100 ms, if the switching time of the switch is long, it will collapse and sufficient β-ray yield can not be obtained. Since a high frequency of several kW is applied to the RF circuit, it is necessary not to break even when high frequency is applied. Here, a Kilovac K40P high voltage vacuum relay switch [30], which satisfies the above conditions, was used.

Connection and disconnection of the high speed changeover switch were controlled by the relay control box. To control switch connection and disconnection, a PSG signal, which is described later,

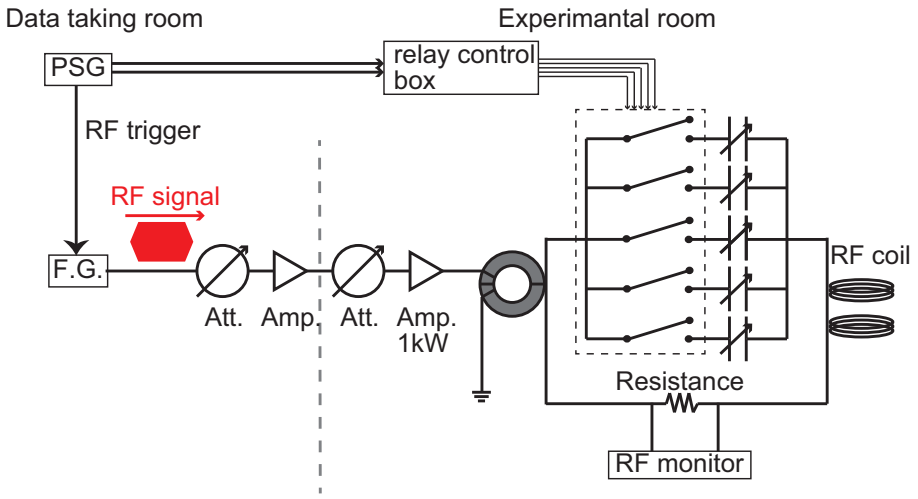

Figure 3.8: Fast switching system

is input to the relay control box, converted to the voltage required to operate the control box switch, and then sent to the switch. The relay control box is equipped with a port that can control all five switches. Using this hardware, it was possible to switch the connection to the next switch in 2.15 ms after the switching signal was input to the relay control box.

Note that the fast switch was controlled using programmable sequence generator (PSG). PSG is the hardware that controls the measurement sequence of AFR, β-NMR experiment. In addition to controlling the switch, the measurement sequence considers the on/off state of unstable nuclear beams, on/off of application of RF magnetic field, open/close of β ray measurement gate, the number of measurement frequency regions, and static magnetic field. In this experiment, PSG for AFR measurement and PSG for β-NMR measurement were prepared. The experimental operations are described in the following.

Beam gate

Beam gate defines the irradiation time of the unstable nuclear beam. By sending the negative logic signal of the beam gate to the accelerator console room as a pulsed beam signal, the pulsed unstable nuclear beam is irradiated to the stopper.

Static magnetic field B_0 sweep gate

The rotation time of the static magnetic field B_0 is defined in the AFR measurement. While this signal is being output, no beam is irradiated and β ray detection is also not performed.

Count gate

The β ray measurement time is defined. Measurement of β rays is performed while this signal is being output.

Spin Up

The direction of the irradiated polarized unstable nuclear beam is defined in the AFR measurement. The direction of the generated spin polarization is defined as upward, and when the spin direction is upward in the static magnetic field rotation, a signal is output with positive logic.

B_0 Up

The direction of the static magnetic field is defined in the AFR measurement. A signal is output with positive logic if the direction of the static magnetic field in the initial state is directed upward and, the direction of the static magnetic field is upward.

Rotation request

In the AFR measurement, the rotation request is a signal that instructs the rotation of the static magnetic field magnet. When this signal is output, the magnet rotates a half turn.

RF jump

In the β-NMR measurement, the beginning of one sequence is defined. By outputting this signal, the sequence is initialized and the measurement sequence is outputted again in chronological order. This signal also serves as an operation start command by inputting this signal to the function generator.

SW increment

In β-NMR measurement, it outputs a signal to control the connection or disconnection of the switch. By sending this signal to the relay control box, control signal is converted to a 24-V signal by the relay control box, and the connection and disconnection of the switch are controlled.

SW jump

By outputting this signal in β-NMR measurement, all the switches in the switch box are disconnected regardless of whether all switches are connected. When an SW increment is input, it controls the relay control box such that it is again connected from switch No. 1. Therefore, SW jump signal initializes the state of the switch.

RF ID

In the β-NMR measurement, the frequency region to be measured and the beta ray being measured at that time are tagged. A state in which each RF ID signal is output is defined as 1, and a state in which each RF ID signal is not output is defined as 0. A frequency measurement area is defined by a binary system by defining RF ID 1 as 2^0, RF ID 2 as 2^1, RF ID 3 as 2^2 and RF ID 4 as 2^3.

There are two types of sequences used in β-NMR measurement using a fast switching system, i.e., wide search and sequential modes.

The wide search mode uses multiple switches to widen the frequency sweeping region of a single measurement point. If this mode is applied when the target frequency sweep region extends beyond the frequency region that can be swept by the coil, it is possible to perform measurements efficiently. The measurement sequence is shown in Fig. 3.9. Prior to taking measurements, different resonance conditions were set for each capacitor in the LCR series resonance circuit in the fast switch system, as shown in Fig. 3.10. Capacitors for which resonance conditions were set were switched at high speed in order from the low frequency side to the high frequency side. Here, the switching time was sufficiently shorter than the lifetime of the nucleus to be measured. As described in Section 2.3, in the experiments, the up/down counting ratios of β rays and RF when RF is applied the resonance frequency is obtained from the up/down counting ratio of β rays when not applied. At this time, unless the measurement start times of β rays are matched between when RF is applied and when RF is not applied, bias in the count ratio appears in the measured spectrum. Therefore, the time interval at the end of the beam irradiation and the β ray counting was the same in both cases.

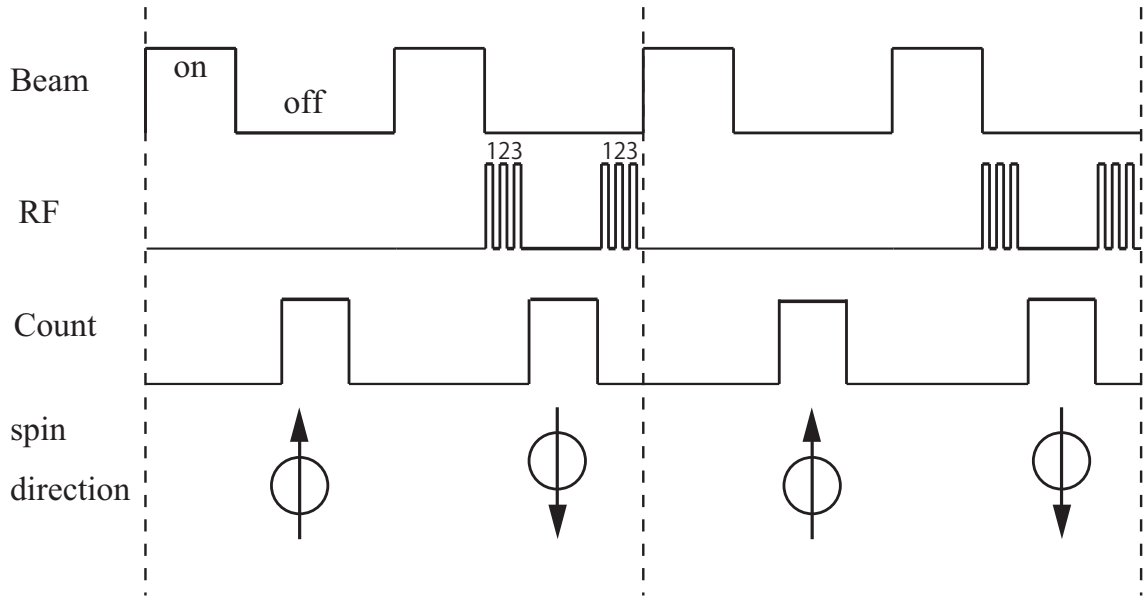

Figure 3.9: Time sequence of wide search mode

The sequential mode measures a frequency region of multiple points over a wide range using multiple switches in a single measurement. The measurement frequency width per point is the same as when not using the fast switch system; however by setting different resonance conditions for each capacitor, it is possible to increase the entire width of the frequency region to be swept by one measurement. By changing the resonance condition setting method, it is also possible to search away frequency ranges with one measurement.

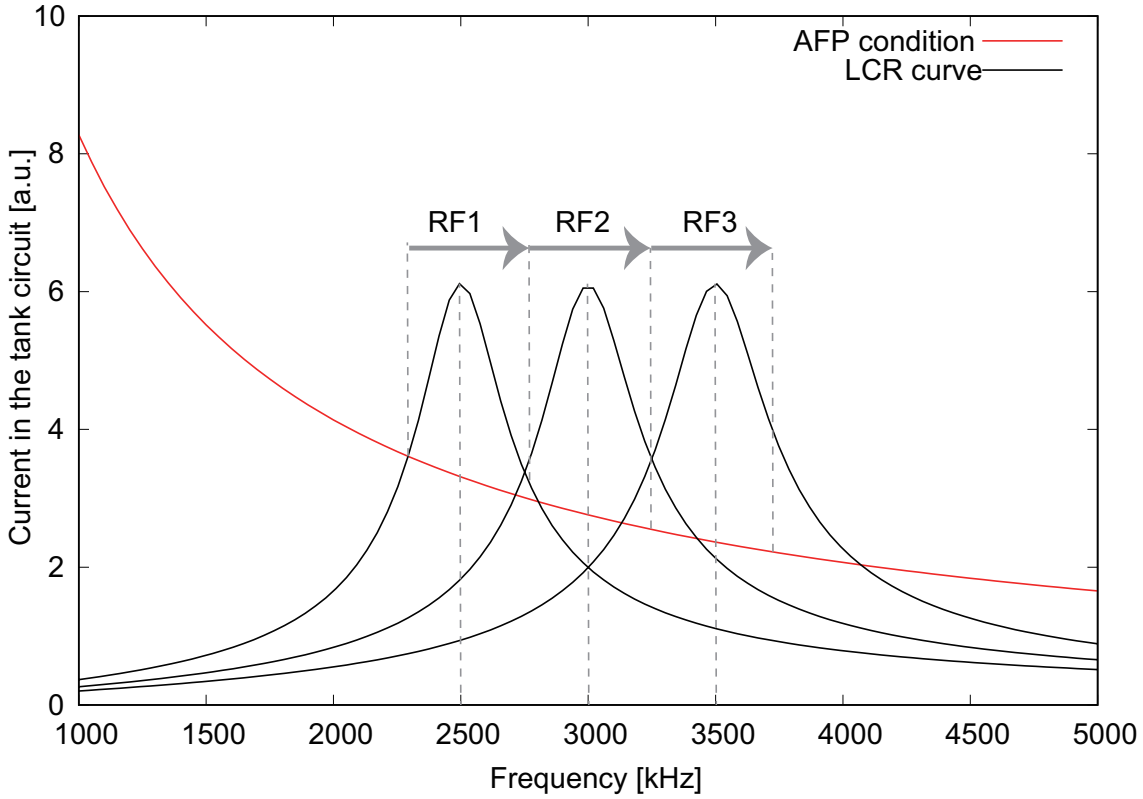

Figure 3.10: Resonance conditions that set for each capacitor in the LCR series resonance circuit in the fast switch system

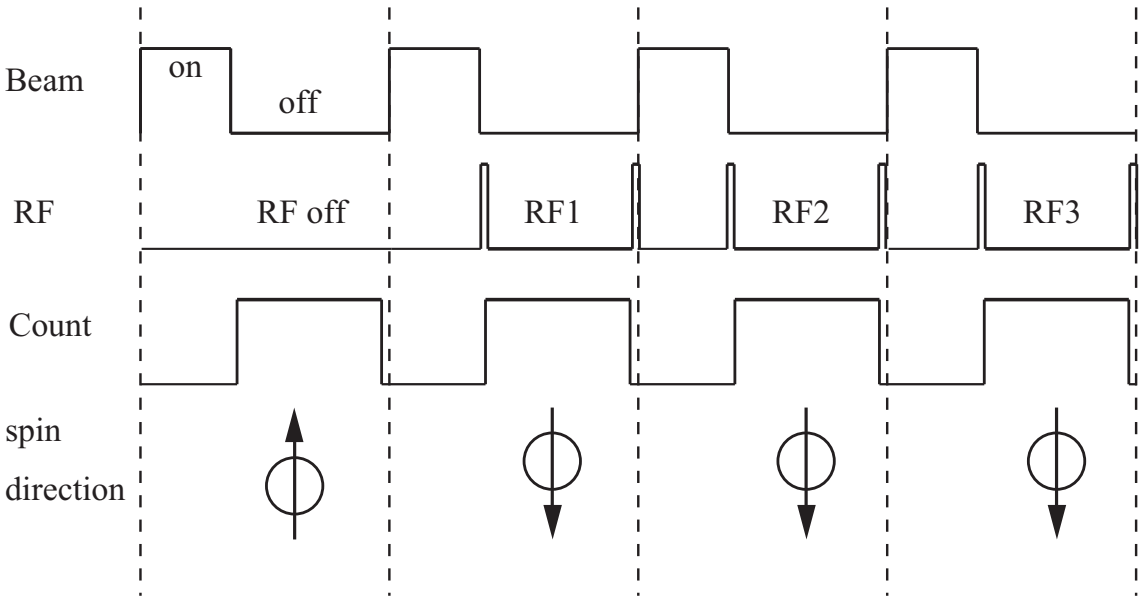

Figure 3.11: Time sequence of sequential mode

Chapter 4

Performance test of AFR system

4.1 AFR apparatus

A schematic of the AFR apparatus is shown in Fig. 4.1 [33]. The pair of Nd magnets attached to actuator is inverted by the stepping motor. The magnetic field can be adiabatically inverted in 150 ms by rotating the Nd magnets mechanically.Since the direction of the RI spin is also inverted according to the B_0 rotation, the spin polarization magnitude (more correctly, the product of the spin polarization and the β-decay asymmetry parameter) can be determined through the change in the β-ray asymmetry, as conducted in the conventional β-NMR measurements.

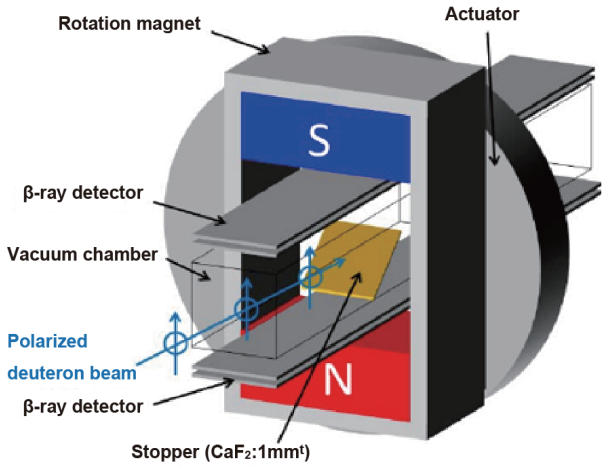

Figure 4.1: Schematic of AFR system.

In this apparatus, a static magnetic field $B_0 of \sim 300$ mT was applied by a pair of permanent Nd magnets to preserve polarization. Prior to conducting a performance test, we measured the uniformity of the magnetic field of the AFR magnet. Figure 4.2 shows the measurement results. The magnetic field at the center point of the AFR magnet was 287 mT. The deviation of the magnetic field within the target position is listed Table 4.1. From this result, the uniformity was not very good, and even within the target position (magnetic field deviation of approximately 4% at maximum occurs).

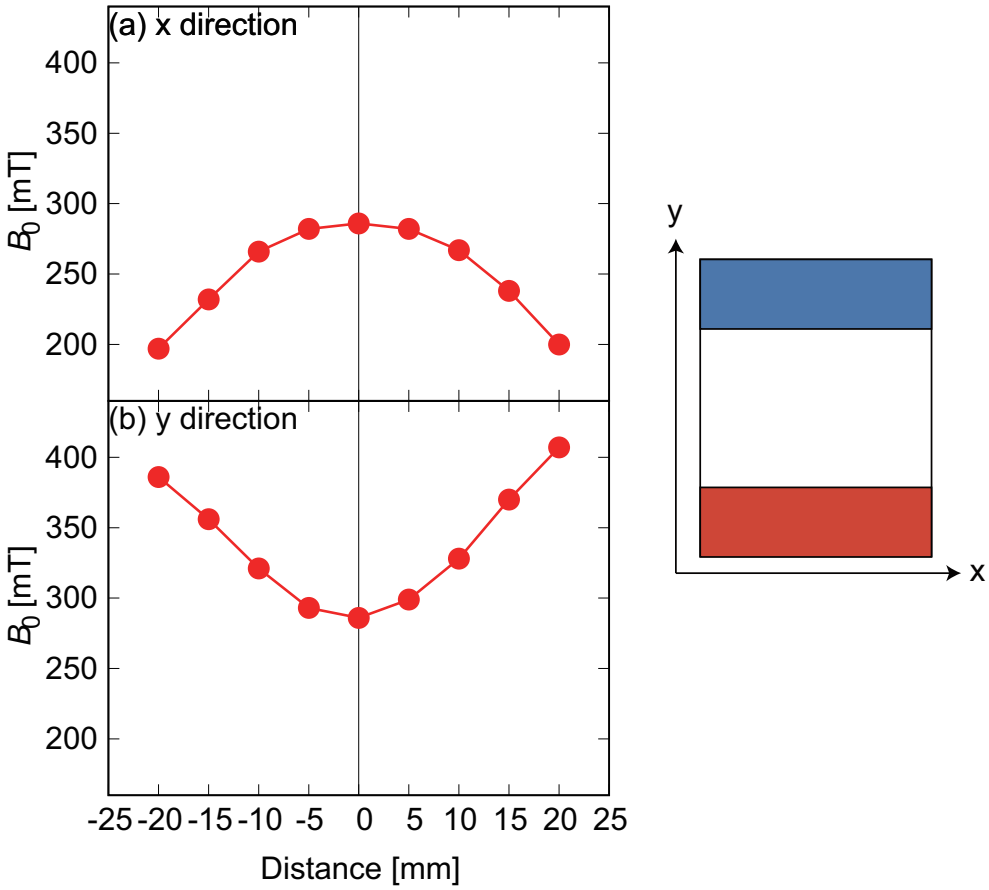

Figure 4.2: Magnetic field distribution of AFR magnet.

Table 4.1: Deviation of magnetic field within target position

Direction	Deviation [mT]	Deviation [%]
$\Delta B_{0\mathbf{X}}$	- 5.5(5)	1.9(2)%
$\Delta B_{0\mathbf{Y}}$	+ 11.0(1.0)	3.8(3)%

4.2 Experimental procedure

The performance of the system was evaluated with spin-polarized ^{20}F ($I^{\pi} = 2^{+}$, $T_{1/2} = 11.163$ s) nuclei produced in the ^{19}F($\overrightarrow{d}$,p)^{20}F reaction at $E/A = 7$ MeV at the RIBF facility. A spin-polarized $\overrightarrow{d}$ beam was provided by a polarized ion source [34] and was accelerated by the AVF cyclotron. The intensity of the $\overrightarrow{d}$ beam was typically ~ 5 nA. The beam was pulsed with beam-on and -off durations of $t_{\mathrm{on}} = 16$ s and $t_{\mathrm{off}} = 16$ s, respectively. The $\overrightarrow{d}$ beams introduced into the AFR system impinged on a stopper crystal (i.e., CaF_2 : 10 mm $\times$ 10 mm $\times$ 1 mm) placed at the center of the AFR apparatus, as illustrated in Fig. 4.3, produce the polarized ^{20}F.

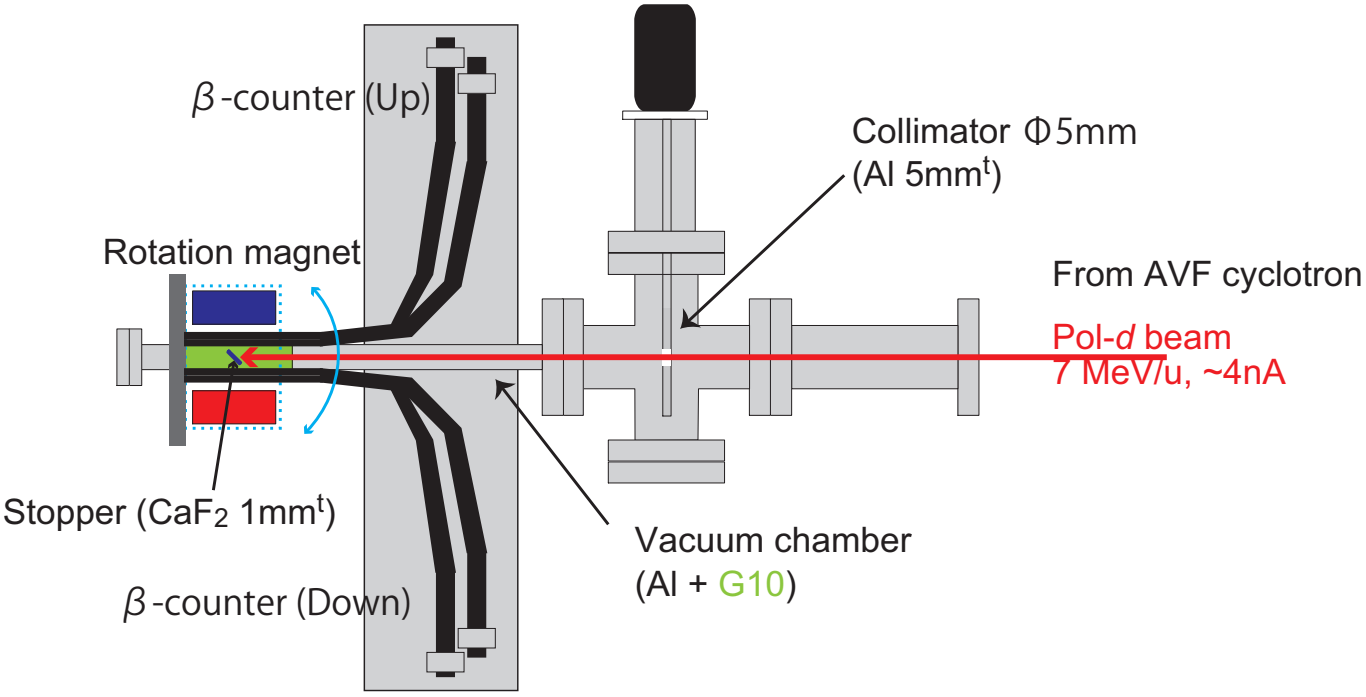

Figure 4.3: AFR apparatus for RIKEN experiment

A lifetime measurement was first conducted to investigate whether ^{20}F was produced and how pure it was. A polarization measurement was then performed using an AFR apparatus. At this time, measurements of three patterns were conducted where in the polarization direction of the beam was up, down, and non-polarized. Finally, AFP-NMR measurements were performed using this apparatus to compare the degree of polarization.

4.3 Experimental results of AFR measurement

The production of ^{20}F was identified by observing a β-ray time spectrum as shown in Fig. 4.4. The purity of ^{20}F was determined as 92.2(4)% by a least χ^2-fitting analysis with the following function:

$$f(t) = N_{^{20}\mathrm{F}} \exp\left(-\frac{\ln 2 \cdot t}{T_{1/2}(^{20}\mathrm{F})}\right) + N_{\mathrm{B.G.}}, \tag{4.1}$$

where $N_{^{20}\mathrm{F}}$ is the yield of β-rays from ^{20}F and $N_{\mathrm{B.G.}}$ is the yield of β-rays of the constant background.

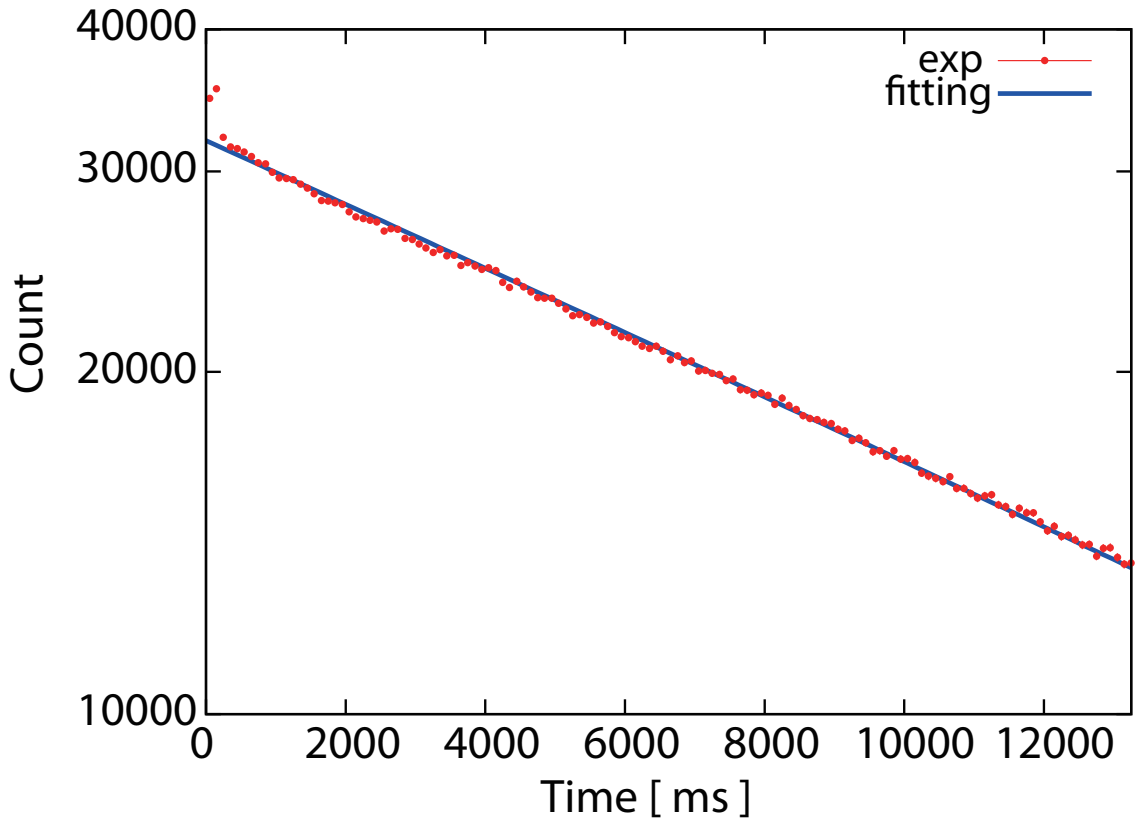

Figure 4.4: Obtained time spectrum of ^{20}F (the experiment data were fitted using Eq. 4.1)

The obtained β-ray up/down ratios r of ^{20}F with the $\overrightarrow{d}$ beams with of "up", "down", and "unpolarized" spin directions relative to the direction of the B_0 field are plotted in Fig. 4.5. Their numerical values are listed in Table 4.2.

The obtained $r = 0.992(5)$ with the "unpolarized" $\overrightarrow{d}$ beam indicates deviation from unity (i.e., $r = 1$) caused by the effect of the B_0 field rotation on the efficiency changes of the PMTs connected to the plastic scintillators. The efficiency difference of the β-ray telescopes can be canceled according to Eq. 3.4 in the AFR method. In this measurement, however, the shift in the R spectra was caused by dynamical efficiency changes of the telescopes due to the rotating strong B_0 field. We note that

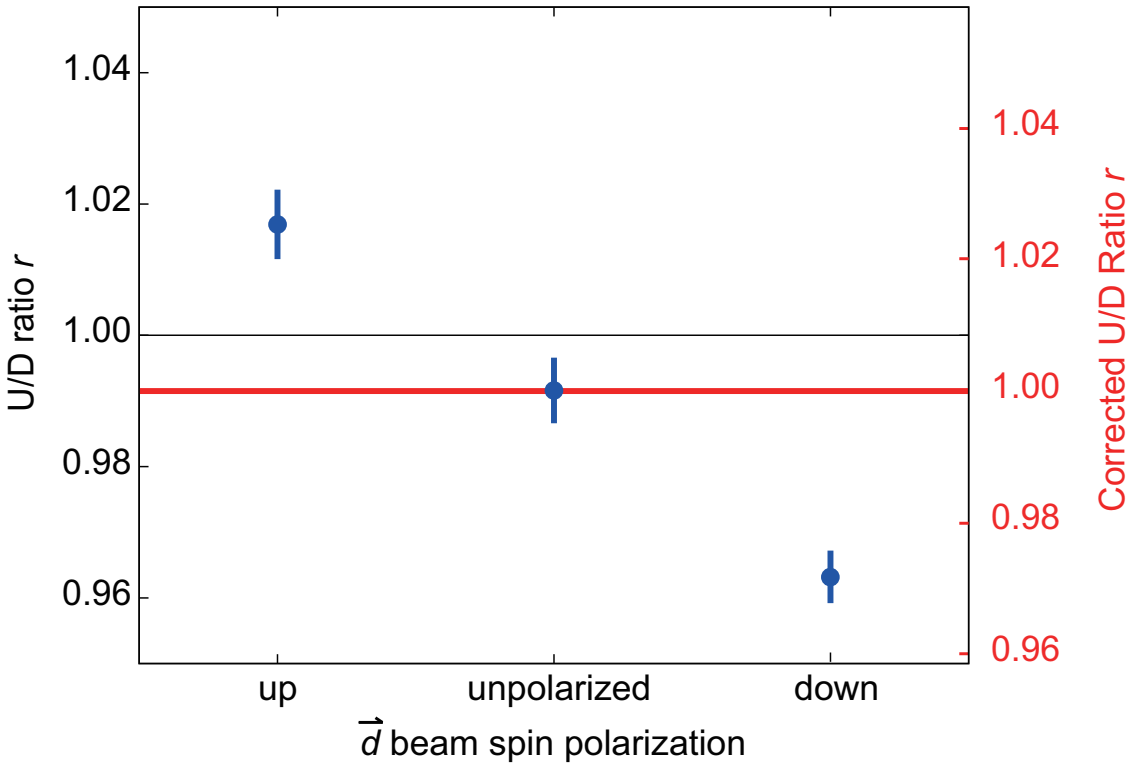

Figure 4.5: Obtained polarization of ^{20}F. The left axis shows uncorrected, and the right axis and red values show the corrected spin polarizations. For the correction, see the text.

Table 4.2: Obtained degree of spin polarization of ^{20}F

	up/down ratio r			
$\vec{d}$ beam polarization	uncorrected	corrected	$A_\beta P$	$P_{\rm correct}$
up	1.017(5)	1.025(5)	0.3(1)%	1.5(3)%
unpolarized	0.992(5)	1.000(5)	0.0(1)%	0.0(4)%
down	0.963(4)	0.972(4)	-0.4(1)%	-1.7(3)%

this effect can be minimized by introducing magnetic shielding at the PMTs.

Corrected r values, calculated taking the $r = 0.992(5)$ effect as a common baseline shift, are also expressed on the right axis in Fig. 4.5. Spin polarization of ^{20}F, determined by adopting these corrected $A_\beta P$ values, are listed in Table 4.2, where i) the asymmetry parameter of the ^{20}F β-decay, $A_\beta = 1/3$, ii) the solid angle of detectors, $\Omega = 0.70(5)$, and iii) the observed purity of ^{20}F β-rays, 92.2(4)%, were considered. The resulting spin polarizations were $P_{\rm up} = 1.5(3)\%$, $P_{\rm unpolarized} = 0.0(4)\%$, and $P_{\rm down} = -1.7(3)\%$.

Taking the weighted average of $|P|$ values of the "up" and "down" beam polarizations, we obtained $|P| = 1.6(2)\%$. It has been reported in the literature [35] that the spin polarization $P(^{20}\mathrm{F}) \sim 3\%$ was measured using the β-NMR method under typical beam polarization of 72%. The $\vec{d}$ beam polarization was derived as approximately ~40% by simply scaling the presently obtained $|P(^{20}\mathrm{F})| = 1.6(2)\%$.

Chapter 5

Performance tests of New AFR/AFP system

When measuring the magnetic moment of ^{21}O, a performance test was performed using ^{21}F nuclei previously produced and measured by RIPS. The results are reported in this chapter.

5.1 New AFR apparatus using Halbach type magnet

As discussed in Chapter 4, the degree of polarization obtained by the AFR measurement was smaller than that of the previous study. As one factor, the difference in polarization of the beam has been described previously; however, the possibility that the holding magnetic field was small is another possible factor. Therefore, we have been developing a new AFR device in which permanent magnets are arranged in a Halbach array [37] of rotating magnets in an AFR apparatus that used opposing permanent magnets. Figure 5.1 shows the layout of a Halbach type magnet.

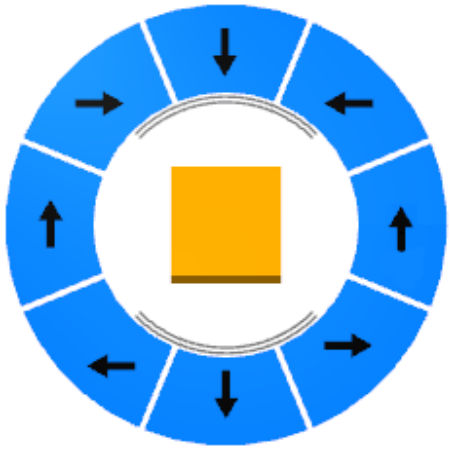

Figure 5.1: Layout of a Halbach type magnet

The results of the magnetic field measurement inside this magnet are shown in Fig. 5.2. With the central magnetic field of 481 mT, the uniformity of the magnetic field was 5 mT/10 mm in the x direction, 30 mT/10 mm in the y direction and approximately 40 mT/10 mm in the z direction. Since the stopper was tilted at 45 degrees vertically by 28 mm and laterally by 20 mm, uniformity within $\pm$10 mm is important. In the previous hyperbolic type magnet, there was a deviation of 10% or more in the range of $\pm$10 mm; however, by changing this magnet, deviation was 8% at maximum.

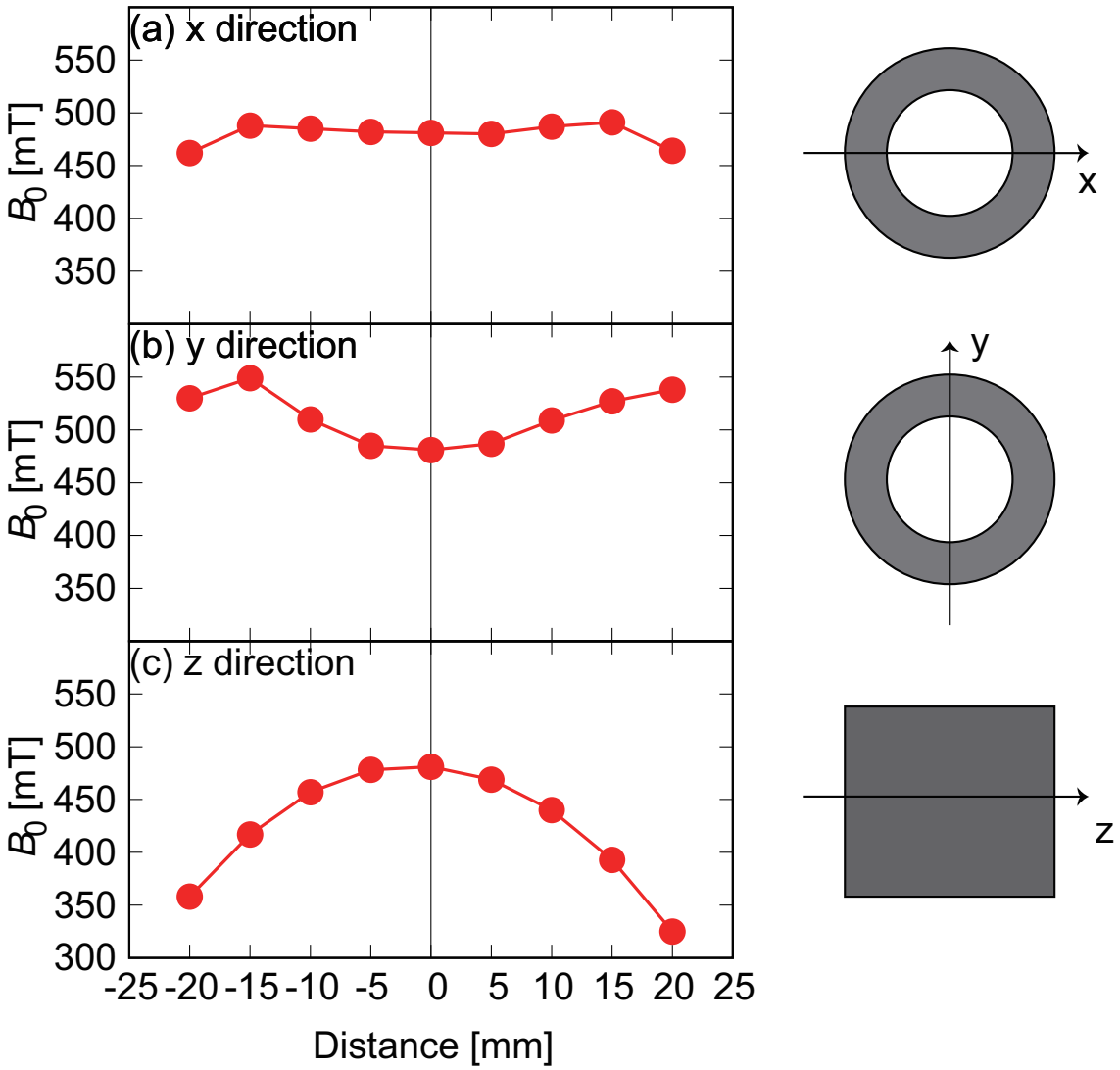

Figure 5.2: B_0 distribution

The rotation of the magnet uses the TTL signal output from the PSG. Figure 5.3 shows the circuit diagram for the magnet rotation control. The TTL signal of the rotation command output from the PSG is input to a control box for signal processing. The control box is connected to the control PC via a USB cable, and the command to initialize the rotation time and magnet position can be issued using the control PC. The rotation command signal output from the control box is connected to the magnet rotation motor in the AFR apparatus, and the signal is input to the motor, whereby the magnet rotates by 180°. To prevent malfunction, the control box is programmed to not accept the TTL signal more than once per second. In addition, an origin sensor is installed inside the AFR apparatus. When the command to initialize the magnet position is issued from the control PC, initialization of the magnet position and a return to origin are performed using the origin sensor. A light sensor is installed inside the AFR device to confirm that the magnet has rotated by 180°. When the magnet rotates 180°, the light output from one of the optical sensors is detected by the other sensor. The TTL signal is output when rotation detection is performed by the sensor. In the experiment, the number of the rotation request and the rotation detection signals from the PSG were monitored constantly, and an experiment was conducted while confirming that there was no deviation. In addition, when the magnet becomes uncontrollable, an emergency stop switch is connected to the control box to forcibly stop the magnet rotation.

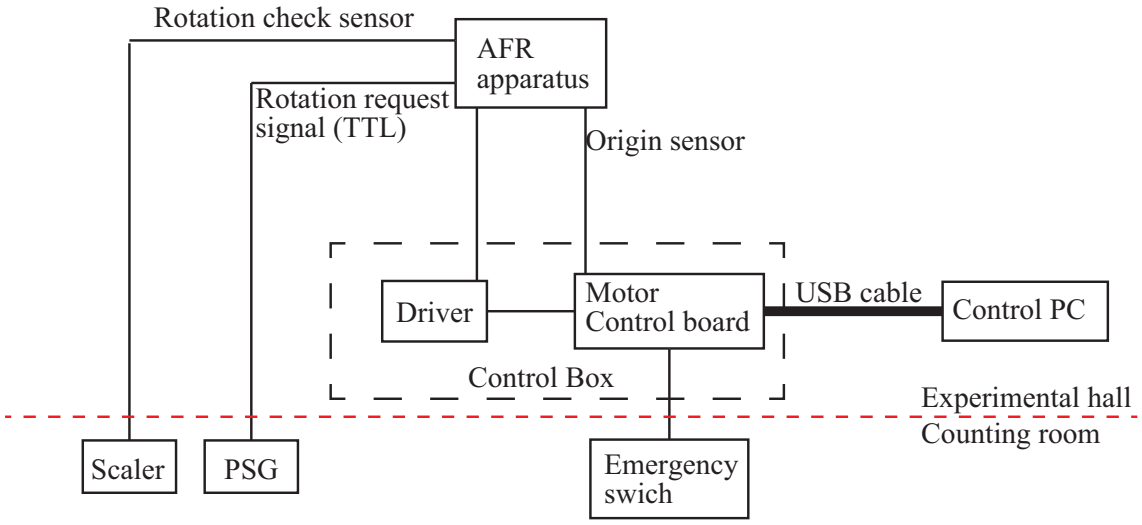

Figure 5.3: Circuit of rotation magnet system

5.2 Time spectra of ^{21}F

First, lifetime measurement was conducted to confirm the production of ^{21}F. The results are shown in Fig. 5.4. The red circle in the figure shows the experimental data, the black line shows the fitting curve,

$$f(t) = N_{^{21}\mathrm{F}} \exp\left(-\frac{\ln 2 \cdot t}{T_{1/2}(^{21}\mathrm{F})}\right) + N_{\mathrm{B.G.}}, \tag{5.1}$$

and the blue line shows the proportion of ^{21}F in the whole. From this fitting result, the purity of ^{21}F was 84.3 (1.1)%.

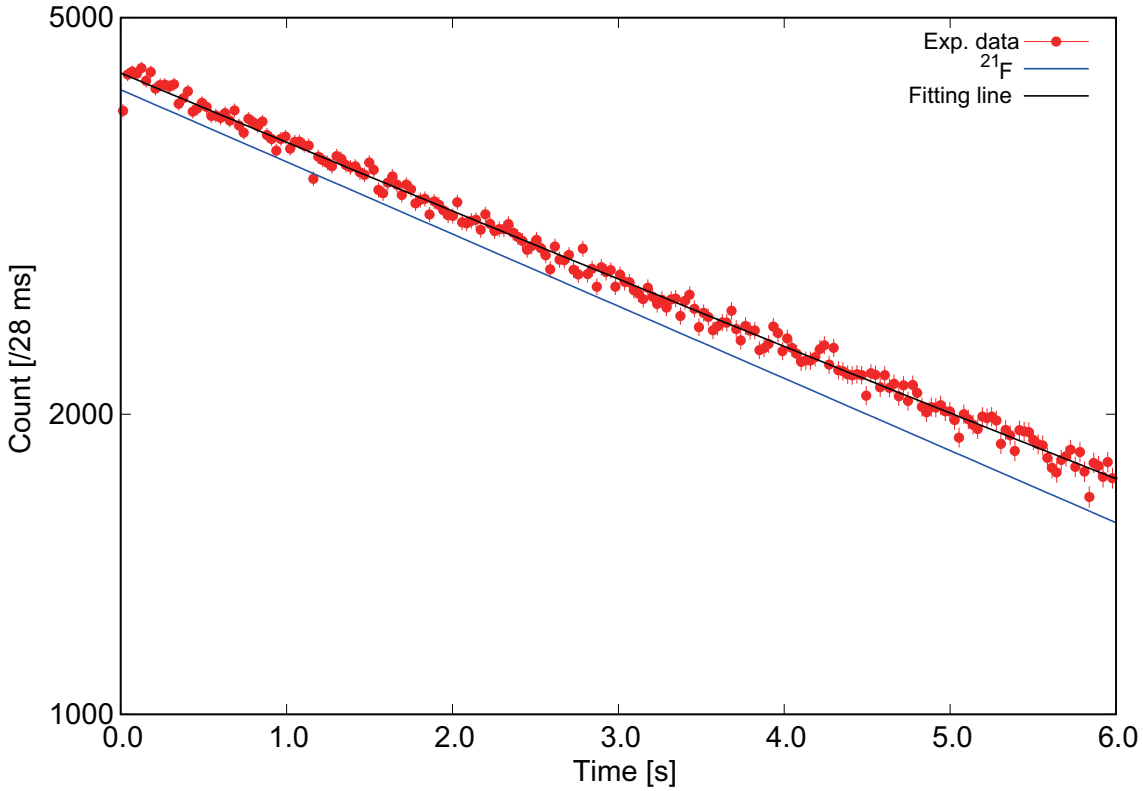

Figure 5.4: Time spectrum of ^{21}F

Table 5.1: Least square fitting results of time spectrum of ^{21}F

$N_{\mathrm{B.G.}}$	166(13)
$N_{^{21}\mathrm{F}}$	4233(21)
$T_{1/2}(^{21}\mathrm{F})$	4158
χ^2	1.06

5.3 AFR measurement

In the AFR measurement, several conditions were changed and several measurements were performed. The yield, polarization, and FOM results are shown in Fig. 5.5, and the conditions are summarized in Table 5.2. The results demonstrate that although it was possible to observe the degree of polarization even under conditions, the degree of polarization was optimal under condition #4. Therefore, subsequent NMR measurements, proceeded under these conditions.

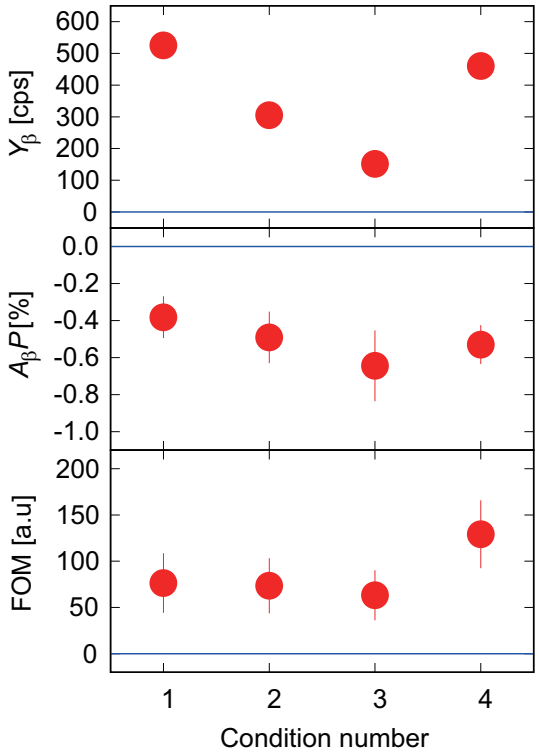

Figure 5.5: Summary of AFR measurement of ^{21}F

Table 5.2: Conditions of AFR measurement of ^{21}F (p_c is the center of momentum (= $(p_{\mathrm{F}} - p_{\mathrm{Beam}})/p_{\mathrm{Beam}}$))

#	Selected momentum	Selected angle	Beam on/off period	Y_β	AP [%]
1	$1.5\% < p_c < 2.5\%$	$1.6^\circ < \theta < 5.9^\circ$	6 s / 6 s	525(23) cps	-0.38(11)
2	$1.5\% < p_c < 2.5\%$	$1.6^\circ < \theta < 5.9^\circ$	2 s / 10 s	305(17) cps	-0.49(14)
3	$1.5\% < p_c < 5.0\%$	$2.1^\circ < \theta < 5.9^\circ$	2 s / 10 s	152(12) cps	-0.64(19)
4	$1.5\% < p_c < 5.0\%$	$1.6^\circ < \theta < 5.9^\circ$	6 s / 6 s	469(22) cps	-0.53(11)

5.4 β-NMR measurement

Before using the fast switch system, measurements were conducted using the conventional system as the comparison target. Although the magnetic moment measurement of ^{21}F was previously performed in this system, it is measured under slightly different conditions such as beam energy and target thickness. The details of beam conditions are given in the appendix.

5.4.1 β-NMR measurement using the conventional system

A conceptual diagram of the RF system in the conventional system is shown in Fig. 5.6. Only one variable capacitor is used in the conventional system. To adjust the capacitance of the capacitor, a variable vacuum condenser with a motor (Meidensha corp.) was used.

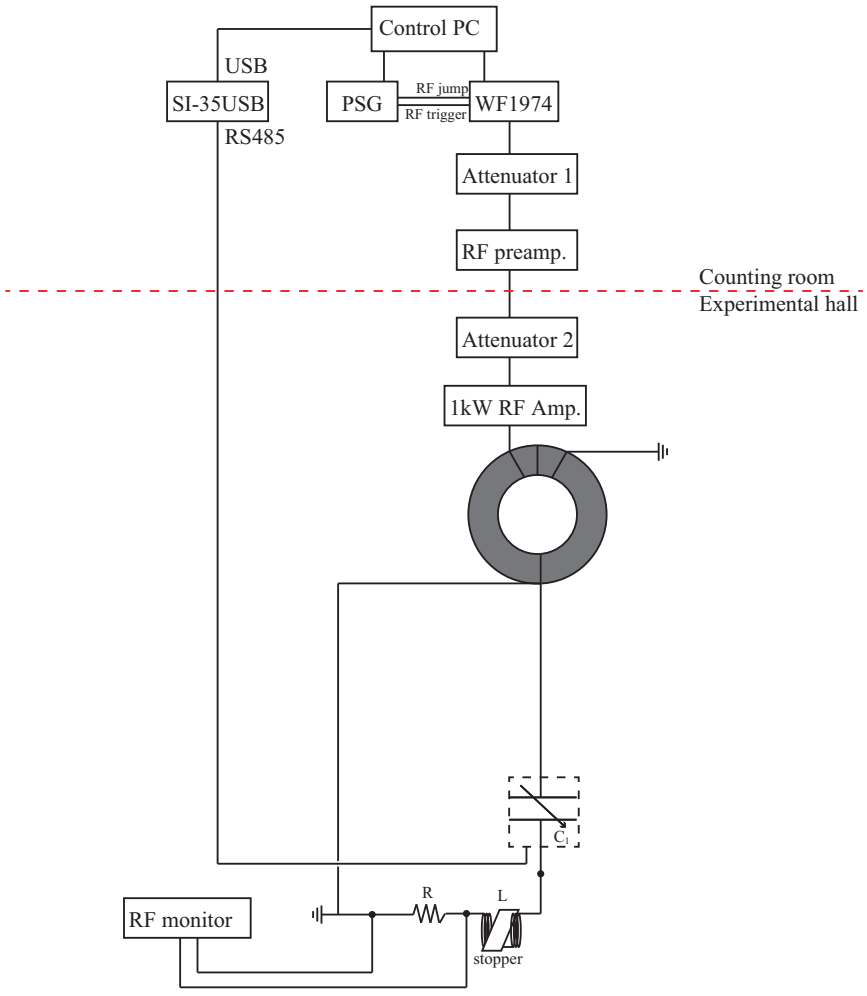

Figure 5.6: Conventional RF magnetic field application system

The magnetic moment of ^{21}F is $|\mu(^{21}\mathrm{F}{:}5/2^{+})| = 3.9194(12)\ \mu_{\mathrm{N}}$ [38], and the g-factor becomes $|g| = 1.5678(5)$. As described previously, in the conventional system, frequency sweeping is performed using only one condenser; thus, three measurements are performed in sequence. This was done to take measurements in the wide search mode at three points. The measurement results are shown in Fig. 5.7.

Here, since the external magnetic field was set to 100.62(1) mT, which is comparable to that of a previous study, and RF was applied at a resonance frequency of 1201.37 kHz. Compared to the degree of polarization in the AFR measurement, here the degree of polarization was small because the holding magnetic field was insufficient or the RF magnetic field did not sufficiently satisfy the AFP condition.

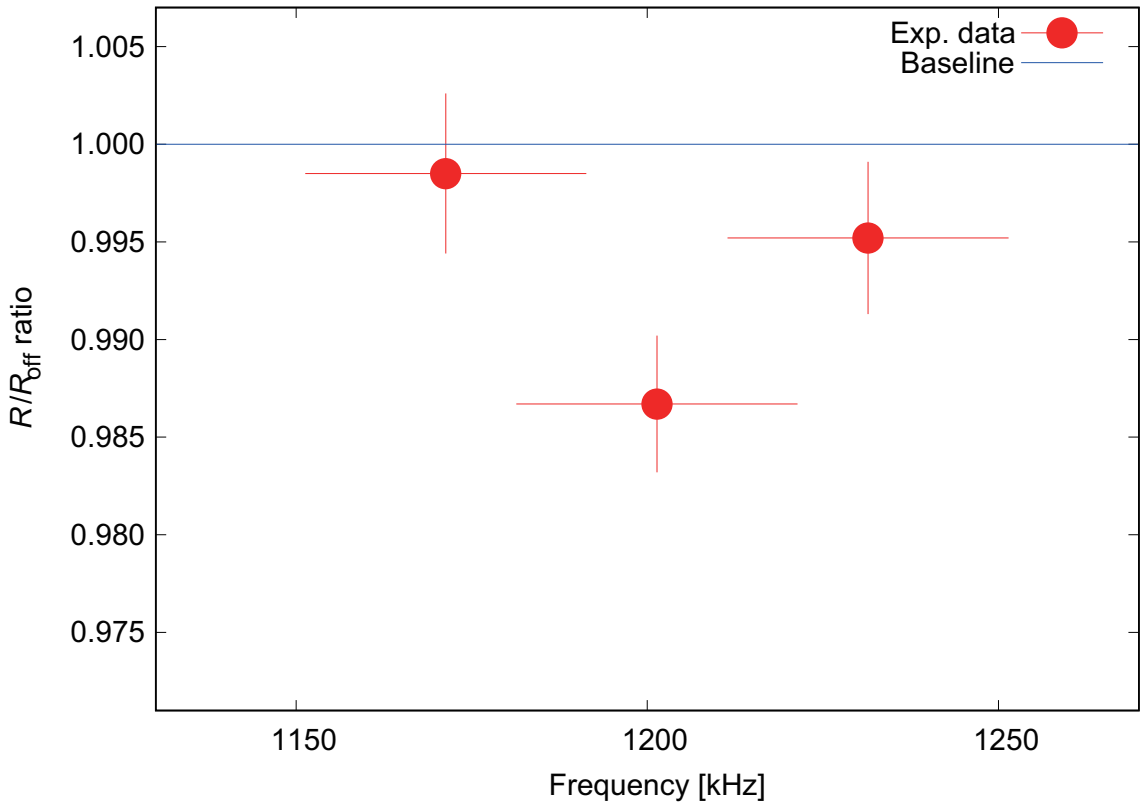

Figure 5.7: Results of NMR measurement of ^{21}F using conventional system

5.4.2 β-NMR measurement using the new RF system

A conceptual diagram of the new RF system is shown in Fig. 3.3. As can be seen, three variable capacitors are connected in parallel, and two ceramic capacitors are connected to correspond to RF in the low frequency range. With this system, measurements were first taken in wide search mode, and the results are shown in Fig. 5.8. The applied frequencies are summarized in Table 5.3. In this mode, the RF of the three regions shown in the figure was applied continuously; thus even when resonance was observed, it could not be determined in which region the resonance frequency exists. (However, in the case of ^{21}F, since the magnetic moment is already known, it is known that there is a resonance frequency in the center region from the beginning.) Therefore, when resonance was observed, it was necessary to measure the same region in sequential mode.

Table 5.3: Relationship between applied frequency and g-factor

RF #	frequency (kHz)	g-factor
1	1147.31–1165.33–1183.35	1.4959–1.5194–1.5429
2	1183.35–1201.37–1219.39	1.5429–1.5664–1.5899
3	1219.39–1237.41–1255.43	1.5899–1.6134–1.6369

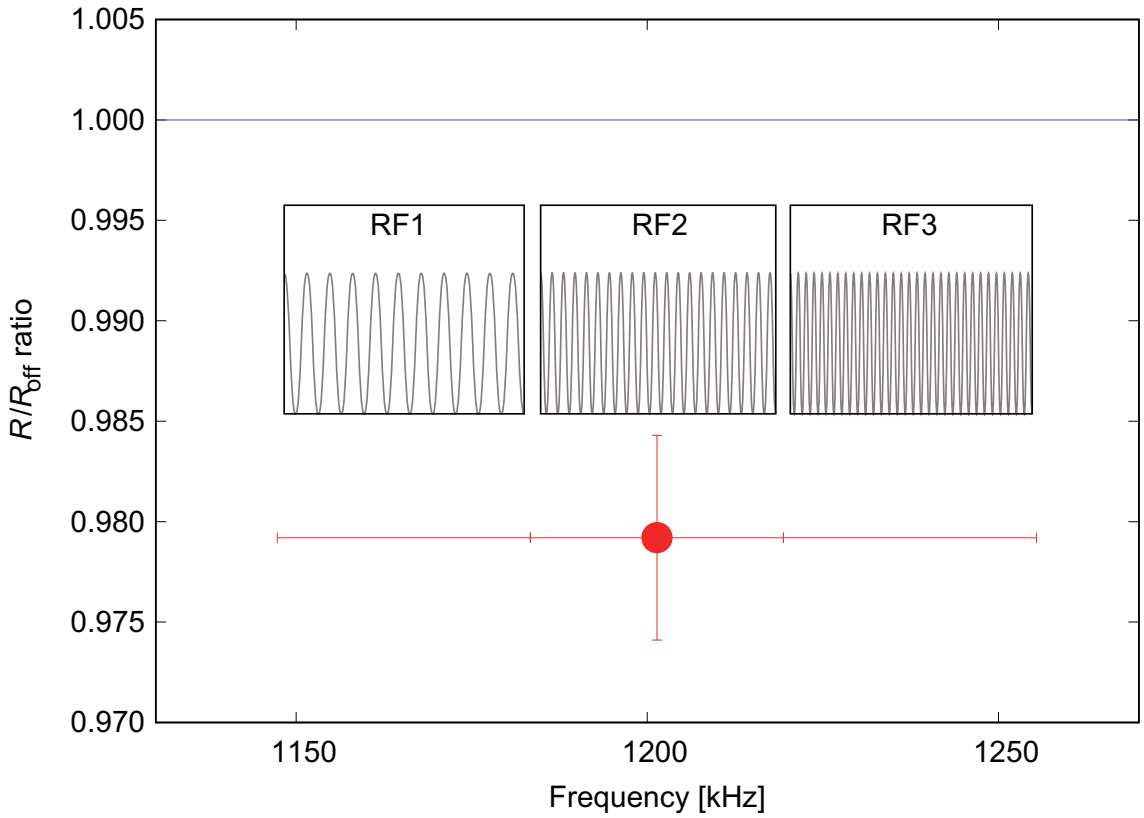

Figure 5.8: Result of wide search mode NMR measurement of ^{21}F. The wavy lines are an example of frequency.

As described above, the measurement was performed in sequential mode, and the results are shown in Fig. 5.9. Here, the frequency deviates from that in the above-mentioned wide search measurement (Fig. 5.8) because the static magnetic field, which is an input parameter of the RF system, was erroneously input at 100.0 mT (it should be 100.6 mT). The applied frequencies are summarized in Table 5.4. As a result, the frequency shifted to the lower frequency side, and as a result, the resonance frequency was also included at the point on the high frequency side; therefore resonance was observed at two points.

Table 5.4: Relationship between applied frequency and g-factor in wide search mode

RF #	frequency (kHz)	g-factor
1	1140.26–1164.16–1184.06	1.5011–1.5272–1.5533
2	1174.11–1194.01–1213.91	1.5403–1.5664–1.5925
3	1203.96–1223.86–1243.76	1.5795–1.6056–1.6317

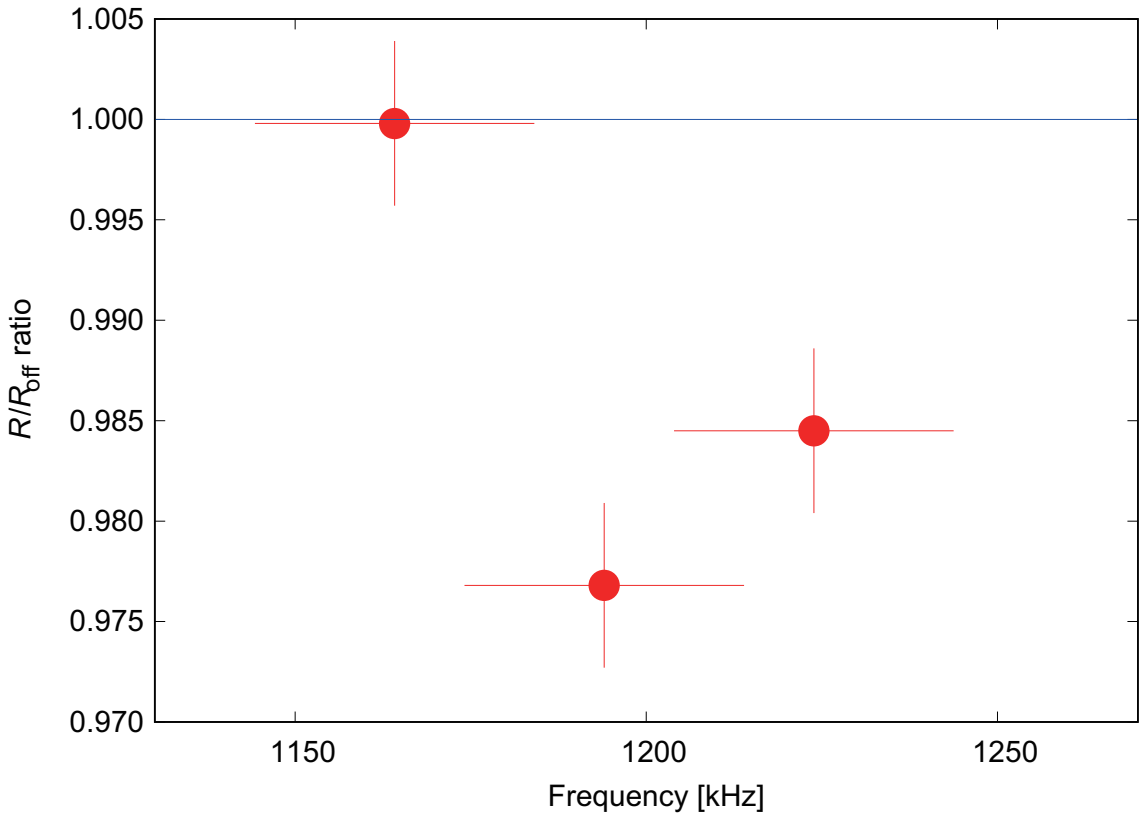

Figure 5.9: Result of sequential measurement of ^{21}F

Figure 5.10 compares the measurement results of the conventional and new systems. As can be seen, the R/R_{off} ratio value matches on the point on the low frequency side, but it does not match even in the range of error at the other two points. Relative to the point on the high frequency side, the R/R_{off} ratio became small because RF with the resonance frequency was applied in the new

system. For the central point, the polarization degree $A_\beta P$ of the new system was -0.59(10)%, and the polarization degree at AFR (Table 5.2) could be reproduced.

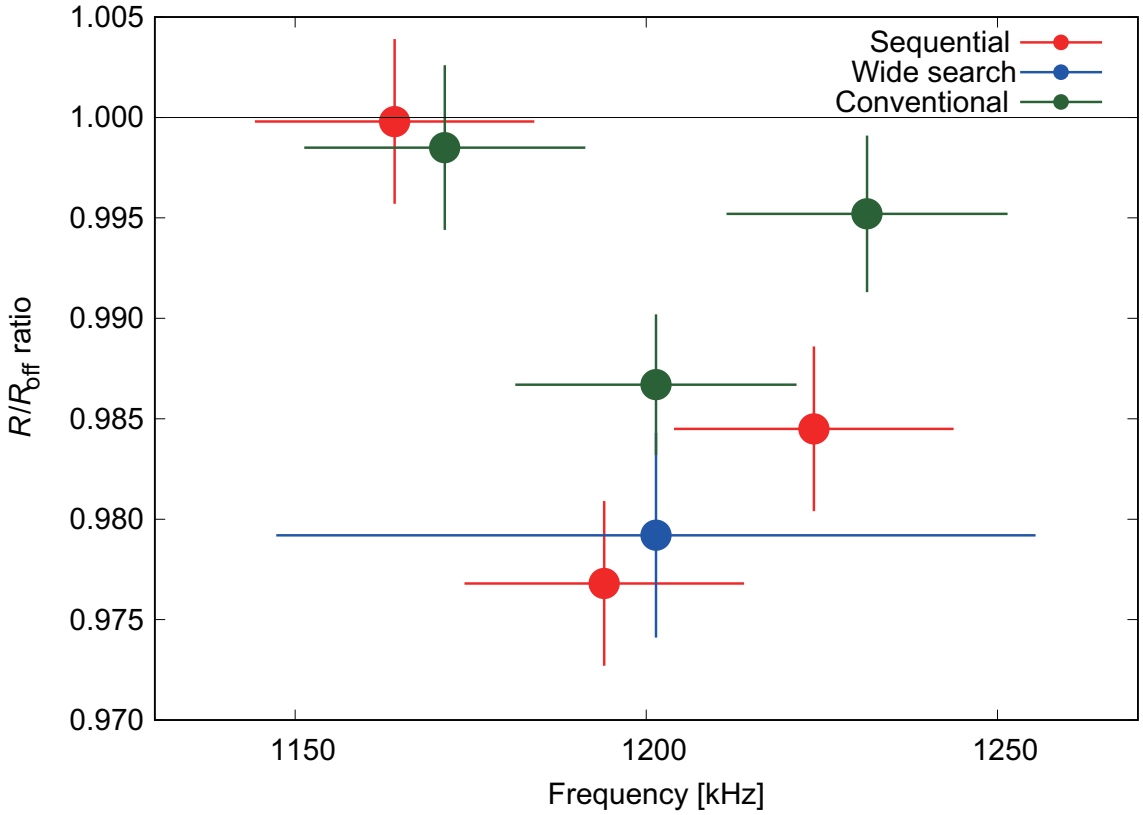

Figure 5.10: Comparison of measurements of conventional and new systems at $B_0 \sim 100$ mT

Therefore, it was confirmed that the new system works without problem and that measurement up to 100 mT (for comparison with previous work) has been realized. Then, β-NMR measurement was started again by changing the static magnetic field to 500 mT, which is nearly equal to the magnetic field of the new AFR apparatus.

5.4.3 Precise measurement of ^{21}F

After changing the magnetic field, three points were measured in the same g-factor region, as in Table 5.4, and it was confirmed that the same result shown in Fig. 5.9 was obtained. Here, the magnetic field of this measurement was 500 mT; thus, frequency search was performed with 500 mT at the input of RF. The applied frequencies are summarized in Table 5.5, and the results are shown in Fig. 5.11. As can be seen, polarization was observed only at the center point and that polarization is smaller as compared with the case of $B_0 \sim 100$ mT. This is considered to be caused by the fact that the holding magnetic field was insufficient at 100 mT and a large magnetic field of approximately 500 mT was required to preserve polarization.

Table 5.5: Relationship between applied frequency and g-factor in sequential mode

RF #	frequency (kHz)	g-factor
1	5721.31–5820.81–5920.31	1.5011–1.5272–1.5533
2	5870.56–5970.06–6069.56	1.5403–1.5664–1.5925
3	6019.82–6119.32–6218.82	1.5795–1.6056–1.6317

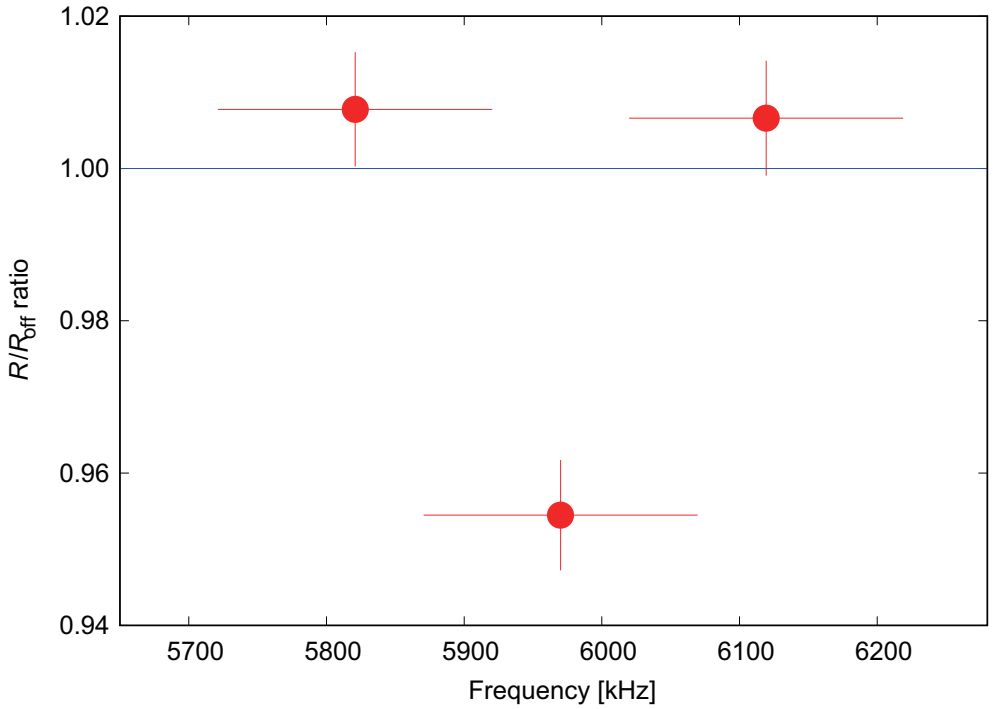

Figure 5.11: Three-point measurement of ^{21}F @ $B_0 \sim 500.0$ mT

Finally, a precise 15-point measurement was performed. Here, frequency search was performed with an overlap of 0.03%, with 1% width centered on g-factor = 1.5664. The results are shown in Fig. 5.12.

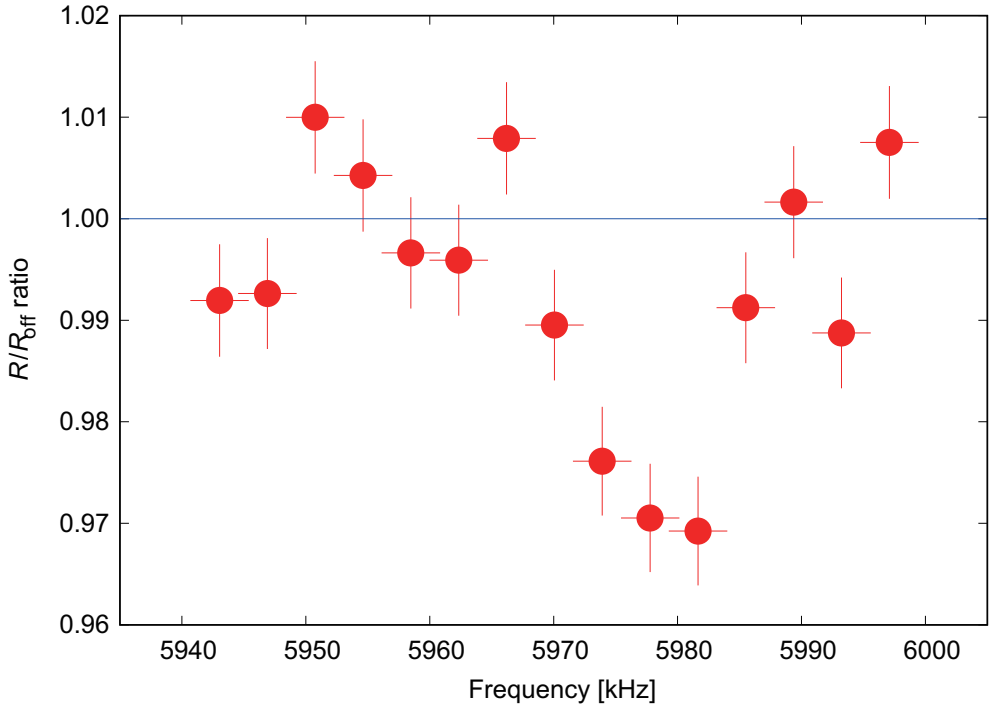

Figure 5.12: Result of precise measurement of ^{21}F

5.5 Derivation of magnetic moment of ^{21}F

Since the resonance peak can be observed by precise measurement, the resonance frequency was obtained by fitting using the least squares method. Here, for the original function, we simulated the inversion rate of AFP and found the applicable function. See the appendix for details. Figure 5.13 shows the final result and the fitting curve. The fitting results are given in Table 5.6. Here, A_0 is the $R/R_{\rm off}$ ratio, x_0 is the center frequency, and $\sigma_{\rm EB}$ is the extra broadening width. Based on the

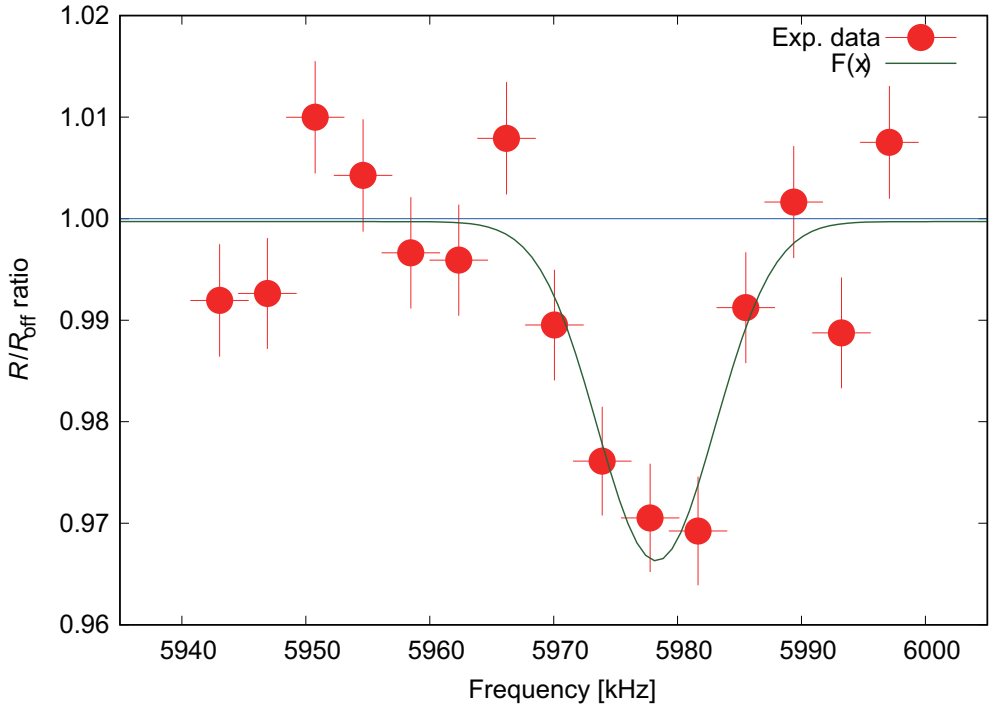

Figure 5.13: Fitting results of precise measurement of ^{21}F

Table 5.6: Results of experimental data fitting

A_0	-0.073 ± 0.018
x_0	5978.28 ± 1.38
$\sigma_{\rm EB}$	4.45 ± 1.32
Baseline	0.9997 ± 0.0025
Reduced χ^2	1.787

above analysis, the center frequency was obtained as follows:

$$\nu_{\rm L} = 5978.28 \pm 1.38(\text{statistic error}) \pm 4.45(\text{systematic error}).$$

Since the spin of ^{21}F is $5/2^+$ and the magnetic field at the end of experiment was 500.86 (1) mT, the magnetic moment was derived as follows:

$$\begin{aligned} |g| &= \frac{h\nu_0}{\mu_{\rm N} B_0} \\ &= 1.5659 \pm 0.0004(\text{sta.}) \pm 0.0012(\text{sys.}). \end{aligned} \tag{5.2}$$

$$\begin{aligned} |\mu_{\rm uncorrect}| &= g\mu_{\rm N} I \\ &= (1.5659 \pm 0.0004 \pm 0.0012) \times \frac{5}{2} \times \mu_{\rm N} \\ &= 3.9147 \pm 0.0009 \pm 0.0029 \mu_{\rm N} \\ &= 3.9147 \pm 0.0031 \mu_{\rm N}. \end{aligned} \tag{5.3}$$

Chapter 6

Experimental procedure

This experiment was conducted at the RIKEN Radioactive Isotope Beam Factory (RIBF). ^{22}Ne accelerated to $E/A = 70$ MeV was injected into ^{9}Be to produce ^{21}O by projectile fragmentation reaction and nucleon pick-up reaction. The produced nuclear beams were separated using RIKEN Projectile Fragment Separator (RIPS) [39], and the produced ^{21}O was led to an AFR apparatus located downstream of RIPS, and the degree of polarization was measured using the AFR method. Then, the setup of the final focal plane was changed from the AFR apparatus to the β-NMR apparatus, and the magnetic moment measurement was conducted using the β-NMR method. This chapter describes the experimental procedure.

6.1 Description of RIPS

A ^{22}Ne beam accelerated up to $E/A = 70$ MeV in the ring cyclotron accelerator (RIKEN Ring Cyclotron, RRC) with the AVF accelerator as the front stage collides with the target nucleus ^{9}Be.To separate the target nuclei from various fragments produced by subsequent projectile fragmentation and nucleon pick-up reactions, a projectile fragment separator RIPS was used. An overview of RIPS is shown in Fig. 6.1. Beam swingers are installed upstream of the RIPS target chamber. The fragments produced using the bipolar electromagnet inside the swinger are bent and made to enter the target at an angle of 15° at maximum. The swinger and slit on the downstream side of the target are combined to select the emission angle. Then, the following steps were conducted to select only the target nuclei from the produced fragments.

Separation of dipolar electromagnet D1

The velocity of the fragments produced by the projectile fragmentation reaction was nearly equal to velocity v of the incident particles. Therefore, assuming that the magnetic field B is applied by the dipole electromagnet D1, the motion equation of the particle with atomic number Z and the mass number A in this magnetic field is as follows:

$$Am_{\mathrm{N}}\frac{v^2}{\rho_1} = ZevB \tag{6.1}$$

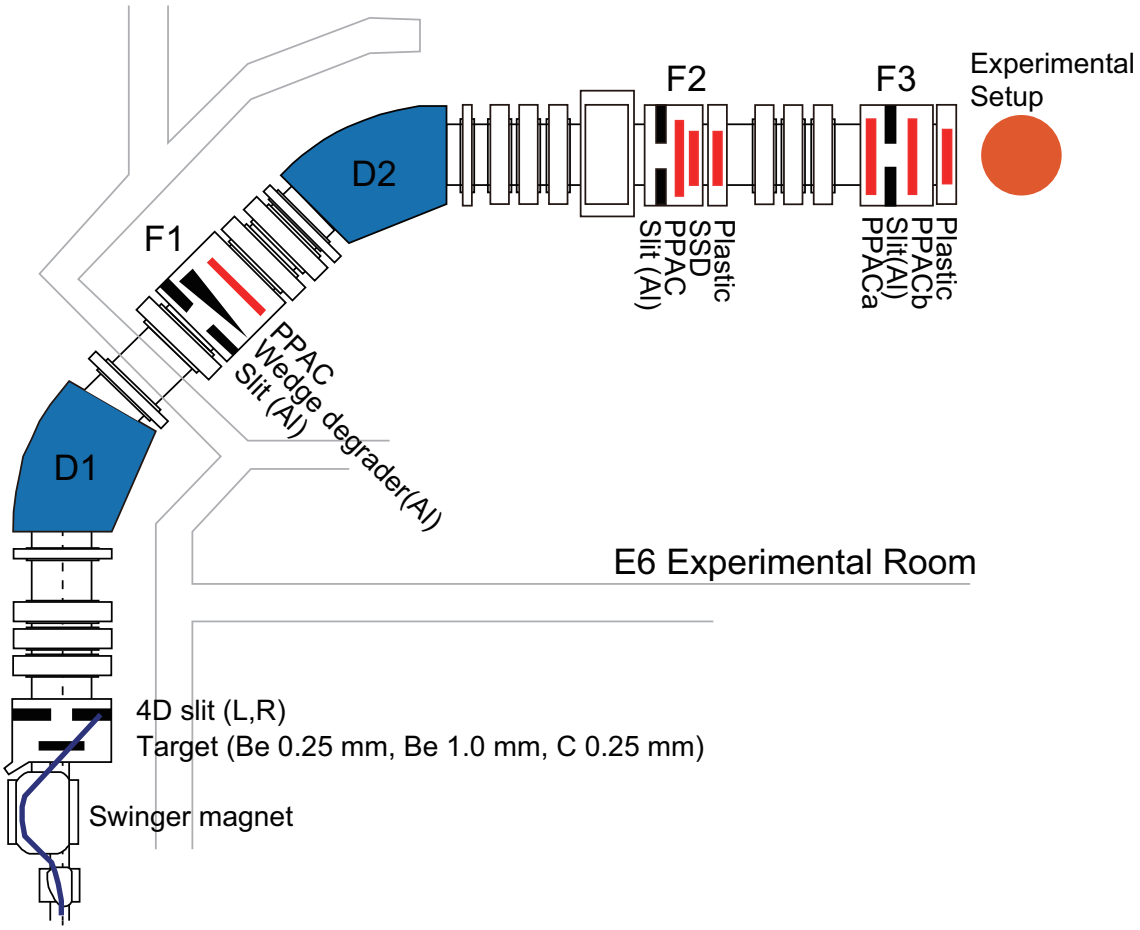

Figure 6.1: Schematic of the setup for production and implantation of spin-polarized fragments using RIPS

where ρ_1 is the radius of curvature of the dipolar electromagnet D1 (3.6 m), and m_{N} and e denote the nucleon mass and elementary electric charge. As a result, the magnetic rigidity $B\rho_1$ is given as follow, and separation with $A = Z$ becomes possible by the dipolar electromagnet D1.

$$B\rho_1 = \frac{A}{Z}\frac{m_{\mathrm{N}}v}{e} = \frac{A}{Z}\frac{p_1}{e} \tag{6.2}$$

Particles other than the set $A = Z$ were removed using the slit of F1. If we have the same $A = Z$ from Eq. 6.2, the trajectory depends on momentum, so D1 is also used to select momentum.

Separation by energy degrader and dipole magnet D2

In the separation by the dipole magnet D1, a nucleus having the same $A = Z$ as the target nucleus and target nucleus is obtained. To select only target nuclei from these, pass through the energy degrader placed on the focal plane of Fl. The range R of the particle in the energy degrader is expressed by the following equation.

$$R = k\frac{A}{Z^2}p_1^{\lambda} \tag{6.3}$$

Here, k, p_1 and λ are constants that depend on the material of the degrader, the momentum of the particle per nucleon, and the constant that depend on the energy of the particle. Assuming that the thickness of the degrader is d, the range after passing through the energy degrader is $R - d$; thus, the range can be expressed as follows equation if the momentum is p_2.

$$R - d = k\frac{A}{Z^2}p_2^{\lambda} \tag{6.4}$$

After passing through the energy degrader, the particles are incident on the dipolar electromagnet D2 and the magnetic rigidity $B\rho_2$ thereof is calculated from these equations:

$$B\rho_2 = B\rho_1 \left(1 - \frac{d}{k}\frac{A^{2\lambda-1}}{Z^{2\lambda-2}}(B\rho_1)^{-2\lambda}\right)^{\frac{1}{2\lambda}} \tag{6.5}$$

ρ_2 is the radius of curvature at D2, and its value is 3.6 m as D1. In the region where the energy per nucleon is 100 MeV, when aluminum is used as the material of the energy degrader, since $\lambda = 1.75$, separation is performed at $A^{2.5}/Z^{1.5}$ in the dipole electromagnet D2 and F2.

$$\frac{A^{2.5}}{Z^{1.5}} \propto \left((B\rho_1)^{3.5} - (B\rho_2)^{3.5}\right)/d \tag{6.6}$$

For simplicity, the spread of the momentum with the variance represented by Eq. 2.2 has not been considered; however, as a result, the trajectory spreads even for one nuclide. To converge the spread of this trajectory, the shape of the energy degrader was wedged such that the target nucleus can be focused at the F2 focal plane. Table 6.1 shows the thickness of the aluminum plate as the effective thickness and bending angle of the aluminum plate as the effective angle.

Several slits were installed in this configuration. 1) A slit behind the production target was used to define the emission angle for the projectile fragments. As shown in Fig. 6.2, this slit comprises of two sets of thick Ta plates. The left and right plates determine the acceptance of the emission angle θ_{h} in the reaction plane, and the up and down plates determine the acceptance angle θ_{v} along the reaction normal. A 7-mm displacement of the slit edge from the beam-line axis corresponds to the emission angle of 1°. 2) The slit is located just before the energy degrader (the first focal plane F1 in Fig. 6.1) and is used to select momentum. Opening the slit 24 mm corresponds to 1% momentum. 3) The slit was placed on the second focal plane F2 for nuclide selection.

Particle discrimination at the second focal plane F2 was performed using a semiconductor solid state detector (SSD) and a parallel plate avalanche counter (PPAC) in the F2 chamber, as well as a plastic scintillator in the F2 and F3 chambers to obtain energy loss (ΔE) and flight time (Time of Flight, TOF). It is possible to obtain information about the energy loss of particles passing through the SSD, and there is a relationship of $\Delta E \propto Z^2$. In this experiment, the SSD was used (thickness: 500 μm). TOF is measured from the signal of plastic scintillator in F2, F3 chamber and TOF is proportional to $A = Z$. The thickness of the plastic scintillator used in this experiment was 100 mum. By two-dimensionally plotting ΔE-TOF, it is possible to identify the particles. Figure 6.3 shows the particle identification diagram of ^{21}O of this experiment. The setting of the beam line

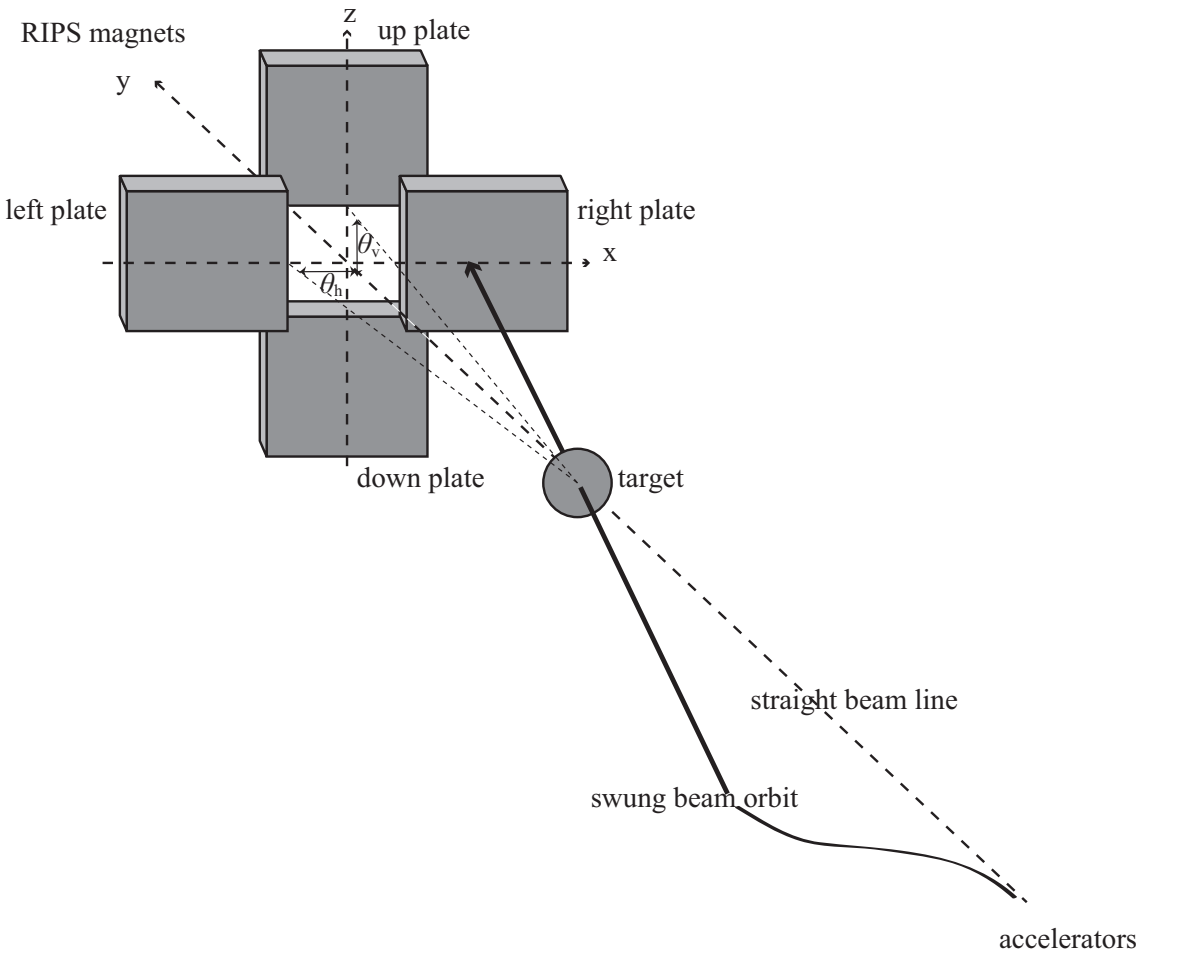

Figure 6.2: Acceptance slit for emission angles of fragments. A primary beam is inclined using a beam swinger. θ_h and θ_v denote acceptance of the emission angle in the reaction plane and along the reaction normal, respectively.

at this time is shown in Table 6.1. Since PPAC is sensitive to position information, it was used to view an image of the beam. Here, the magnetic fields of the dipole electromagnets D1and D2 were adjusted such that the target unstable nuclear beam passed through the center at the focal plane using the PPAC in the F1 and F2 chambers. In addition, PPAC in the F2 chamber, together with the particle identification information, the nuclide whose position is shifted from the target nuclide on the F2 focal plane among the nuclide other than the target nuclide not reaches the final focal plane F3 by adjusting the slit.

Table 6.1: RIPS overview

Configuration	Q-Q-SX-D-SX-Q (first section) Q-Q-SX-D-SX-Q-Q-Q (second section) Q-Q-Q (third section)
Angular acceptance	80 mrad, circle
Solid angle	5 msr
Momentum acceptance	6%, for full angular acceptance
Max. magnetic rigidity	5.76 Tm, 65% larger than that of the cyclotron
Focuses	F1: dispersive, end of the first section F2: double achromatic, end of the second section F3: double achromatic, end of the third section
Flight path length	F0-F1: 10.4 m F0-F2: 21.3 m F0-F3: 27.5 m
Momentum dispersion at F1	(x|δ) = 2.4 cm/%
Magnification at F1	(x|x) = -1.6, (y|y) = -5.7
Magnification at F2	(x|x) = 2.5, (y|y) = 1.5
Beam swinger	Max 15 degree

6.2 Polarization production parameter

6.2.1 Optimal FOM simulation by momentum selection

We simulated change in the experimental efficiency by momentum selection in the nuclear reaction. First, we describe selection of the target thickness. Initially, we optimized the target thickness using the LISE ++ simulation code [40]. The results are shown in Fig. 6.3. Thickness approximately 1.0 mm assuming that the maximum value of yield×0.7 is the maximum thickness, concerned that the target is too thick and depolarized. Therefore, in case of an emphasis on yield, the Be 1.0 mm target is optimal. Next, we describe the momentum distribution. As discussed in Section 2.1, momentum in the case of nuclear fragmentation reaction is given by Eq. 2.3, and in the case of pick-up reaction it is given by Eq. 2.14. The parameters of this experiment were added to these and calculated as follows.

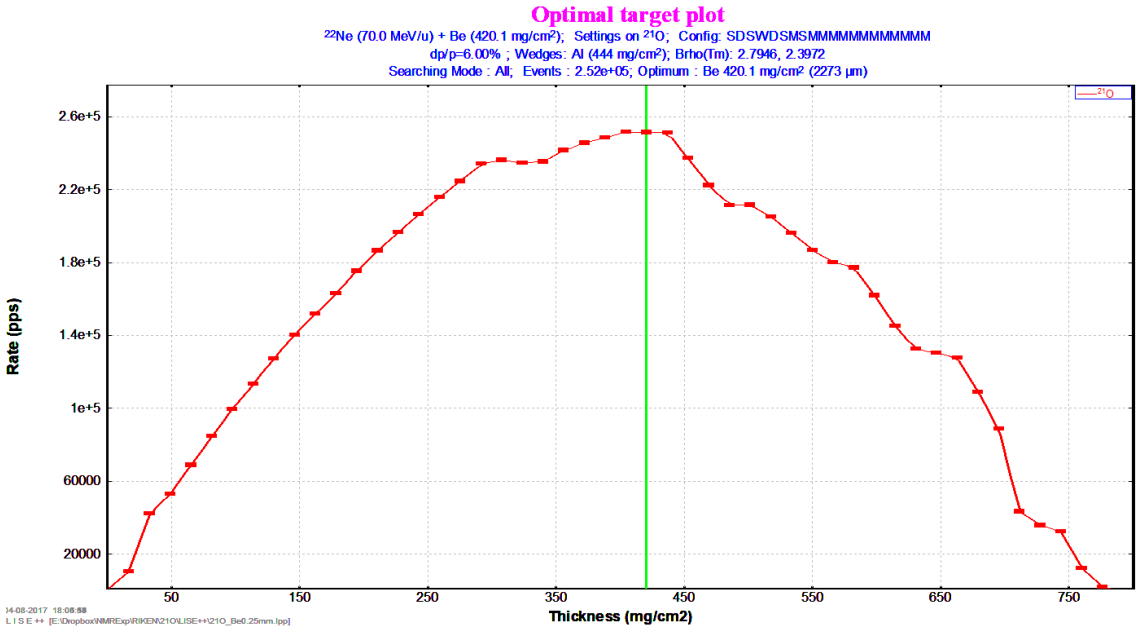

Figure 6.3: Results of optimal target simulation by LISE++

$$\begin{aligned} \sigma_{\mathrm{F}} &= \sigma_0 \sqrt{\frac{K(A-K)}{A-1}} \\ &= 90 \times \sqrt{\frac{21(22-21)}{22-1}} \\ &= 90 \text{ MeV/c} \end{aligned} \tag{6.7}$$

$$\begin{aligned}\sigma_{\mathrm{P}} &= \sigma_0\sqrt{\frac{A_{\mathrm{PF}}(A_{\mathrm{P}}-A_{\mathrm{PF}})}{A_{\mathrm{P}}-1}} \\ &= 90\times\sqrt{\frac{20(22-20)}{22-1}} \\ &= 124\ \mathrm{MeV/c}\end{aligned} \tag{6.8}$$

Momentum p_0 of fragments ^{21}O with speed equal to the incident velocity is given as follows:

$$p_0 = 7.728\times10^3\ \mathrm{MeV/c}. \tag{6.9}$$

Thus, momentum distribution $f(x)$ with $x=(p-p_0)/p_0$ is given as

$$f(x) = \exp\left(-\frac{1}{2}\left(\frac{p_0}{\sigma}\right)^2 x^2\right), \tag{6.10}$$

and the obtained calculation results are shows in Fig. 6.4.

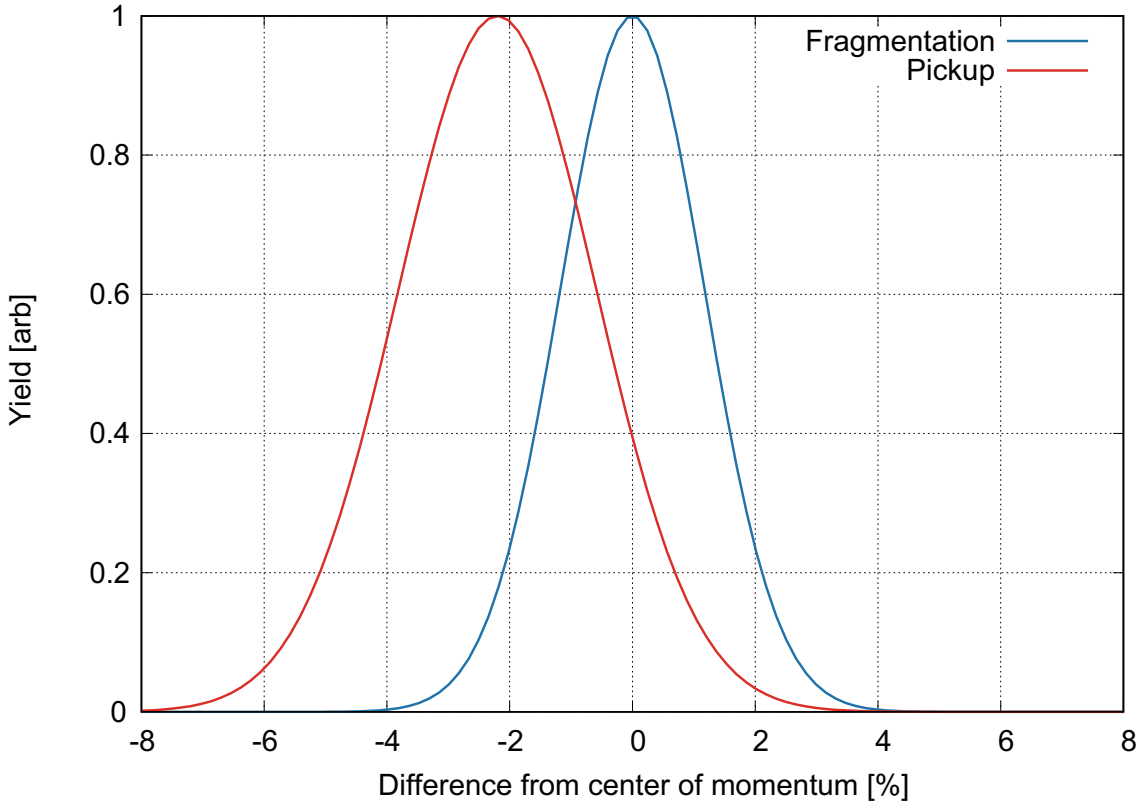

Figure 6.4: Calculation results of momentum distribution of ^{21}O

Next, the degree of polarization of the fragment ^{21}O against the momentum distribution will be considered. The change in polarization degree P relative to the momentum distribution can be expressed by Eqs. 6.11 and 6.12, where $a=0.8$ and $b=1.7$ to reproduce the polarization of reported in the literature [16]. Figure 6.5 shows the calculation result.

$$P_{\mathrm{F}}(x) = -\tanh(ax) \tag{6.11}$$

$$P_{\mathrm{P}}(x) = -\tanh(ax + b) \tag{6.12}$$

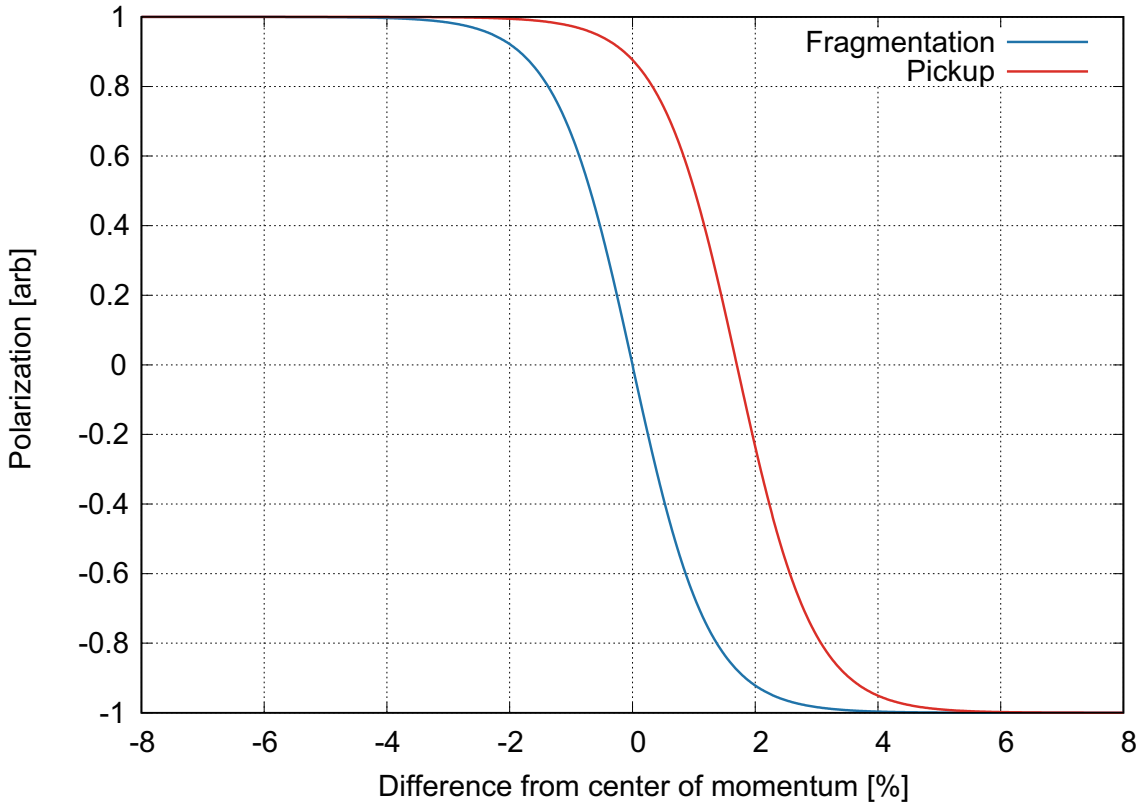

Figure 6.5: Polarization calculation results

Experimental efficiency, FOM is expressed using Yield×Polarization^2. In the case of ^{21}O, it can be expressed by the following expression using the Eqs. 6.10, 6.11 and 6.12.

$$FOM(x) = f(x) \times P(x)^2, \tag{6.13}$$

The results are shown in Fig. 6.6. As can be seen, the momentum area that should be selected for both reactions was found.

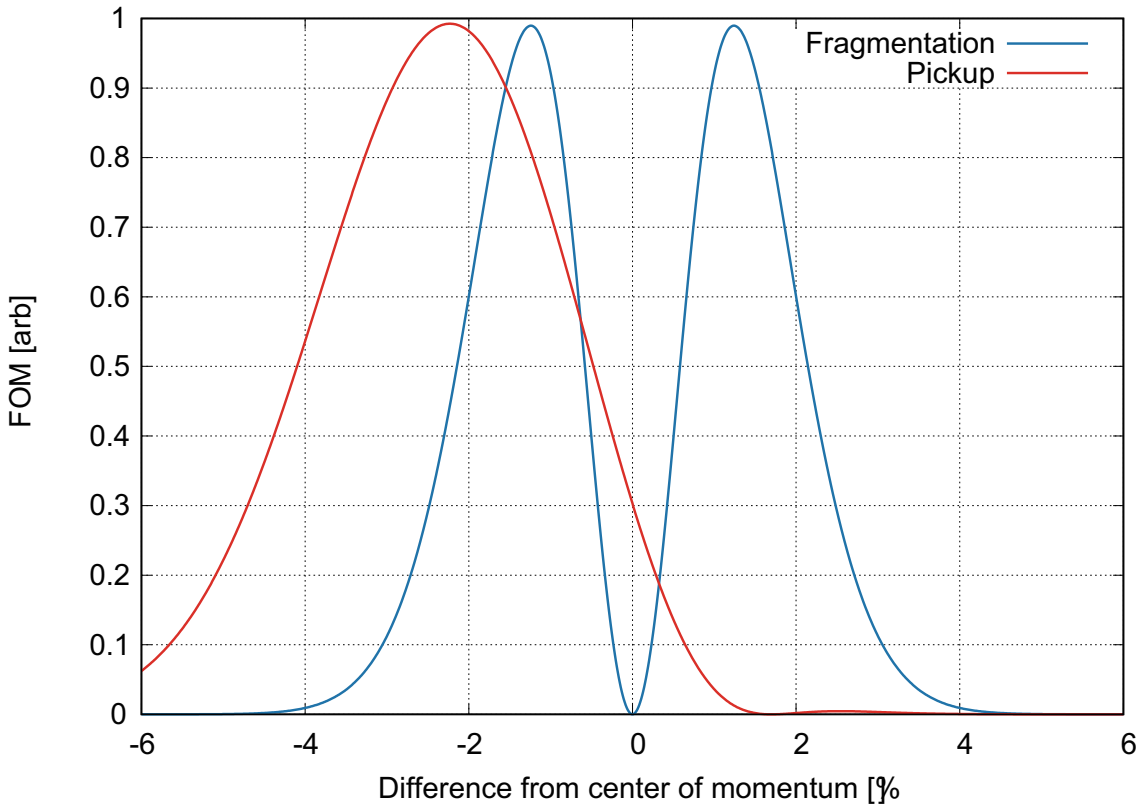

Figure 6.6: Calculation results of FOM

6.2.2 Emission angle

To obtain spin-polarized RI beams, the emission angle should be selected as described in Section 2.1. The slit located downstream of the production target was used to select the emission angle (Fig. 6.2).

The transversal momentum distribution of the outgoing fragments has a Gaussian-like shape with a width known as the perpendicular width $\sigma_\perp$ being function of the Goldhaber width [16]:

$$\sigma_\perp^2 = \sigma_0^2 \frac{A_f(A_p - A_f)}{A_p - 1} + \sigma_d^2 \frac{A_f(A_f - 1)}{A_p(A_p - 1)}, \tag{6.14}$$

where σ_d is orbital dispersion and takes a typical value of 200 MeV/c [17].

The emission angle θ_L is expressed as follows:

$$\theta_\mathrm{L} = \tan^{-1} \frac{\sigma_\perp}{p_0}. \tag{6.15}$$

The emission angle that calculated are $\sigma_\mathrm{L} = 1.69°$. However after AFR measurement, the emission angle was optimized to 2.6°.

The target, angle, and momentum acceptance differed between measurements because the polarization degree was optimized by the AFR measurement. Table 6.2 lists the final RIPS parameters for the β-NMR measurement.

Table 6.2: RIPS parameters

Primary beam	$^{22}Ne^{10+}$
Incident energy	69.18 A MeV
Beam intensity	250 pnA
Target material	^{9}Be
Target thickness	1.81 mg/cm^2
Emission angle(θ_L)	2.6°
Emission angle(θ_h)	2.1° – 6.0°
Emission angle(θ_v)	±1.0°
Momentum region	7.47 GeV/c ±3%
F1 slit	±72 mm
$B\rho_1$	2.9330 Tm
F1 degrader material	Aluminum
F1 degrader thickness	452.8 mg/cm^2
F1 degrader angle	2.21 mrad
$B\rho_2$	2.5813 Tm
F2 slit L	25 mm
F2 slit R	15 mm
Intensity at F2	25 kcps
Purity	88%

6.2.3 Momentum distribution

The momentum distribution measured in this experiment is shown in Fig. 6.7. Here, p_{Beam} is the center of the velocity of the momentum, and p_0 is the velocity of the incident nucleus converted to the momentum of the fragment. In the momentum measurement, while setting the magnetic field of the D1 dipole magnet to 0% at the point corresponding to p_0 and setting the momentum width at $\pm$ 0.5% at the F1 slit, the number of ^{21}O per unit time obtained at that time, the ratio with the recoil counter in the F0 chamber was measured. As shown in Fig. 6.7, the momentum recalculated as $(p_{\mathrm{F}} - p_{\mathrm{Beam}})/p_{\mathrm{Beam}}$. First, the number of ^{21}O was determined using the two-dimensional TOF image measured between the SSD in the F2 chamber and the F2-F3 plastic scintillator, and the purity of ^{21}O contained in the secondary beam was obtained. If the synchronized count of the SSD and plastic scintillator is N_{all} and the count of ^{21}O is $N_{^{21}\mathrm{O}}$, then purity P can be expressed as follows.

$$P = \frac{N_{^{21}\mathrm{O}}}{N_{\mathrm{all}}} \tag{6.16}$$

Next, the count of the F2 plastic scintillator was standardized by the count of the recoil counter per unit time, and the number of ^{21}O was obtained by multiplying the standardized count by the purity P. If the count per unit time of the F2 plastic scintillator is N_{PL} and the count of the recoil counter is N_{r}, the count $Y_{^{21}\mathrm{O}}$ of ^{21}O can be expressed as follows:

$$Y_{^{21}\mathrm{O}} = \frac{N_{\mathrm{PL}}}{N_{\mathrm{r}}} \times P \tag{6.17}$$

The vertical axis of Fig. 6.7 is $Y_{^{21}\mathrm{O}}$.

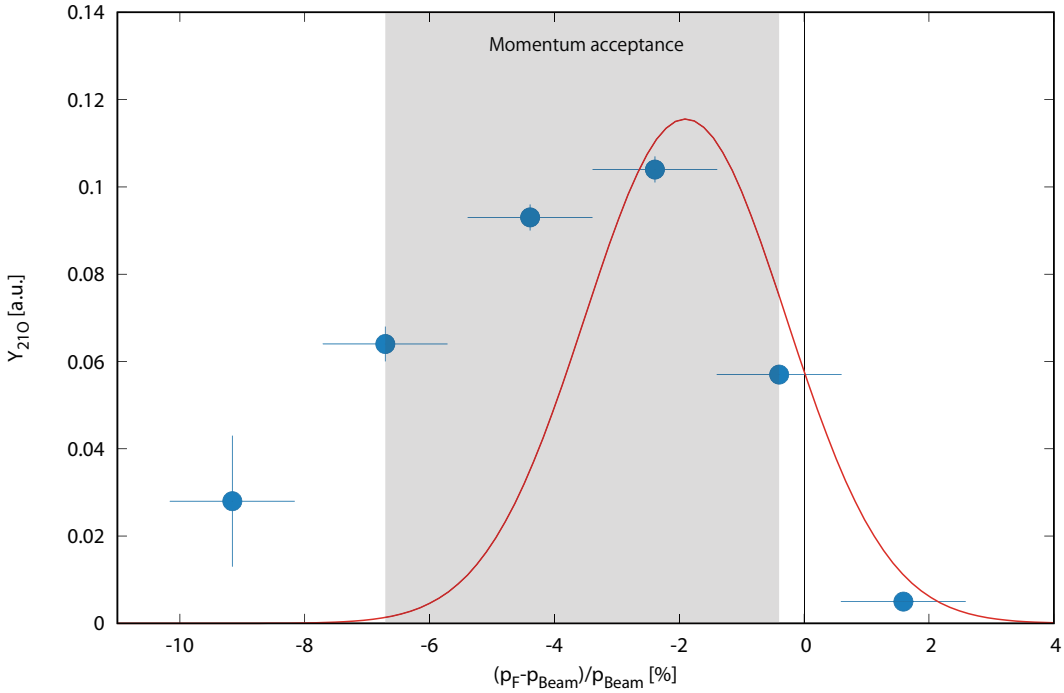

Figure 6.7: Momentum distribution of ^{21}O. The circles are experimental data and the red line is the calculation result by the Eq. 6.10. The momentum area selected by NMR measurement was shown in gray area.

6.3 Polarization measurement using the new AFR system

A schematic of the AFR apparatus is shown in Fig. 6.8. The unstable nuclear beam that passed the F3 chamber degraded the energy with the energy degrader, then the beam diameter was narrowed with the collimator and stopped in the stopper crystal at the center of the static magnetic field. Note that the thickness of the energy degrader can be changed continuously by rotation, the stop position of the beam is confirmed by beam counters installed upstream and downstream of the stopper, and the unstable nuclear beam stops at the center position of the stopper. Here, the Al plate was set to 0.25 mm for the ^{21} O measurement. β rays emitted upward and downward from the unstable nuclei stopped at the stopper were detected using plastic scintillators. As shown in Fig. 6.8, two plastic scintillators (thickness: 0.5 mm) were installed above and below the stopper. Two plastic scintillators were used at the top and bottom to eliminate the background due to γ rays from daughter nuclei or the like by synchronizing the two signals. This is possible because the detection efficiency of γ rays is less than that of β rays.

The stopper was tilted to not interfere with the β rays coming up and down. Considering only the energy loss of β rays, the stopper should be tilted as much as possible; however, the length of the stopper in the beam axis direction becomes long with increasing tilt. Therefore, since the size of the rotating magnet in the AFR also becomes large, the torque required to rotate the rotating magnet also becomes large, and a strong motor is required. In addition, as the length in the beam axis direction increases, the time required for the unstable nuclear beam to pass through the stopper increases and the energy generally attenuates much more than in atmosphere. We installed 45° such that the thickness passing through the β-ray relative to the center of the stopper and the thickness through which the unstable nuclear beam passed through the stopper were equal.

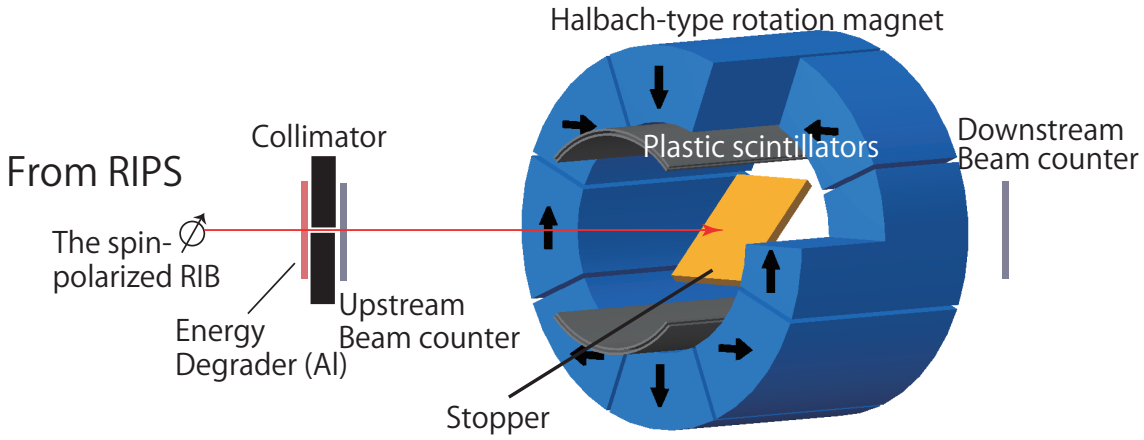

Figure 6.8: Schematic of AFR apparatus

6.4 Magnetic moment measurement using new β-NMR system

A schematic of the β-NMR apparatus is shown in Fig. 6.9. Similar to the AFR device described in Section 5.3, the unstable nuclear beam that passed through the F3 chamber was energy degraded by the energy degrader installed downstream of the F3 chamber, and the beam diameter was reduced by passing it through a collimator with a diameter of 18 mm. The beam stops at the center of the stopper crystal at the center between the poles of the dipole magnet. Here, the dipole magnet had a pole gap of 70 mm and a static magnetic field of 500.94(16) mT was obtained by applying DC current (20.986(1) A) to the electromagnet in constant current mode. The fluctuation of the magnetic field at this time is due to the fluctuation of the current. β-rays emitted from the stopped unstable nucleus are detected by β ray detectors, which are three on each of the up and down sides. The scintillator part of the β ray detector used is a circle with a diameter of 100 mm, 120 mm, and 145 mm in order from the innermost scintillator. The thickness is 2 mm, and the thicknesses of the light guide and light shielding film wound on the scintillator were also adjusted. The total thickness was approximately 5 mm per sheet. An H1161 (Hamamatsu Photonics) was used as the photomultiplier. The voltage is -2700 V. The solid angle Ω of the upper counter is expresses as follows, where θ_0 is the angle from the center of the magnet to the edge of the outermost scintillator.

$$\Omega = 2\pi(1 - cos\theta_0) \tag{6.18}$$

With a scintillator size of $\theta_0 = 64.2°$, the upper solid angle is 1.1π. Since the shape of the detector is vertically symmetrical, it is sufficient to consider only the upper side, and the detection efficiency $\epsilon\Omega$ by the solid angle is given as

$$\epsilon\Omega = \frac{2\pi(1 - cos\theta_0)}{2\pi} = 0.56. \tag{6.19}$$

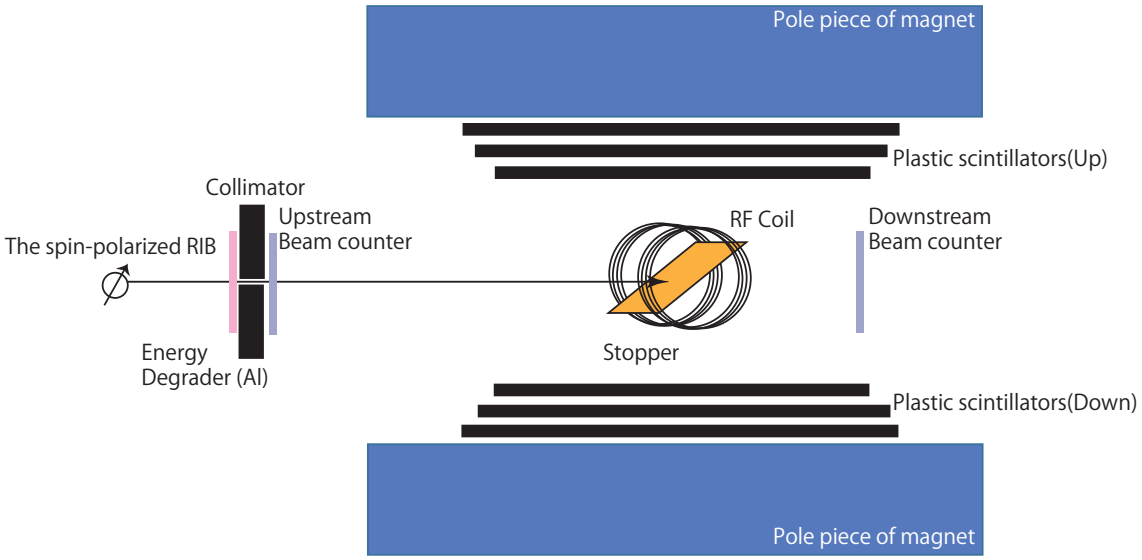

Figure 6.9: Schematic of β-NMR apparatus

6.5 Data acquisition system

In the AFR (β-NMR) experiment, β rays are detected by two (three) plastic scintillators of each measuring device. The detection signal is divided into two using a signal divider. Here one signal detects the β ray energy information as an analog signal, and the other signal is converted to a digital signal and sent to a data processing system. The start signal (event trigger) of the data processing system is expressed as follows.

$$\begin{aligned} \text{event trigger} &= (((\mathrm{U1} \cap \mathrm{U2}) \cup (\mathrm{D1} \cap \mathrm{D2})) \cap \text{count gate}) \text{ for AFR} && (6.20) \\ &= (((\mathrm{U1} \cap \mathrm{U2} \cap \mathrm{U3}) \cup (\mathrm{D1} \cap \mathrm{D2} \cap \mathrm{D3})) \cap \text{count gate}) \text{ for } \beta - \mathrm{NMR} && (6.21) \end{aligned}$$

The U1, U2, and U3 detectors were installed on the upper side of the stopper, and the D1, D2, and D3 detectors were installed on the lower side of the stopper. With the occurrence of this event trigger, the event capture gate of the CAMAC module opens, and the analog digital converter (ADC), the coincidence register, and the non-stop time to digital converter (NSTDC) record the information. The circuit diagram is shown in Figs. D.1–D.3. Here, a 4300B fast enhancement and readout ADC (FERA) manufactured by LeCroy was used as ADC. In addition, a CC7700 (Toyo Technica Co.) was used as the crate controller. The analog signal is divided into two, where one signal is converted into a digital signal and used as time information of the event. The other signal is used to synchronize the analog signal with the gate with a certain time window created by the digital signal and obtain energy information by integrating the charge that has entered the time gate. The energy information of β rays obtained by FERA, time information, such as the collapse of nuclei by NSTDC, β ray detection information, and control information from PSG were recorded by the coincidence register. The event trigger information is transferred to the PC for data processing, i.e., online analysis processing. Since event detection is prohibited until data processing is completed, a veto signal is applied when an event is detected. When data processing is complete, a veto release signal is output from the output register and the next event trigger is accepted.

Chapter 7

Data analysis and experimental results

In this chapter, we first report the analysis of the ^{21}O beams produced by projectile-fragmentation and pick-up reaction. Then, we determined the best condition of polarization from AFR measurement. Finally, we measured Lamor frequency of ^{21}O.

7.1 Particle identification

The polarized beam of ^{21}O was produced by the projectile fragmentation reaction and nucleon pick-up reaction of ^{22}Ne beam at $E/A = 70$ MeV. The isotope separation was provided by combined analyses of the magnetic rigidity and momentum loss of the ions in the aluminum degrader at F1 of RIPS. To identify ^{21}O from the other isotopes, we measured the time of flight (TOF) of the beam and energy loss (ΔE) in the Si detector located F2.

The ΔE-TOF spectrum of ^{21}O with the 0.25-mm thick Be target is shown in Fig. 7.1. The vertical axis stands for the ΔE and horizontal one stands for the TOF. The position distribution of the ^{21}O at the achromatic focal plane F2 of RIPS was measured by a parallel plate avalanche counter (PPAC) installed at F2. The position was optimized by adjusting the magnetic field in the D2 magnet. The ΔE spectrum of ^{21}O with 0.25 mm thickness Be target is shown in Fig. 7.2. As shown in Figs. 7.1 and 7.2, two components that correspond to ^{21}O and ^{19}N were observed with the F2 slit $L = 25$ mm and $R = 15$ mm. From the spectrum the purity of the ^{21}O beam was measured to be about 88% at F2. The ΔE-TOF and ΔE spectrum of ^{21}O with 1.0 mm thickness Be target is shown in Figs. 7.3 and 7.4.

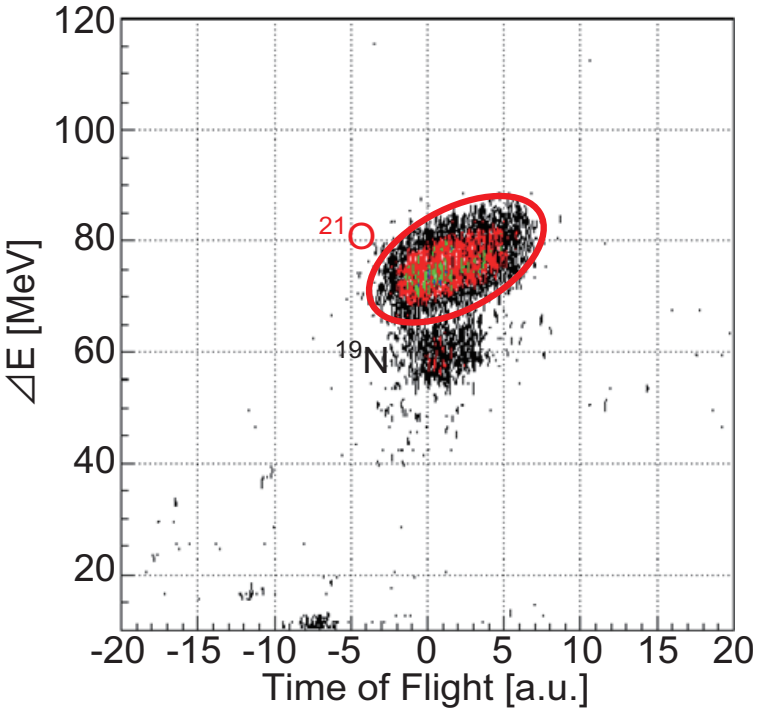

Figure 7.1: Particle identification graph of ^{21}O with 0.25-mm^{t} Be target

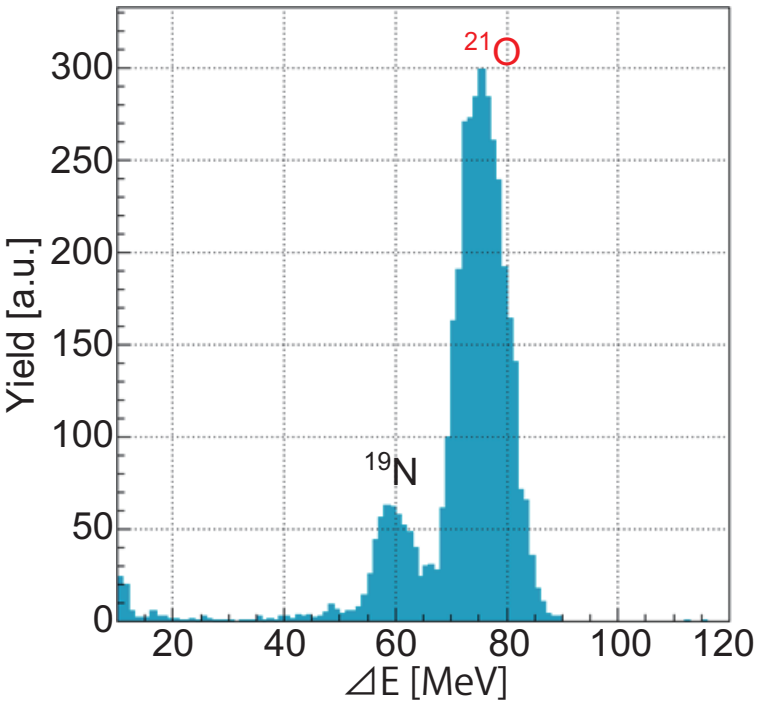

Figure 7.2: Energy loss of ^{21}O with 0.25-mm^{t} Be target

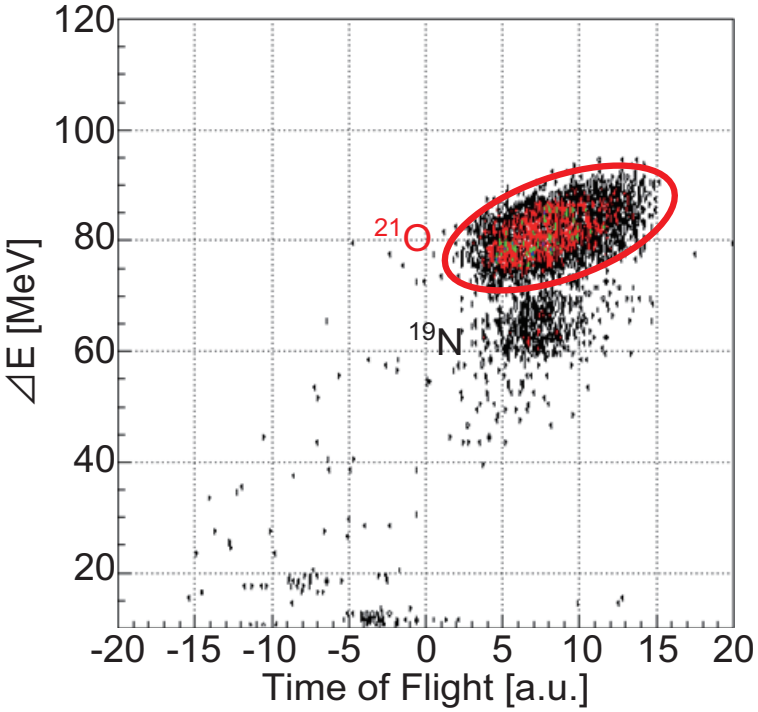

Figure 7.3: Particle identification graph of ^{21}O with 1.0-mm^{t} Be target

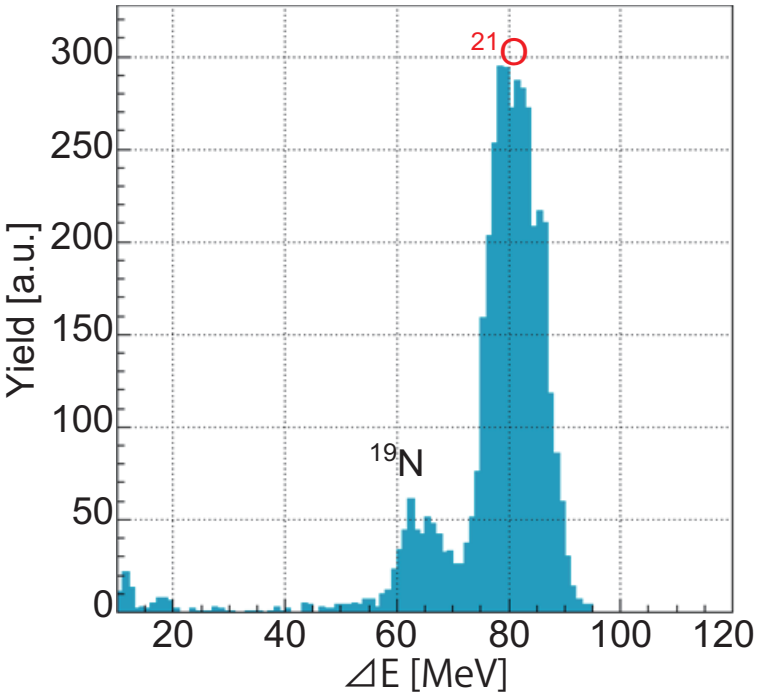

Figure 7.4: Energy loss of ^{21}O with 1.0-mm^{t} Be target

7.2 Time spectrum for the β decays ^{21}O

To confirm whether the nuclei selected by particle identification are really ^{21}O, time spectrum of β decay was obtained. The measurement result is shown in Fig. 7.5, where circles represent experimental data and curves are fitting curve obtained using the following expression.

$$f(t) = N_{^{21}\mathrm{O}} \exp\left(-\frac{\ln 2 \cdot t}{T_{1/2}(^{21}\mathrm{O})}\right) + N_{^{21}\mathrm{F}} \exp\left(-\frac{\ln 2 \cdot t}{T_{1/2}(^{21}\mathrm{F})}\right) \tag{7.1}$$

where $N_{^{21}\mathrm{O}} and N_{^{21}\mathrm{F}}$ are free parameters, that represent the yield of nuclei. $T_{1/2}(^{21}\mathrm{O})$ and $T_{1/2}(^{21}\mathrm{F})$ are fixed parameters that represent the half-life of nuclei. These fitting results are given in Table 7.1

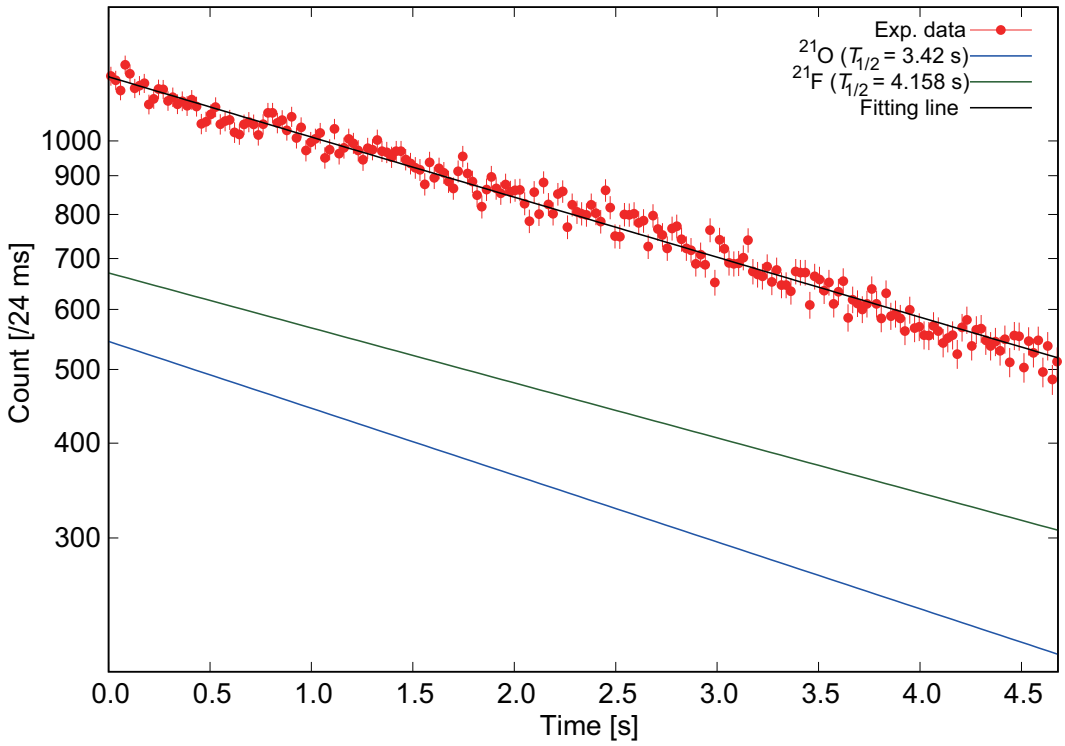

Figure 7.5: Time spectrum of ^{21}O

Table 7.1: Least square fitting results for time spectrum of ^{21}O

$N_{^{21}\mathrm{O}}$	544(63)
$T_{1/2}(^{21}\mathrm{O})$	3.42 s
$N_{^{21}\mathrm{F}}$	670(58)
$T_{1/2}(^{21}\mathrm{F})$	4.158 s
χ^2	0.918

The half-life of ^{21}O measured this time is 3.42 s, but it is difficult to perfectly separate it because

its half-life of the daughter nucleus ^{21}F is close to 4.158 s. As a result, it is understood that ^{21}O was obtained with a purity of 43(6)%.

7.3 AFR measurement

AFR measurements were taken to identify optimal polarization conditions. The changed conditions are summarized as follows.

7.3.1 Selection of stopper materials

MgO crystal was used as the stopper material for the magnetic moment measurement of ^{13}O [41] and CaO crystal was used for ^{19}O [42]. The measurement results for each sample are given in Table 7.2. As can be seen, polarization could not be observed in the MgO crystal. One possible reason for this is that the spin-lattice relaxation time T_1 of ^{21}O is less than the counting time. According to the literature [41], the relaxation time of ^{13}O in the MgO crystal is $T_1 > 50$ ms. The half-life of ^{21}O ($T_{1/2} = 3.42$ s) is two orders of magnitude greater than the lower limit value of T_1 of ^{13}O. In the measurement sequence, since beam on/off was switched on the order of seconds; thus it is possible polarization could not be preserved until the end of the counting time. In contrast, polarization was observed in the CaO crystal; however, the degree of polarization was small, because the other polarization conditions were not good.

Table 7.2: β ray yield and $A_\beta P$ values obtained with CaO and MgO crystals

	MgO	CaO
Y_β [cps]	128 ± 11	100 ± 10
$A_\beta P$ [%]	0.08 ± 0.31	0.27 ± 0.18
FOM [a.u]	0.9 ± 4.7	7.2 ± 7.0

7.3.2 Selection of measurement sequence

For the measurement sequence, the length of one loop was set to 10 s, which is approximately twice the mean life of ^{21}O, and measurement was conducted with two types of beam on/off period of "5 s – 5 s" and "2 s – 8 s". This is a comparison in which the polarization is relaxed prior to starting the measurement after beam implantation, and the polarization degree was reduced as the polarization relaxation time was not so long. The results are shown in Fig. 7.6. As can be seen, polarization relaxation time was not so long, and when the beam on was set to 5 s, the degree of polarization was reduced. Therefore, the "2 s – 8 s" sequence represent the better condition.

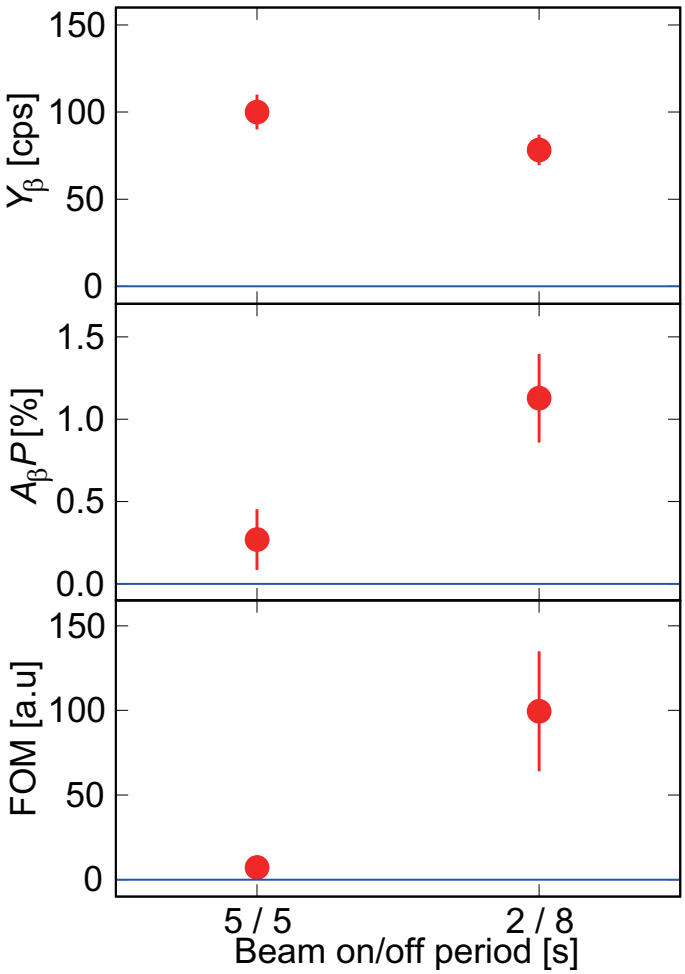

Figure 7.6: AFR measurement results (selection of measurement sequence)

7.3.3 Selection of target thickness

As the target, Be 0.25 mm^t and 1.0 mm^t were prepared. Figure 7.7 shows the results of FOM on two targets, i.e., a thin target (0.25 mm^t) emphasizing polarization, and a thick target (1.0 mm^t) with an emphasis on yield. We were apprehensive about depolarization in the thick target; however, the results demonstrate that the thick target was better than the thin target because the β-ray yield increased.

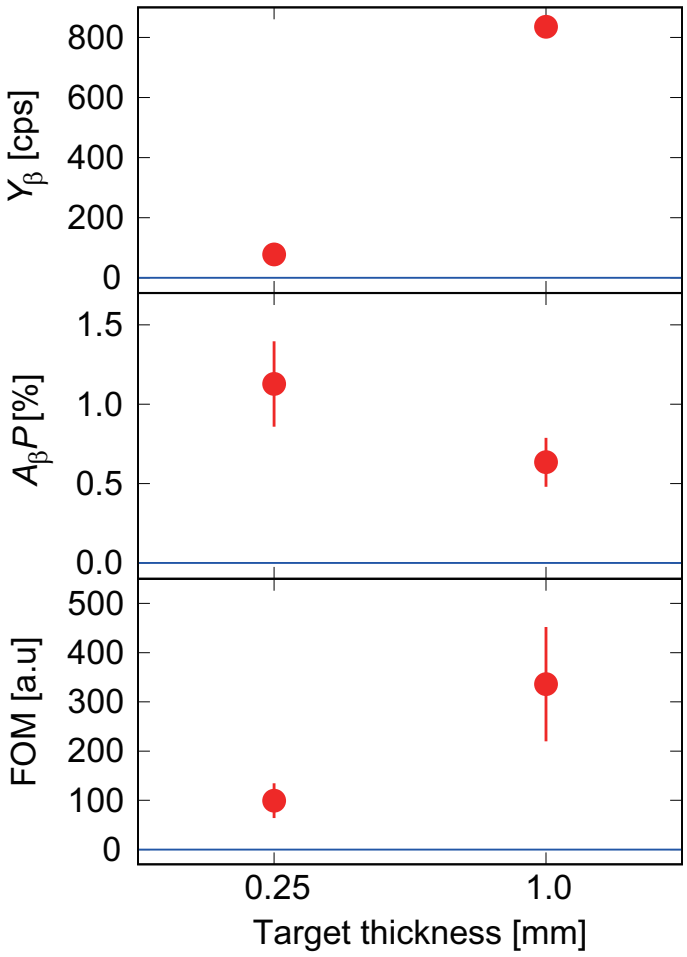

Figure 7.7: AFR measurement results (selection of target thickness)

7.3.4 Selection of emission angle

For the angle selection, measurements were taken with acceptance changed with the incident angle unchanged. The measurement results are shown in Fig. 7.8. It was found that the FOM is better when the angle is tightened; thus, we decided to select the angle from 2.1 to 6.0 degree.

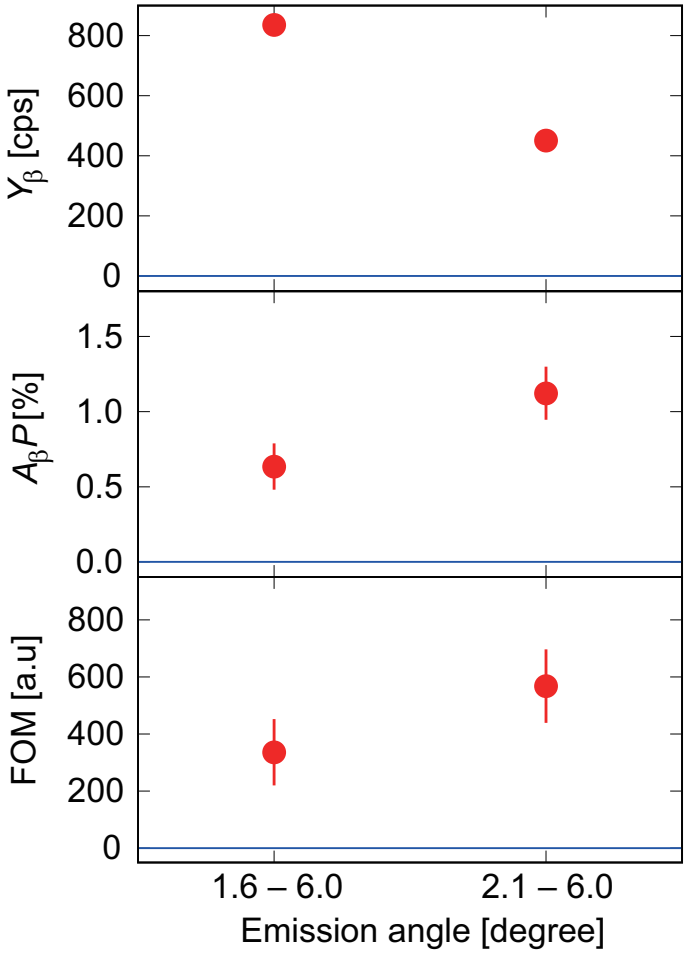

Figure 7.8: AFR measurement results (selection of emission angle)

In summary, the following condition is optimal in the current polarization measurement.

Table 7.3: Optimum conditions obtained from AFR measurement

Stopper material	CaO crystal
Measurement sequence	2 s + 8 s
Target thickness	1.0 mm^t
Selected angle	2.1–6.0 degree

7.3.5 Nuclear polarization

Polarization of $|A_\beta P| = 1.12 \pm 0.18\%$ was obtained from an AFR measurement of ^{21}O. Here, we make some corrections to derive the degree of polarization.

Correction using asymmetry parameter

The asymmetry parameter A_β represents the degree of asymmetry of the probability of emission parallel or anti-parallel to β rays spin.

In the case of Fermi transition, A_β is zero. For pure Gamow-Teller transition, A_β is expressed as follows:

$$A_\beta = \begin{cases} \pm 1 & \text{for } I \to I-1 \\ \pm \dfrac{1}{I+1} & \text{for } I \to I \\ \mp \dfrac{I}{I+1} & \text{for } I \to I+1 \end{cases} \tag{7.2}$$

where up is selected if the sign is β^+ decay and down is selected if the sign is β^- decay.

Figure 7.9 shows decay scheme of ^{21}O [27]. Although the spin of the ground state of ^{21}O is not determined in this figure, it is determined that I^π is $5/2^+$ from this study; thus, the following is calculated as $I^\pi = 5/2^+$. Moreover, spins of several excitation levels of ^{21}F, which is the daughter

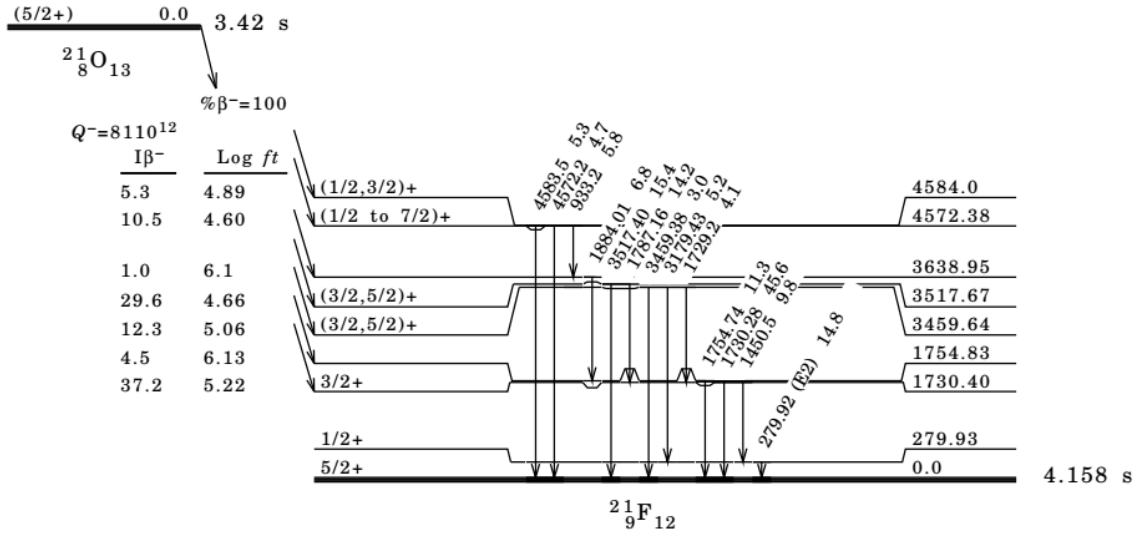

Figure 7.9: Decay scheme of ^{21}O

nucleus of ^{21}O have not been determined. Therefore, asymmetry parameters were calculated with all spin combinations. The results are shown in Table 7.4.

The upper and lower limit values of the asymmetry parameter were obtained as follows.

$$\begin{aligned} A_{\beta\_\text{upper limit}} &= 0.372 \times (-1) + 0.123 \times (-\frac{2}{7}) + 0.296 \times (-\frac{2}{7}) + 0.105 \times (\frac{5}{7}) + 0.053 \times (-1) \\ &= -0.472 \end{aligned}$$

Table 7.4: Branching ratio and asymmetry parameter

Ex [keV]	Branching ratio	Spin exchange	Asymmetry parameter
1730.40	37.2%	$\frac{5}{2}^+ \rightarrow \frac{3}{2}^+$	-1
3459.64	12.3%	$\frac{5}{2}^+ \rightarrow \frac{5}{2}^+$	$-\frac{2}{7}$
		$\frac{5}{2}^+ \rightarrow \frac{3}{2}^+$	-1
3517.67	29.6%	$\frac{5}{2}^+ \rightarrow \frac{5}{2}^+$	$-\frac{2}{7}$
		$\frac{5}{2}^+ \rightarrow \frac{3}{2}^+$	-1
4572.38	10.5%	$\frac{5}{2}^+ \rightarrow \frac{7}{2}^+$	$\frac{5}{7}$
		$\frac{5}{2}^+ \rightarrow \frac{5}{2}^+$	$-\frac{2}{7}$
		$\frac{5}{2}^+ \rightarrow \frac{3}{2}^+$	-1
4584.0	5.3%	$\frac{5}{2}^+ \rightarrow \frac{3}{2}^+$	-1

$$\begin{aligned} A_{\beta\_\text{lower limit}} &= 0.372 \times (-1) + 0.123 \times (-1) + 0.296 \times (-1) + 0.105 \times (-1) + 0.053 \times (-1) \\ &= -0.949 \end{aligned}$$

Table 7.5 shows the value of the polarization degree corrected using the asymmetry parameter.

Table 7.5: Correction using asymmetry parameter

	$A_\beta P_{\text{exp}}$	A_β	P_{exp}
Upper limit	1.12±0.18	-0.472	-2.37±0.38
Lower limit	1.12±0.18	-0.949	-1.18±0.19

Correction using solid angle of detectors

When the unstable nuclei generated in the stopper β decay, β-rays are released at a certain emission angle distribution. Although the emission angle distribution $W(\theta)$ described in Chapter 2 is only calculated when θ is 0 and 180 degrees, in practice the size of the detector is finite, and the observed $A_\beta P$ diminishes. Therefore, it is necessary to correct the solid angle of the detector. From Section 6.4, the detection efficiency $\epsilon\Omega$ by the solid angle is expressed as follows:

$$\epsilon\Omega = \frac{2\pi(1 - cos\theta_0)}{2\pi} = 0.56. \tag{7.3}$$

Table 7.6: Correction using solid angle of detectors

	P_{exp}	$\epsilon\Omega$	P
Lower limit	-1.18±0.19	0.56	-2.11±0.34

Correction using purity

From the result of the lifetime measurement (Section 7.2), the purity of the ^{21}O nucleus was obtained. Since 100% purity cannot be obtained, corrections based on purity are required.

Table 7.7: Correction using solid angle of detectors

	P_{exp}	Purity	P
Lower limit	-2.11±0.34	0.43±0.06	-4.9±1.0

From the above correction, the polarization degree of ^{21}O obtained in this experiment was $|P| >$ 4.9%.

7.4 β-NMR measurement

In this NMR measurement, since the polarization degree was optimized, the approximate value of the polarization degree was known. First, we measured in wide search mode. As described in Section 3.1, in this mode, a wide range frequency search can be performed by switching multiple capacitors with a relay switch. Here, by switching between three variable capacitors and two ceramic capacitors, the range $g = 0.5765 \pm 0.064$ was searched in a single measurement. Table 7.8 shows the relationship between applied frequency and g-factor. The results of the wide search measurement are shown in Fig. 7.10. The $A_\beta P$ value $(0.63 \pm 0.15)\%$ obtained by the wide search measurement was smaller than that measured by AFR ($A_\beta P = (1.1 \pm 0.2)\%$), but a resonance with a statistical accuracy of 4.2σ was observed. Therefore, we determined that there was a resonance frequency in this region, and it shifted to sequential measurement.

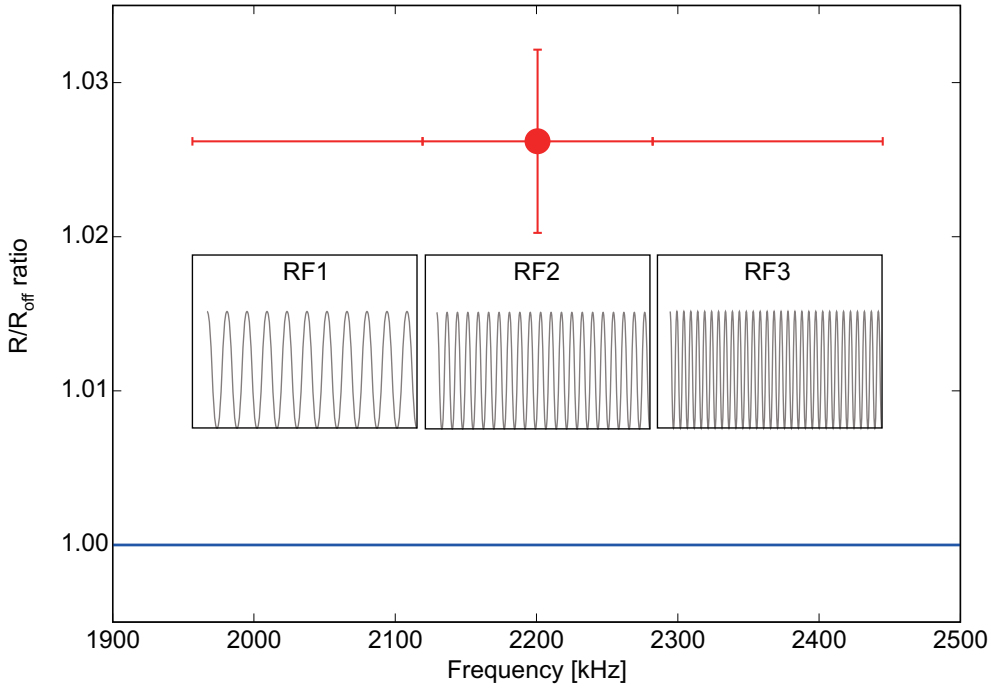

Figure 7.10: Results of wide search mode NMR measurement (the wavy lines are an example of frequency.)

Table 7.8: Relationship between applied frequency and g-factor

RF #	frequency (kHz)	g-factor
1	1956.46–2037.89–2119.32	0.5125–0.5338–0.5552
2	2119.32–2200.75–2282.17	0.5552–0.5765–0.5978
3	2282.17–2363.60–2445.03	0.5978–0.6192–0.6405

In the sequential mode measurement, the wide search range was first divided into three to accommodate a three-point. Here, the FM width was 147.94 kHz. Table 7.9 shows the relationship between applied frequency and g-factor, and the results are shown in Fig. 7.11. As described in section 2.2.3, the frequency sweep was performed in a trapezoidal shape. In this measurement, the effective frequency did not overlap the neighboring region.

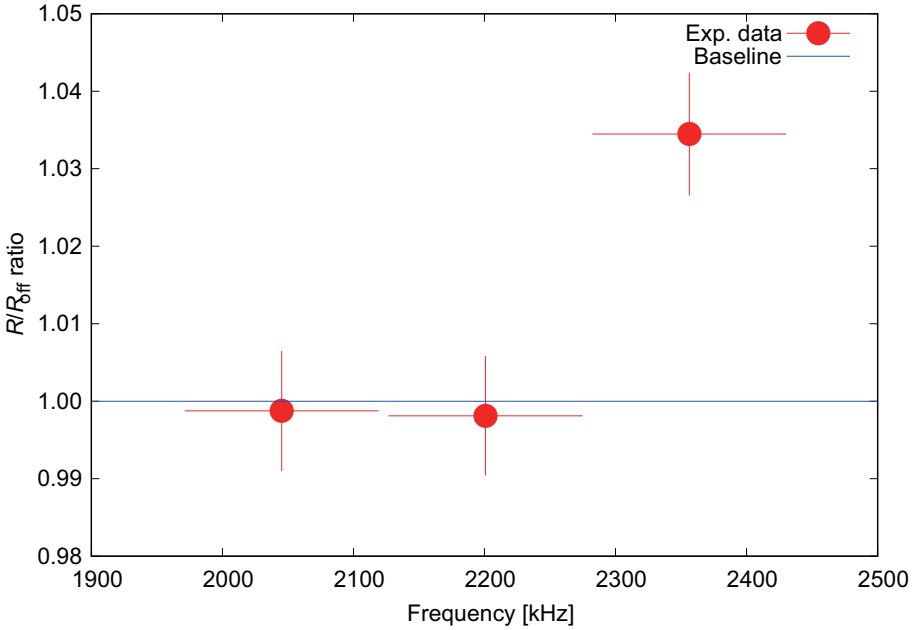

Figure 7.11: Results of three-point sequential mode measurement (FM = 147.94 kHz)

Table 7.9: Relationship between applied frequency and g-factor for sequential measurement

RF #	frequency (kHz)	g-factor
1	1971.26–2045.23–2119.20	0.5164–0.5358–0.5552
2	2126.78–2200.75–2274.72	0.5571–0.5765–0.5959
3	2282.30–2356.27–2430.24	0.5978–0.6172–0.6366

The $A_\beta P$ value obtained in this measurement was 0.86 $\pm$ 0.19%, which is consistent with the AFR $A_\beta P$ value (1.12 $\pm$ 0.18%); thus, the AFP-NMR measurement was successful. Since resonance was observed in the high frequency region, it was possible resonance could be observed in a higher region. However, we swept an FM width of approximately 4% in one region, and there was a resonance frequency in this region. Therefore, this region was divided for further measurement.

Figure 7.12 shows the results of all sequential mode measurements; (a) first three-point measurement; (b) seven-point measurement with FM = 29.16 kHz; and (c) second three-point measurement with FM = 11.65 kHz. Figure 7.12(a) shows only the point to the right of Fig. 7.11. Here, it is necessary to obtain the resonance frequency in order to derive the magnetic moment.

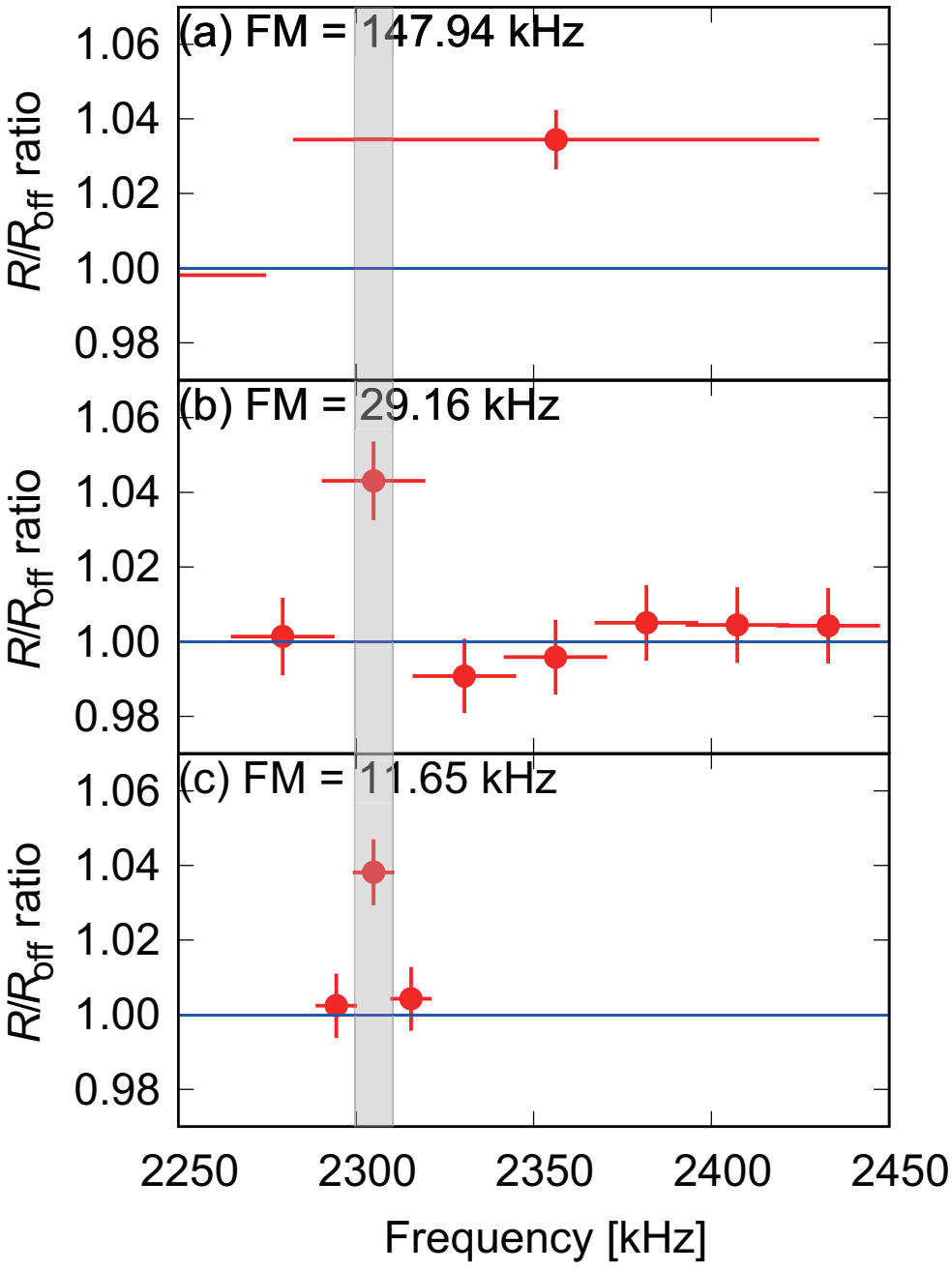

Figure 7.12: Final results of AFP-NMR measurement of ^{21}O: (a) first three-point measurement (high-frequency region only); (b) seven-point measurement with FM = 29.16 kHz; and (c) second three-point measurement with FM = 11.65 kHz. In the figure, gray zone shows the region of final resonance frequency error.

Figure 7.13 shows results of final measurement of ^{21}O again. Since resonance was observed only at one point at three points in Fig. 7.13, half of the overlap of frequency sweep was adopted as a frequency error. The resonance frequency was obtained as follows:

$$\nu_{\mathrm{L}} = 2304.94 \pm 5.35\mathrm{kHz}.$$

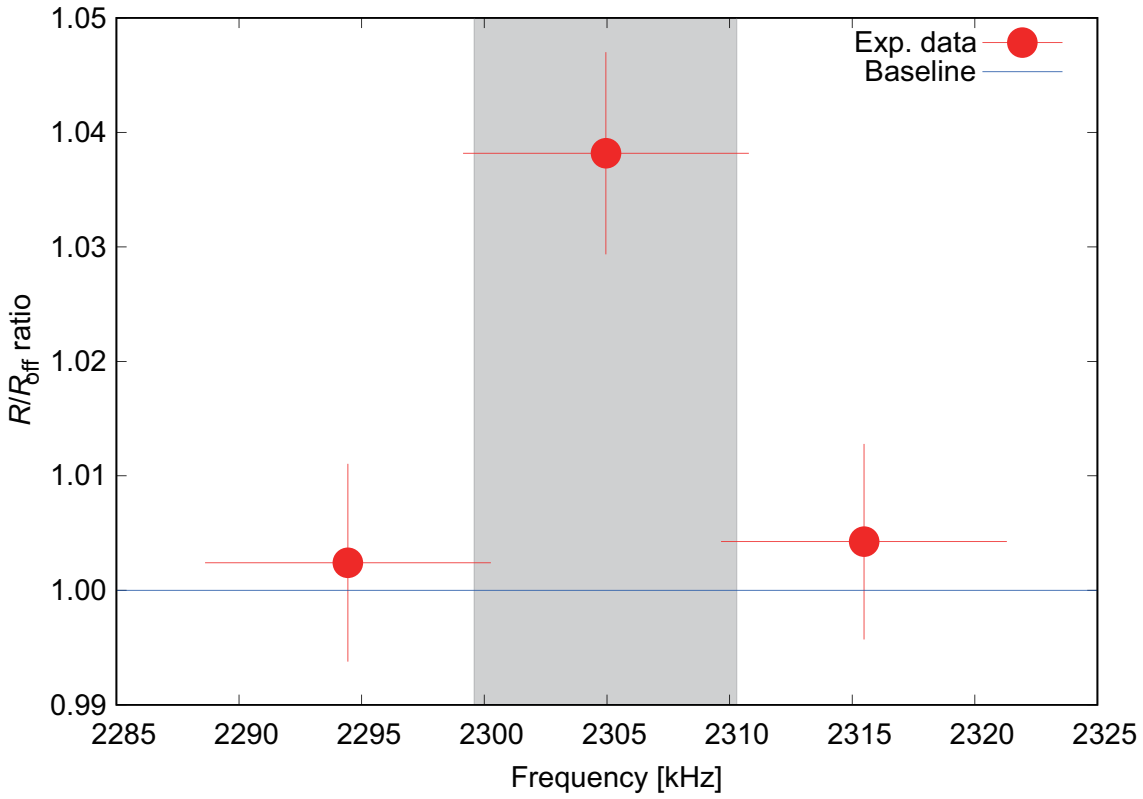

Figure 7.13: Final results of AFP-NMR measurement of ^{21}O. In the figure, gray zone shows the region of final resonance frequency error.

Chapter 8

Discussion

8.1 Results of g-factor

The values of the center frequency was determined from Section 7.4 as follows.

$$\nu_{\mathrm{L}} = 2304.94 \pm 5.35 \text{ kHz}$$

The static magnetic field was measured six times using NMR probe before and after NMR measurement. Table 8.1 shows the values of the magnetic field obtained. By taking a weighted average of these values, the static magnetic field value obtained as follows.

$$B_0 = 500.98 \pm 0.16 \text{ mT}$$

Table 8.1: Obtained values of static magnetic field. The values from 1 to 4 are the measured value before NMR measurement, and 5 and 6 are the values after NMR measurement.

Number	B_0 [G]
1	500.86 ± 0.01
2	500.86 ± 0.01
3	500.85 ± 0.01
4	500.78 ± 0.01
5	501.09 ± 0.01
6	501.43 ± 0.01

Therefore, using the static magnetic field of $B_0 = 500.98 \pm 0.16$ mT, the value of g-factor could be obtained as follows.

$$\begin{aligned} |g| &= \frac{h\nu_{\mathrm{L}}}{\mu_{\mathrm{N}} B_0} \\ &= 0.6036 \pm 0.0014 \end{aligned} \tag{8.1}$$

The magnitude of the magnetic field actually sensed by the nucleus differs slightly from the external magnetic field B_0 due to the diamagnetic effect by the chemical shift. The magnitude of the correction term of the diamagnetic shift is known to be

$$\sigma = 40 \pm 15 \text{ ppm},$$

from the literature value [44, 45]. From Eq. 2.30, the total magnetic field changes to

$$\begin{aligned} B &= B_0(1-\sigma) \\ &= 500.96 \pm 0.16 \text{ mT}. \end{aligned} \tag{8.2}$$

Therefore, the final value of g-factor is

$$|g|_{\text{corrected}} = 0.6036 \pm 0.0014.$$

8.2 Ground-state spin parity and configuration of ^{21}O

A nucleus ^{21}O comprises of eight protons forming the $Z = 8$ closed shell and five neutrons occupying sd orbits outside the $N = 8$ closed shell. Therefore, its ground-state spin parity I^π is dominantly formed by the five neutrons in the sd orbit. In an extreme single-particle model, the ground state of ^{21}O is represented by the configuration with one unpaired neutron in the $d_{5/2}$ orbit, i.e., $|[(sd)^4]^{0^+}(d_{5/2})\rangle^{I^\pi=5/2^+}$. In this configuration, the ground-state spin parity becomes $I^\pi = 5/2^+$, similar to the odd-mass neutron-rich oxygen isotopes ^{17}O and ^{19}O, which also have one unpaired neutron in the $d_{5/2}$ orbit. Regarding the configuration of $[(sd)^4]^{0^+}$, $[(d_{5/2})^4]^{0^+}$ or $[(d_{5/2})^2(s_{1/2})^2]^{0^+}$, or the admixture of thereof will be main components.

The neighboring nuclei of ^{21}O having the even-Z number nearest to $Z = 8$ and the same neutron number $N = 13$ are ^{23}Ne and ^{19}C, whose spin parities are also formed by the five neutrons in the sd orbit like as ^{21}O. Interestingly, however, their spin parities are different from each other as follows.

$$\begin{aligned} I^\pi(^{23}\text{Ne}_{\text{g.s.}}) &= 5/2^+(Z=10) \text{ and} \\ I^\pi(^{19}\text{C}_{\text{g.s.}}) &= 1/2^+(Z=6) \text{ [46]} \end{aligned} \tag{8.3}$$

Provided the neutron configuration of ^{21}O is approximately same as ^{23}Ne, which is natural in a simple shell model, $I^\pi = 5/2^+$ is suggested for the ^{21}O ground state. However, if ^{21}O neutrons are in the same situation of ^{19}C, the $I^\pi = 1/2^+$ assignment is also possible.

Experimentally, the structure of ^{21}O has been investigated through, the multi-nucleon transfer reaction [47] and in-beam γ-ray spectroscopy [48], in which$I^\pi = 5/2^+$ has been tentatively assigned to the ^{21}O ground state. In Ref. [49], the momentum distribution was measured in the one-neutron removal (knockout) reaction, and the same assignment of $I^\pi = 5/2^+$ as these previous studies has been claimed. In a more recent study, the $d(^{20}\text{O}, ^{21}\text{O})p$ reaction as the (d, p) reaction in inverse kinematics was applied for the structure study on ^{21}O [50]. This study also claims the $5/2^+$ assignment, because a measured differential cross sections to the ^{21}O ground state can be well reproduced with a dominant $\ell = 2$ component. However, according to the literature [51], the $I^\pi = 5/2^+$ assignment is still treated as a tentative result. In such a situation, it is important to investigate the ^{21}O ground state through g factor by NMR spectroscopy, which is a completely different observable from those obtained in nuclear-reaction-based studies.

There is no special reason for the inversion of the single-particle levels ($\nu d_{5/2}$) and ($\nu d_{3/2}$); thus, here, we consider two possible configurations in which an unpaired $d_{5/2}$ or $s_{1/2}$ neutron carries approximately entire nuclear spin parity $I^\pi = 5/2^+$ or $1/2^+$, respectively. Then, the g factors corresponding to the possible two configurations $|[(sd)^4]^{0^+}(d_{5/2})\rangle^{I^\pi=5/2^+}$ and $|[(sd)^4]^{0^+}(s_{1/2})\rangle^{I^\pi=1/2^+}$, calculated with the bare g factors (i.e., the Schmidt value) are given as $g_{\rm Schmidt}(d_{5/2}) = -0.765$ and $g_{\rm Schmidt}(s_{1/2}) = -3.826$, respectively. Although a sign was not assigned to the experimental g factor determined in the present study, i.e., $|g_{\rm exp}(^{21}{\rm O})| = 0.6036 \pm 0.0014$, we can assign $I^\pi = 5/2^+$ to the ^{21}O ground state even only from the comparison of the absolute value to the above-noted Schmidt values due to the large difference in $g_{\rm Schmidt}(d_{5/2})$ and $g_{\rm Schmidt}(s_{1/2})$ (as much as 4.9-fold difference).

Because we took the bare g factors in the above analysis, the single-particle g factors, $g(d_{5/2})$ and $g(s_{1/2})$, reduce to the Schmidt values. To make the discussion more quantitative, we include the effects [52, 53] of the meson exchange currents and second-order configuration mixing by taking the effective g factors of Ref. [54]. Then, the single particle g factors are given as $g_{\rm eff}(d_{5/2}) = -0.729$ and $g_{\rm eff}(s_{1/2}) = -3.449$, respectively. Here, the difference between them is reduced only from 4.9 times to 4.6 times, even when the effective g factors are adopted. This 4.6-times difference is still large and it does not compromise the sensitivity of the I^π assignment. Thus, the $I^\pi(^{21}{\rm O}_{\rm g.s.}) = 5/2^+$ assignment remains unchanged.

It is interesting to compare the $|g_{\rm exp}(^{21}{\rm O})|$ value with the g factors of the neighboring nuclei ^{17}O and ^{19}O in the neutron-rich oxygen isotope, whose ground state I^π are known to be $5/2^+$, and thus, their single particle g factors are commonly $g_{\rm eff}(d_{5/2})$. We found that the reported experimental g factors for ^{17}O and ^{19}O, i.e., $g_{\rm exp}(^{17}{\rm O}_{\rm g.s.}) = -0.75752(4)$ [42] and $|g_{\rm exp}(^{19}{\rm O}_{\rm g.s.})| = 0.61278(3)$ [55], respectively, are close to the present $|g_{\rm exp}(^{21}{\rm O})|$ value in comparing their absolute values. This observation also suggests the $I^\pi(^{21}{\rm O}_{\rm g.s.}) = 5/2^+$ assignment. Here, we are certain that $I^\pi(^{21}{\rm O}_{\rm g.s.})$ is $5/2^+$; thus, the ground-state nuclear magnetic moment of ^{21}O can be determined as $|\mu_{\rm exp}(^{21}{\rm O}_{\rm g.s.})|$ $= (1.5090 \pm 0.0035)\ \mu_{\rm N}$.

8.3 Comparison with theoretical models

The experimental $\mu_{\rm exp}(^{21}{\rm O})$ value was compared to the results of shell-model calculations. Here, three unique sets of effective interactions were adopted. The first one, referred to as USD [5], was introduced by Wildenthal in the 1990s. This is a parametric effective interaction with an inert core of ^{16}O, created to reproduce experimental energy levels of sd-shell nuclei. This interaction has been used as a "standard" interaction in the sd model space for a long time. The other two interactions, denoted USDA and USDB [6], are new interactions introduced by Brown and Richter in 2006 by improving the USD interaction with updated datasets of binding energies and energy levels accumulated over 20 years after the USD interaction was determined. Both have different procedures relative to parameter convergence in the interaction constructing process; however, they are essentially very similar interactions.

With these three interactions, the shell-model calculations were conducted for the ^{21}O using a code KSHELL [56] and the above-mentioned effective $\hat{\mu}$ operator. The predicted μ moments for the ^{21}O ground state are given in Table 8.2, in which the Schmidt moment and single-particle moment for ^{21}O (i.e., those for the $d_{5/2}$ neutron) are also shown for comparison.

First, looking at the calculation result for the USD interaction, the theoretical value shows quenching from $\mu_{\rm eff}(\nu d_{5/2})$ by the difference $\delta\mu \sim 0.4\ \mu_{\rm N}$ as an effect of configuration mixing. In ^{21}O, the admixture of proton-excited configurations is suppressed due to the LS-closed ^{16}O hard core. Thus, the effect of configuration mixing is approximately caused only by the neutron side. Its major part will be explained by the first-order effect of the M1 core polarization [58]. According to the first-order core-polarization theory, the contribution to the magnetic moment from the M1 core polarization has a common factor $-[1+(-)^{1/2+\ell-j}(j+1/2)](g_s-g_\ell)$, under the assumption of a δ-function-type residual interaction. From the sign of this factor, it can be shown that the corrections are directed inward from the Schmidt lines.

In the case of ^{21}O, the second term of Eq. (8.4) plays an important role.

$$\begin{aligned}
\psi(^{21}\mathrm{O}_{\rm g.s.}) &= c_0|\,[(sd)^4]^{0^+}(d_{5/2})\rangle^{I^\pi=5/2^+} \\
&+ c_1|\,[(sd)^2]^{0^+}[d_{5/2}d_{3/2}]^{1^+}(d_{5/2})\rangle^{I^\pi=5/2^+} \\
&+ c_2|\cdots\rangle^{I^\pi=5/2^+} \\
&+ \cdots \qquad (8.4) \\
&\quad ({c_0}^2+{c_1}^2+{c_2}^2\cdots=1)
\end{aligned}$$

The second (c_1) term represents that one of the $d_{5/2}$-neutron pairs forming $I^\pi=0^+$ excited to the $d_{3/2}$ orbit by a residual interaction with another active $d_{5/2}$ neutron forms $I^\pi=1^+$ with the partner neutron left in the $d_{5/2}$ orbit. Provided that the $I^\pi=1^+$ pair further couples with the active $d_{5/2}$ neutron to form the total spin parity $I^\pi=5/2^+$, this configuration can mix into the ground state wave function.

Remarkably, this c_1 term in Eq. (8.4) can cause large quenching as an off-diagonal M1 matrix element in first order, in spite of the expected small amplitude of it. Even a small probability $|c_1|^2 \sim$0.01 of the M1 core polarization component may give rise to correction in the order of 10% to the magnetic moment. In the present ^{21}O case, $|c_1|^2 \sim$1.5% was predicted from the shell model, which is sufficiently large to cause $\delta\mu \sim 0.4$, considering a concentration to the main configuration with $|c_0|^2 \sim 80\%$.

Next, the predicted μ moments with the USD, USDA, and USDB interactions are compared. As shown in Table 8.2, these three calculations differ by a maximum of $\delta\mu \sim 0.05\ \mu_{\rm N}$. The effective M1 operator has ambiguity $\sim 0.1\ \mu_{\rm N}$ due to the accuracy of the effective g factors; thus, these three μ moments should be regarded as nearly identical. Then, taking the average of the three predicted values, it can be said that these three calculations predict $\mu = -1.41\ \mu_{\rm N}$ in common. This theoretical μ moment agrees with the present experimental $\mu_{\rm exp}(^{21}\mathrm{O})$ moment with only a slight difference.

These interactions cannot describe the nuclear structure affected by the "island of inversion" [57], which is a phenomenon that causes anomalous nuclear structure in the vicinity of the neutron-rich *sd* shell around neutron number $N = 20$ [6]. This phenomenon is caused by the effective level inversion of the *sd* shell and *pf* shell thereon. Therefore, for such "island of inversion" nuclei it is necessary to perform a shell-model calculation in a large model space including all these shells and more higher shell [59]. In the case of ^{21}O, however, as examined in the above discussion, both the ground-state I^π and μ moment can be well reproduced by the shell-model calculation within a *sd* model space, suggesting that ^{21}O is a "normal" nucleus which is not influenced by the "island of inversion" phenomenon.

Apart from shell-model-based studies, recently a random phase approximation (RPA) calculation was performed [60] to describe the core polarization effect of the doubly-magic core in odd-even nuclei using a single-particle basis generated by Hartree-Fock calculations. In this study, nuclear moments were the focus because nuclear moments are quite sensitive to the interaction between the unpaired nucleon and other nucleons, which plays an important role in strongly modifying pure shell-model predictions. The calculations were performed using two different parametrizations of the finite-range density-dependent Gogny interactions based on the traditional D1S force [61] and the recently proposed D1M one [62]. The structure of ^{21}O was calculated taking ^{22}O as a core coupled with a $\nu d_{5/2}$ hole, and the magnetic moment of ^{21}O was deduced as $\mu_{\mathrm{RPA(D1S)}} = -1.667$ and $\mu_{\mathrm{RPA(D1M)}} = -1.487\ \mu_{\mathrm{N}}$ with the D1S and D1M interactions, respectively. Comparing absolute values of these predictions with the present $|\mu_{\mathrm{exp}}(^{21}\mathrm{O})| = 1.5090 \pm 0.0035)\ \mu_{\mathrm{N}}$, $\mu_{\mathrm{RPA(D1M)}}$ agrees with the experimental μ moment, but the reduction in μ from the $\nu d_{5/2}$ single-particle moment will be slightly insufficient for $\mu_{\mathrm{RPA(D1S)}}$.

Table 8.2: Comparison of experimental magnetic moments ($|\mu_{\mathrm{exp}}(^{21}\mathrm{O})|$) obtained for the ^{21}O ground state in the present study with shell-model (USD, USDA, and USDB) and RPA (RPA(D1S) and RPA(D1M)) predictions. The $\mu_{\mathrm{exp}}(^{21}\mathrm{O})$ moment was calculated from the determined $g_{\mathrm{exp}}(^{21}\mathrm{O})$ factor and the assigned $I^\pi = 5/2^+$. The Schmidt moment (μ_{Schmidt}) for a $d_{5/2}$ neutron and the corresponding single particle moment ($\mu_{\mathrm{eff}}(\nu d_{5/2})$) are also shown.

	μ moment (μ_{N})
$\lvert\mu_{\mathrm{exp}}(^{21}\mathrm{O})\rvert$	1.5090(35)
μ_{Schmidt}	-1.913
$\mu_{\mathrm{eff}}(\nu d_{5/2})$	-1.823
USD	-1.435
USDA	-1.382
USDB	-1.421
RPA(D1S)	-1.667
RPA(D1M)	-1.487

Chapter 9

Conclusion

To the best of our knowledge, in this study, the magnetic moment of the ground state of ^{21}O was measured for the first time using the β-NMR method with a spin-polarized RIB.

Prior to the magnetic moment measurement, nuclear spin polarization was measured using an AFR method. In the AFR method, it is possible to measure the degree of polarization without a frequency search; thus, the parameters (e.g., emission angle, momentum selection, measurement sequence, target thickness) required to produce polarization can be optimized beforehand. Therefore, we can focus on frequency search under optimum polarization and yield conditions. A nuclear spin polarization of ^{21}O was produced using the projectile fragmentation reaction and nucleon pick-up reaction. Spin-polarized ^{21}O beams were implanted into the CaO crystal placed in the static magnetic field $B_0 = 481(30)$ mT, polarization is measured using an AFR measurement. In the case of ^{21}O, the asymmetry parameter can only obtain the upper limit value and the lower limit value because there are excitation levels where the spin of the daughter nucleus ^{21}F is not decided. Therefore, $|P| > 4.9\%$ is the lower limit value, which can potentially yield even greater polarization.

In this study, by introducing fast switching system in the β-NMR measurement, it became possible to perform more efficient measurement than the conventional system. In the proposed system, the number of variable capacitors in the LCR tank circuit can be increased from one to three, capacitors can be switched sequentially using the relay circuit, and a single wide frequency search can be performed. Because the frequency range to be searched is wide in the nucleus where the spin is not determined such as the case of ^{21}O, the introduction of this system is very useful to perform the measurement efficiently in a limited time.

The β-NMR measurement and data analysis indicate that the g-factor of the ground state of ^{21}O is $|g_{\mathrm{exp}}| = (0.6036 \pm 0.0014)$. Experimental results indicating $I^{\pi}(^{21}\mathrm{O}_{\mathrm{g.s.}}) = 5/2^{+}$ have been reported; however, that result has not been determined. Then, the g factors corresponding to two possible configurations, i.e., $|[(sd)^4]0^+(d_{5/2})\rangle^{I^{\pi}=5/2^+}$ and $|[(sd)^4]0^+(s_{1/2})\rangle^{I^{\pi}=1/2^+}$, calculated using the effective g factors are given as $g_{\mathrm{eff}}(d_{5/2}) = -0.729$ and $g_{\mathrm{eff}}(s_{1/2}) = -3.449$, respectively. Although a sign was not assigned to the experimental g factor determined in the present study, we can definitely assign $I^{\pi} = 5/2^{+}$ to the ^{21}O ground state even only from the comparison of the absolute value to the above-noted effective g factors values, due to the large difference (as much as 4.6 fold)

in $g_{\rm eff}(d_{5/2})$ and $g_{\rm eff}(s_{1/2})$. Now that we are certain that the $I^{\pi}(^{21}{\rm O}_{\rm g.s.})$ is $5/2^{+}$, the ground-state nuclear magnetic moment of ^{21}O can be determined as $|\mu_{\rm exp}(^{21}{\rm O}_{\rm g.s.})| = (1.5090 \pm 0.0035)\ \mu_{\rm N}$.

Next, this result was compared to the shell model calculation using KSHLL code. The calculated values using the USD, USDA, and USDB interactions are averaged, $\mu = -1.41 \mu_{\rm N}$. The effective M1 operator has ambiguity $\sim 0.1\ \mu_{\rm N}$ due to the accuracy of the effective g factors; thus, this theoretical μ moment nearly agrees with the present experimental $\mu_{\rm exp}(^{21}{\rm O})$ moment, with only a slight difference in value. Recently, as RPA calculation was performed to describe the core polarization effect of the doubly-magic core in odd-even nuclei using a single-particle basis generated by Hartree-Fock calculations. The magnetic moment of ^{21}O was deduced as $\mu_{\rm RPA(D1S)} = -1.667$ and $\mu_{\rm RPA(D1M)} = -1.487\ \mu_{\rm N}$ with the D1S and D1M forces, respectively. Comparing the absolute values of these predictions with the present $|\mu_{\rm exp}(^{21}{\rm O}_{\rm g.s.})| = (1.5090 \pm 0.0035)\ \mu_{\rm N}$, $\mu_{\rm RPA(D1M)}$ agrees with the experimental μ moment.

From these results, I^{π} of the ground state of ^{21}O was $5/2^{+}$, and ^{21}O was found to have a "normal" nucleus. Anomalous structures, such as those found in oxygen isotope ^{23}O, do not develop in ^{21}O, which is consistent with the measurement result of the interaction cross section shown in Chapter 1. From the electric quadrupole moment, it is possible to know the shape and deformation of the nucleus, so measuring the electric quadrupole moment of ^{21}O is important to discuss the nuclear structure. It is also very interesting to measure magnetic moment of ^{23}O where abnormal structure is predicted because it can obtain information about the nuclear structure.

Acknowledgments

I would like to thank all of these who have helped to make this work successful.

I am deeply grateful to Prof. A. Ozawa who has undertaken the chief examiner of my doctoral thesis for helpful advice and discussions on the whole of this work.

Prof. Y. Miake, Prof. T. Nakatsukasa and Associate Prof. T. Yamaguchi were undertaken the sub-chief examiner. I would like to thank them for their advises, encouragements and reading this thesis.

I would like to express my special thanks to Dr. H. Ueno for his advises, guidance and encouragement to complete the present study. Without his supports on scientific researches, I could not make the present work fruitful.

I wish to express my gratitude to Dr. D. Nagae who taught me a lot of physics and experimental techniques.

I would like to express gratitude to Dr. T. Nagatomo who supported me and taught me a lot of experimental techniques and physics.

I wish to thank Dr. Y Abe who always supported me and gave me the helpful advice.

My thanks are due to my colleagues at Nuclear Spectroscopy Laboratory in RIKEN and Ozawa laboratory in University of Tsukuba for helpful collaboration.

To collaborators in RIKEN, I wish to thank Dr. H. Yamazaki for preparing the stopper crystals which are the key points of the experiment. I would like to thank Dr. Ichikawa for using RIPS, how to proceed with the experiment, and correcting the paper. I wish to thank Dr. A. Takamine for not only about experiments and research but also various consultations. I would like to thank Dr. H. Nishibata, Dr. T. Sato and Dr. K. Imamura for helping me prepare for the experiment from morning till late at night. I wish to thank Mr. A. Gladkov for discussing lots of things while doing experiment preparations together and able to carry out the experiment and always supported me.

I wish to express my gratitude to β-NMR experiment collaborators, Prof. K. Asahi, Prof. W. Y. Kim, Dr. G. Georgiev, Dr. J. M. Daugas, Ms. T. Fujita, Mr. L. C. Tao, Mr. T. Egami, Mr. D. Tominaga, T. Kawaguchi, Mr. M. Sanjo, Mr. W. Kobayashi and Mr. Y. Nakamura. Also, I would like to express gratitude to AFR experiment collaborators, Associate Prof. A. Yoshimi, Dr. N. Sakamoto, Dr. T. Furukawa, Dr, X. F. Yang, Mr. N. Yoshida, Mr. M. Chikamori, Ms. H. Shirai, Mr. Y. Ohtomo, Mr. T. Suzuki and Ms. E. Hikota.

To collaborators in University of Tsukuba, I would like to thank Dr. T. Moriguchi, Dr. S.

Suzuki, Mr. S. Fukuoka, Mr. N. Inaba, Mr. Y. Saito, Mr. S. Okada, Mr. K. Sawahata, Ms. Y. Ichikawa, Mr. Y. Tajiri, Mr. K. Hiraishi, Mr. T. Matsumoto for their helpful and kindly support in my Tsukuba life.

I also thank researchers around me, Prof. T. Minamisono, Prof. H. Miyatake, Prof. M. Wada, Associate Prof. K. Matsuta, Associate Prof. K. Sasa, Dr. M. Mihara, Dr. T. Komatsubara, Dr. Y. Ito, Dr. S. Kimura and Dr. M Mukai for helpful and kindly support.

I would like to thank researchers and students in CYRIC at Tohoku University, Prof. M. Itoh, Dr. Y. Matsuda, Dr. K. Harada, Dr. U. Dammalapati, Dr. H. Kawamura, Dr. T. Inoue, Dr. K. Tanaka, Ms. A. Uchiyama, Mr. Y. Nasu, Mr. K. Sakamoto, Mr. J. Okamoto, Ms. S. Ito, Mr. K. Karasudani, Ms. R. Yoshioka, Mr. K. Kasamatsu, Mr. S. Ishida, Ms. A. Nakagawa, Mr. K. Nozawa, Mr. R. Maeda for their helpful and kindly support in my Tohoku life.

I am grateful for Junior Research Associate Program in RIKEN.

The shell model calculations were carried out by using the nuclear shell-model code "KSHELL" by Dr. N. Shimizu.

I am grateful to the staffs at RIKEN Ring Cyclotron for their support during the running of the experiments.

Finally, I would like to express my special thanks to my family for understanding and supporting my long school life.

Appendix A

Data analysis of ^{21}O

To obtain appropriate values for the resonance shape, a simulation of the AFP spin reversal process was performed in consideration of the actual conditions for the RF fields [43]. In this simulation, it was possible to verify in which area the reversal in AFP occurred at 100% by using the actual experimental conditions as the input parameters. Table A.1 shows simulation input parameters, and the result is plotted in Figs. A.1 and A.2.

Table A.1: AFP simulation input parameters

run number	50	52
g-factor	0.6050	0.60504
B_0 [G]	5008	5008
$B_{\mathrm{1cp-max}}$ [G]	2.316	2.044
$B_{\mathrm{1cp-min}}$ [G]	0.735	0.649
g-width [%]	0.132	0.110
RF time [ms]	5	5
Trapezoid shape		
Lower	1	1
Middle	10	10
Higher	1	1

Here, $f_{\mathrm{AFP}}(x)$ was introduced as a response function that reproduces the simulation result as follows.

$$f_{\mathrm{AFP}}(x) = \begin{cases} A_0 \exp\left(-(\frac{x-x_0+\Delta x/2}{2\sigma_{\mathrm{AFP}}})^2\right) + b & (x < x_0 - \Delta x/2) \\ A_0 + b & (x_0 - \Delta x/2 < x < x_0 + \Delta x/2) \\ A_0 \exp\left(-(\frac{x-x_0-\Delta x/2}{2\sigma_{\mathrm{AFP}}})^2\right) + b & (x_0 + \Delta x/2 < x) \end{cases} \tag{A.1}$$

Here, A_0 is the amplitude of R/R_{off} ratio, x_0 is the center of frequency, Δx is the AFP width, σ_{AFP} is the Gaussian dispersion, and b is the baseline shift. By fitting the simulation results with this function, we determined the values of σ_{AFP} and Δx. The results are shown in Figs. A.3 and A.4 and Table A.2.

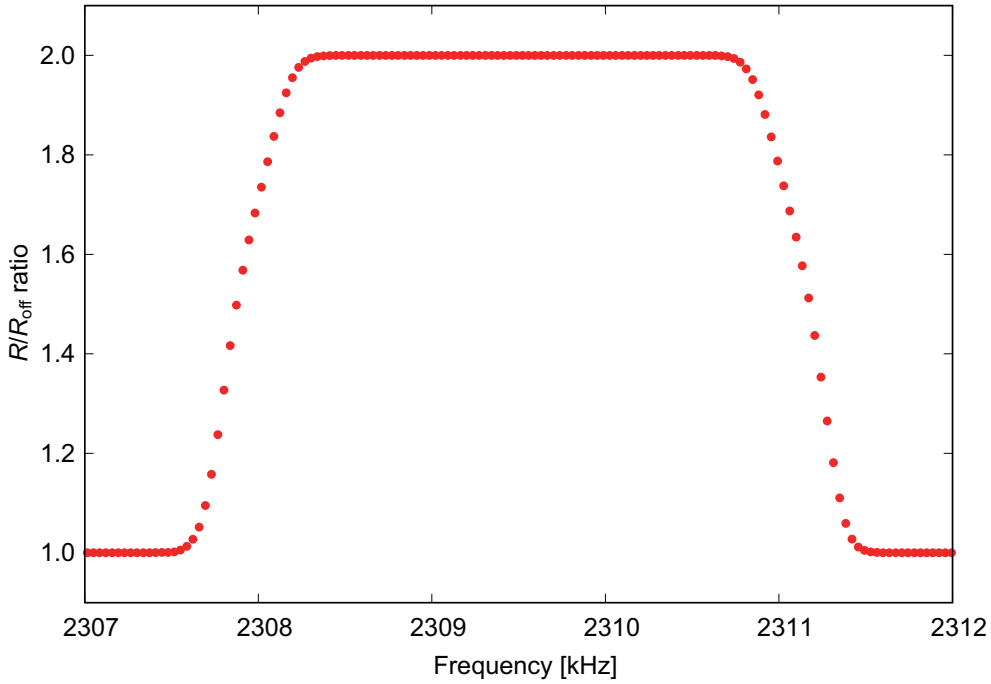

Figure A.1: Results of AFP simulation of run50

Table A.2: Results of simulation fitting

run number	50	52
Δx	2.594 ± 0.0014	2.142 ± 0.0012
σ_{AFP}	0.2728 ± 0.0058	0.2497 ± 0.0050

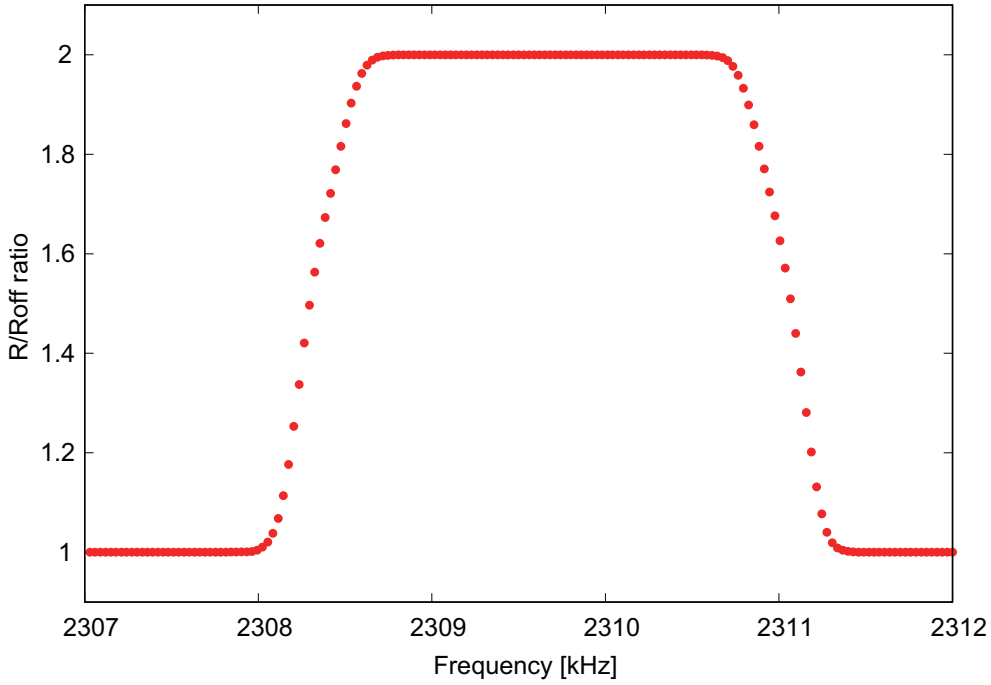

Figure A.2: Results of AFP simulation of run52

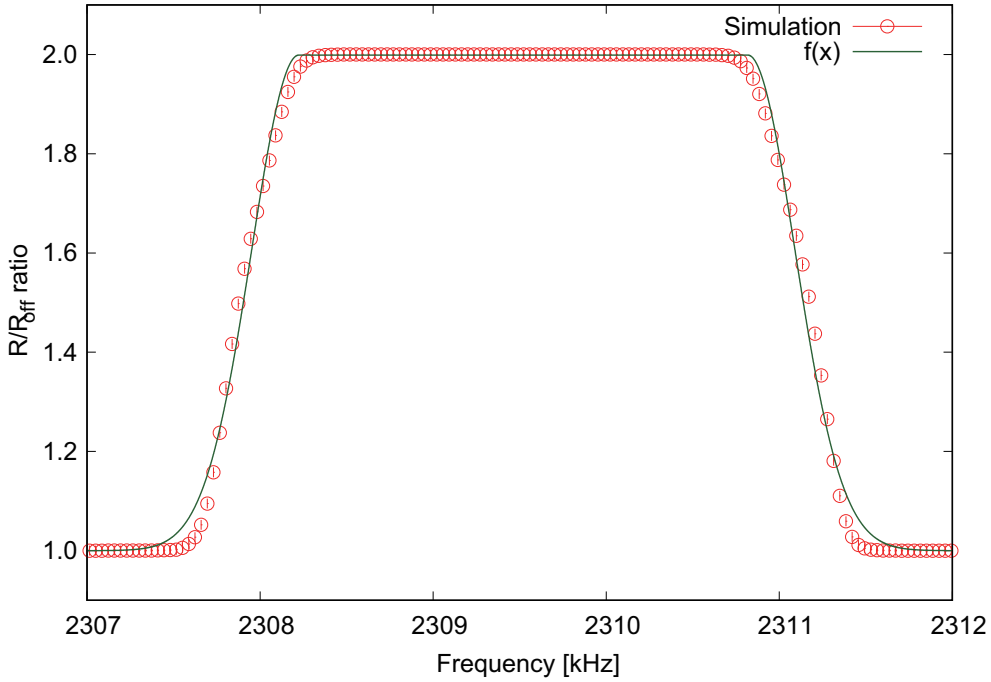

Figure A.3: Results of simulation fitting of run50

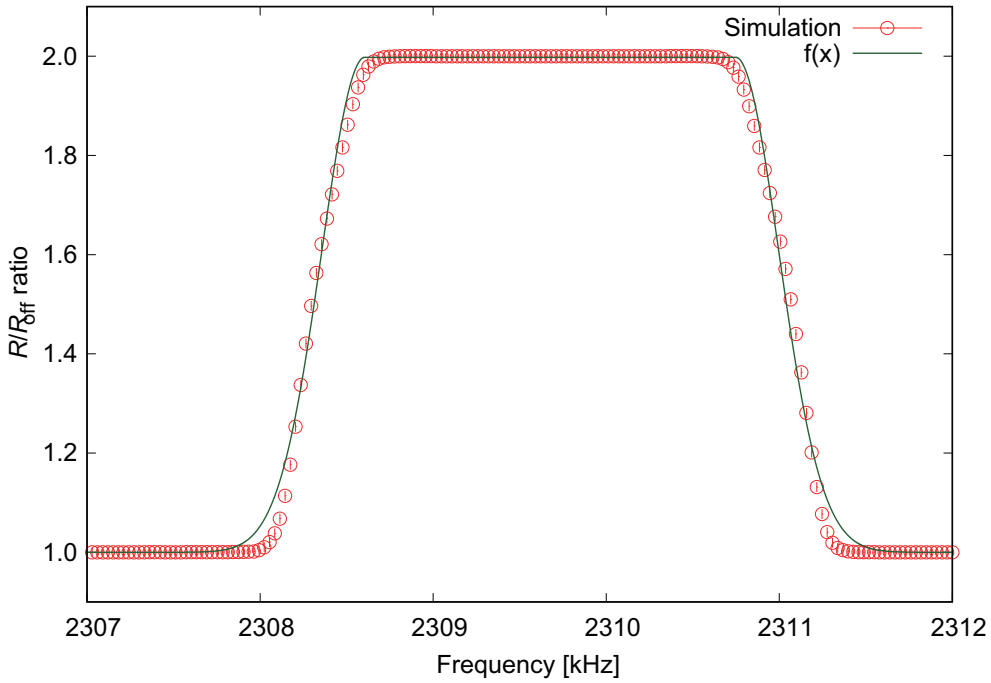

Figure A.4: Results of simulation fitting of run52

Then, we introduced the function $F_{\mathrm{AFP}}(x)$ convolving Gaussian function $g(x)$ in Eq. A.2.

$$g(x) = \frac{1}{\sqrt{2\pi}\sigma_{\mathrm{EB}}} \exp(-(\frac{x}{2\sigma_{\mathrm{EB}}})^2)$$

$$F_{\mathrm{AFP}}(x) = (f_{\mathrm{AFP}} * g)(t) = \int f_{\mathrm{AFP}}(\tau) g(t-\tau) d\tau \tag{A.2}$$

Where σ_{EB} is width of extra broadening.

Finally, σ_{AFP} and Δx were fixed, and the experimental data were fitted with $F_{\mathrm{AFP}}(x)$. The results are shown in Figs. A.5 and A.6 and Table A.3.

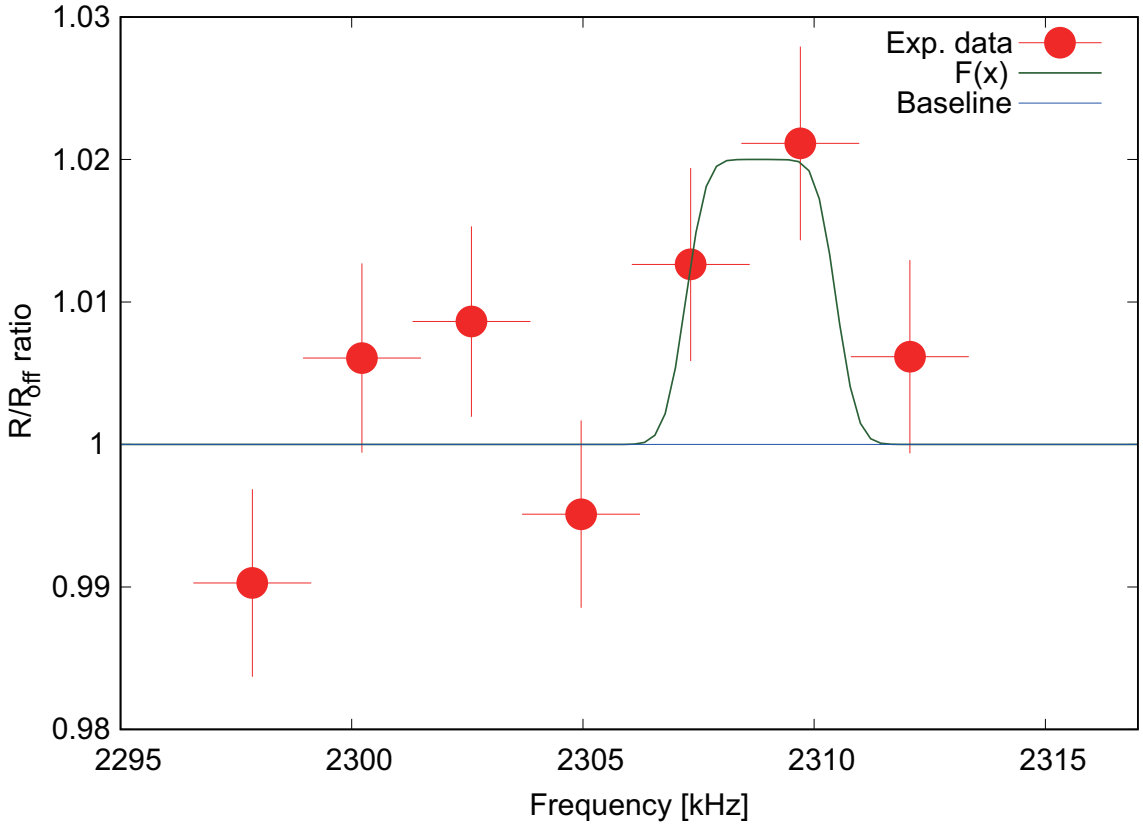

Figure A.5: Results of experimental data fitting of run50

Table A.3: Results of experimental data fitting

run number	50	52
x_0	2308.85 ± 0.98	2309.79 ± 0.52
σ_{EB}	0.30 ± 3.04	0.23 ± 0.53
χ^2	1.526	0.507

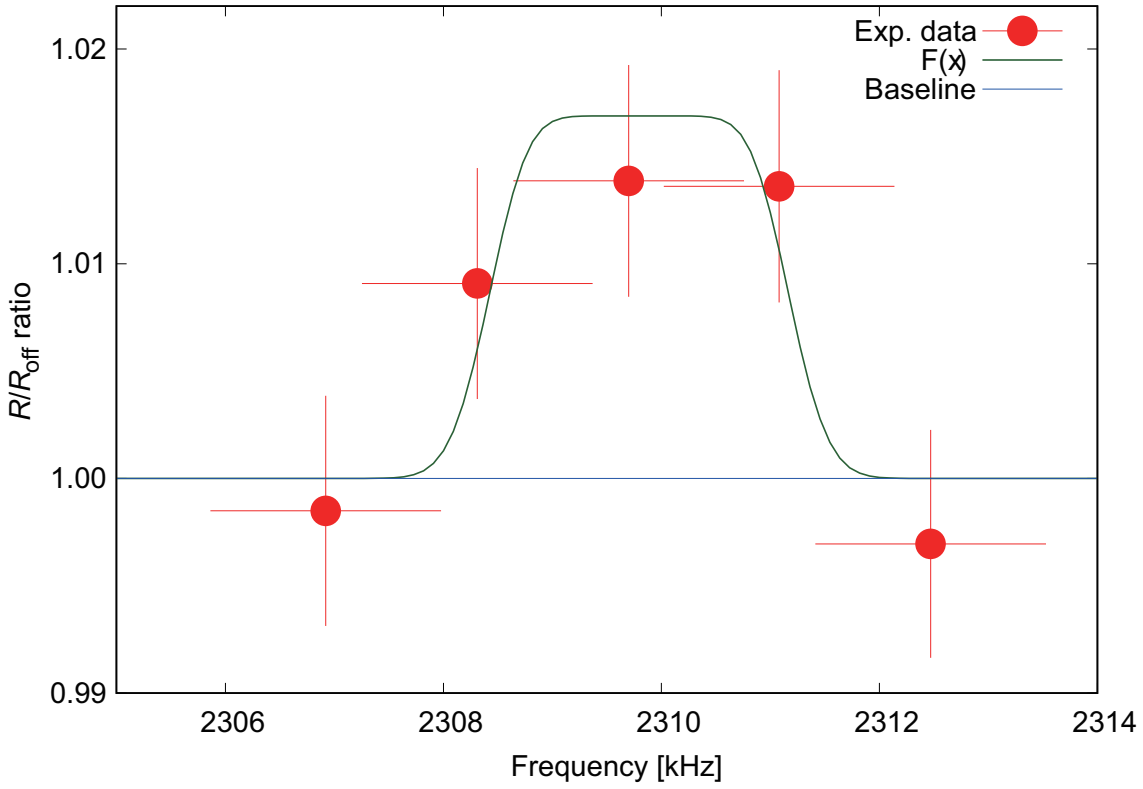

Figure A.6: Results of experimental data fitting of run52

Based on the above analysis, the center frequency was obtained as follows:

$$\begin{aligned} \nu_{\mathrm{L}} &= 2308.85 \pm 0.98(\text{statistic error}) \pm 0.30(\text{systematic error})\text{kHz (run50)}, \\ &= 2309.79 \pm 0.52(\text{statistic error}) \pm 0.23(\text{systematic error})\text{kHz (run52)}, \end{aligned} \tag{A.3}$$

Here, it is necessary to consider spectrum spread. The following can be considered causes of spectrum spread.

1) Change in the effective magnetic field by RF magnetic field B_1

2) Integration of spectrum by frequency modulation

In the case of a macroscopic system comprising many elements, the aggregate contribution of the individual elements is given as a Gaussian distribution.This is the central limit theorem in statistics, which is why the NMR spectrum observed by individual NMR is approximately Gaussian.

1) Change in the effective magnetic field by the RF magnetic field B_1

The angle between the spin polarization vector, which precess angular frequency ω about the effective magnetic field B_{eff} and the z-axis (direction of the static magnetic field B_0) is α. In addition, if the angle formed by B_{eff} and the z-axis is θ, the following equation holds (Rabi's formula).

$$\cos\alpha = 1 - 2\sin^2\theta \sin^2 \frac{1}{2}at \tag{A.4}$$

Here, $\sin\theta$, ω_0, ω_1, and a are expressed as follows.

$$\begin{aligned} \sin\theta &= \frac{\omega_1}{\sqrt{(\omega_0-\omega)^2+\omega_1^2}} \\ \omega_0 &= -\gamma B_0 \\ \omega_1 &= -\gamma B_1 \\ a^2 &= (\omega_0-\omega)^2+\omega_1^2 \end{aligned} \tag{A.5}$$

The spin reversal ratio is proportional to $\sin^2\theta$ and has a Lorentzian type spectrum. Here, when spectrum spread is calculated from $\omega_1 = -\gamma B_1$, it becomes as follows.

$$\Delta f_{B_1} = \frac{|\gamma B_1|}{2\pi} \sim 1.07kHz \tag{A.6}$$

2) Integration of spectrum by frequency modulation

Since the RF magnetic field used for β-NMR changes the frequency using FM, the observed spectrum is integrated over the range $[f-\Delta f_{\text{FM}}, f+\Delta f_{\text{FM}}]$ from the original frequency distribution. Therefore, if the FM width is greater than the spread of the frequency distribution due to the above fluctuation of the magnetic field, the spread of the observed spectrum is determined by Δf_{FM}. Conversely, if the FM width is sufficiently narrow, the spread of the spectrum is given by the magnitude of the magnetic field fluctuation. The FM width used for the final measurement was $\Delta f_{\text{FM}} = 2.55$ kHz, which is $\Delta f_{\text{FM}} > \Delta f_{B_1}$ when compared to the fluctuation of the magnetic field obtained above. The observed broadening of spectrum was $\sigma_{\text{EB}} = (0.30 \pm 3.04)$ kHz (Table A.3); thus, in this measurement, broadening of the spectrum was determined by the FM width.

Appendix B

Production of ^{21}F beam

Table B.1 listed the RIPS parameters for the β-NMR measurement of ^{21}F.

Table B.1: Comparison of RIPS parameters

	present experiment	previous experiment
Primary beam	$^{22}Ne^{10+}$	$^{22}Ne^{10+}$
Incident energy	69.18 A MeV	66.4 A MeV
Target material	^{nat}C	^{nat}C
Target thickness	56.3 mg/cm^2	225.3 mg/cm^2
Emission angle θ_L	2.6°	2.6°
Emission angle θ_h	$2.1° - 6.0°$	$1.6° - 3.6°$
Momentum region	7.44 - 7.52 GeV/c	7.44 - 7.52 GeV/c
F1 degrader material	Aluminum	Aluminum
F1 degrader thickness	583 mg/cm^2	583 mg/cm^2
F1 degrader angle	3.13 mrad	3.13 mrad

To identify ^{21}F from the other isotopes, we measured the time of flight (TOF) of the beam and energy loss (ΔE) in the Si detector located F2. The ΔE-TOF spectrum of ^{21}F with the 0.25-mm thick C target is shown in Fig. B.1. The ΔE spectrum of ^{21}F is shown in Fig. B.2. As shown in Figs. B.1 and B.2, three components that correspond to ^{21}F, ^{19}O and ^{18}N were observed.

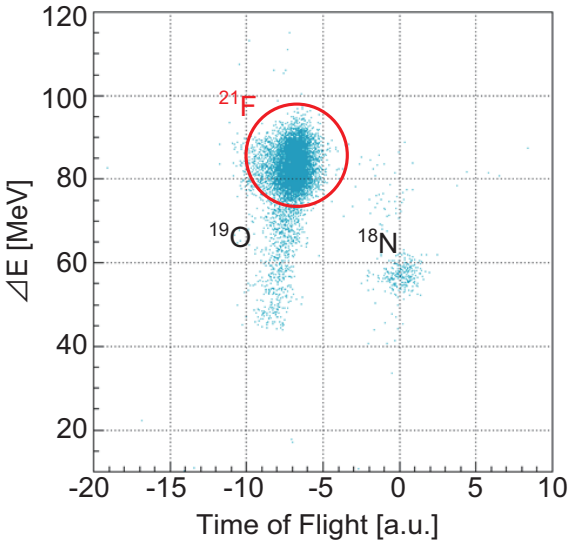

Figure B.1: Particle Identification of ^{21}F

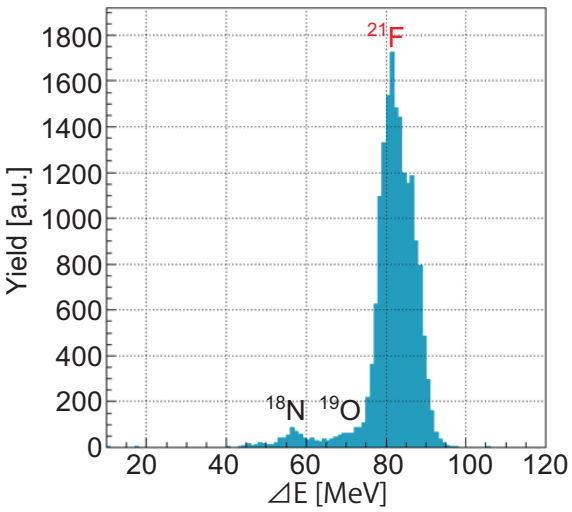

Figure B.2: Energy loss of ^{21}F

The momentum distribution measured in this experiment is shown in Fig. B.3. In this figure, the gray zone shows region of selected momentum acceptance for AFP-NMR measurement.

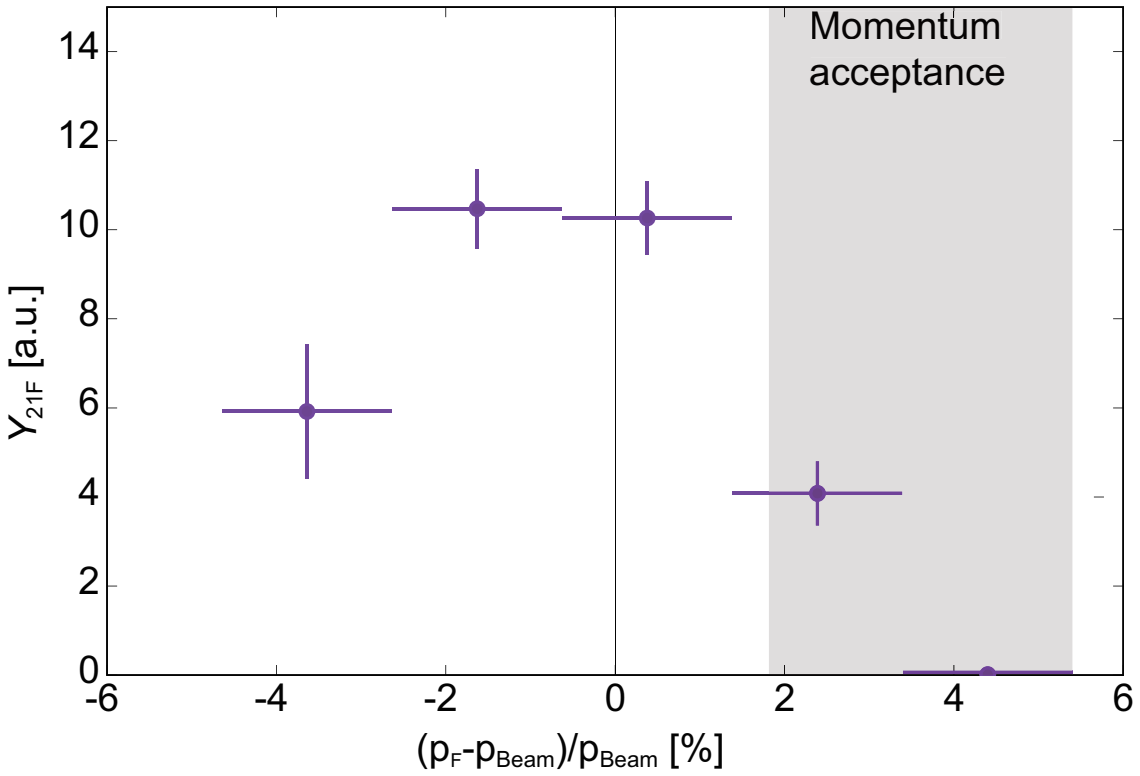

Figure B.3: Momentum distribution of ^{21}F

Appendix C

AFP-simulation of ^{21}F

Figure C.1 shows final results of AFP-NMR measurement of ^{21}F.

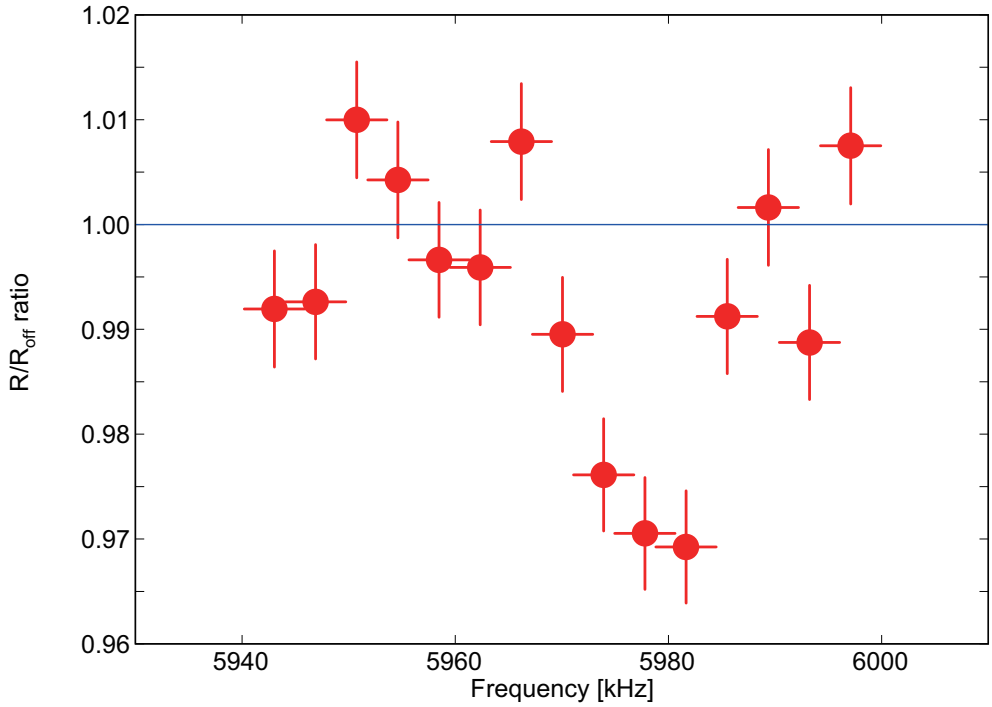

Figure C.1: Final results of AFP-NMR measurement of ^{21}F

In this simulation, it was possible to verify in which area the reversal in AFP occurred at 100% by using the actual experimental conditions as the input parameters. Table C.1 shows simulation input parameters, and the result is plotted in Fig. C.2 Table C.1 shows input parameters of AFP simulation.

Table C.1: Input parameters of AFP simulation of ^{21}F

g-factor	1.5684
Static magnetic field B_0	500.0 mT
$B_{1cp-max}$	0.8576 G
$B_{1cp-min}$	0.2528 G
g-width	0.089%
RF time	5 ms
Trapezoid shape	
Lower	1
Middle	10
Higher	1

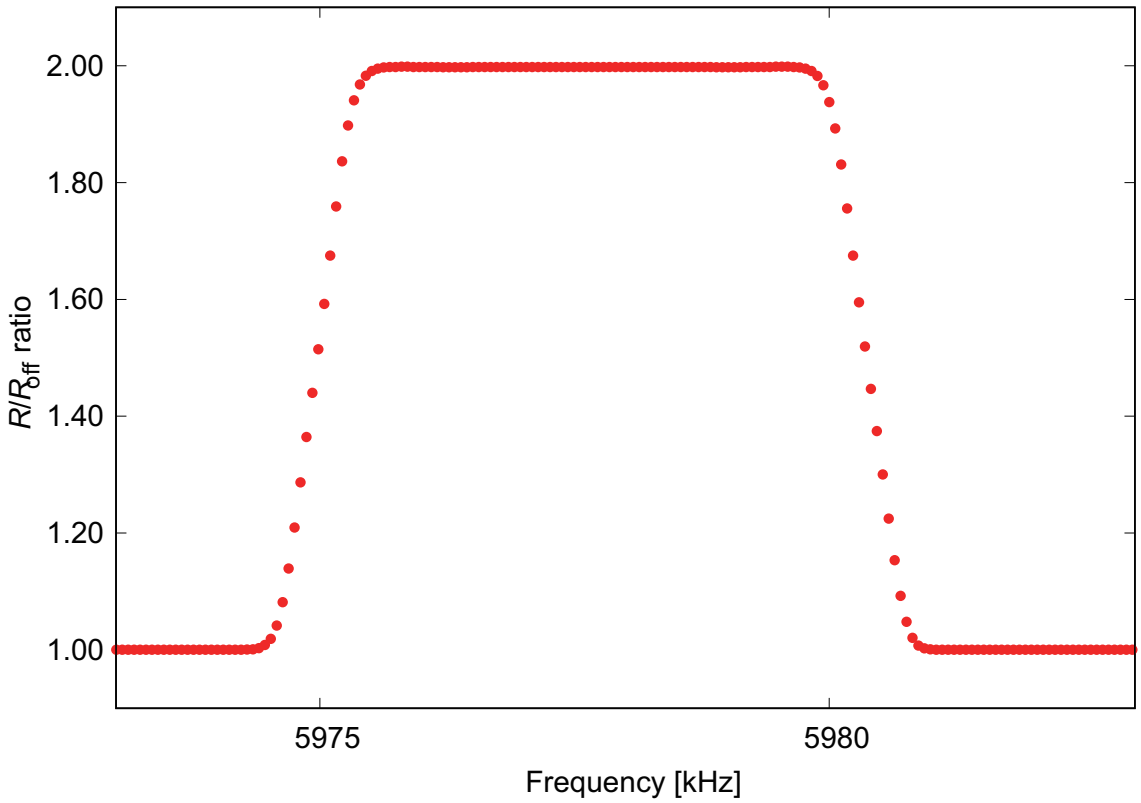

Figure C.2: Results of AFP simulation of ^{21}F

By fitting the simulation results with $f_{\mathrm{AFP}}(x)$, we determined the values of σ_{AFP} and Δx. The results are shown in Fig. C.3 and Table C.2.

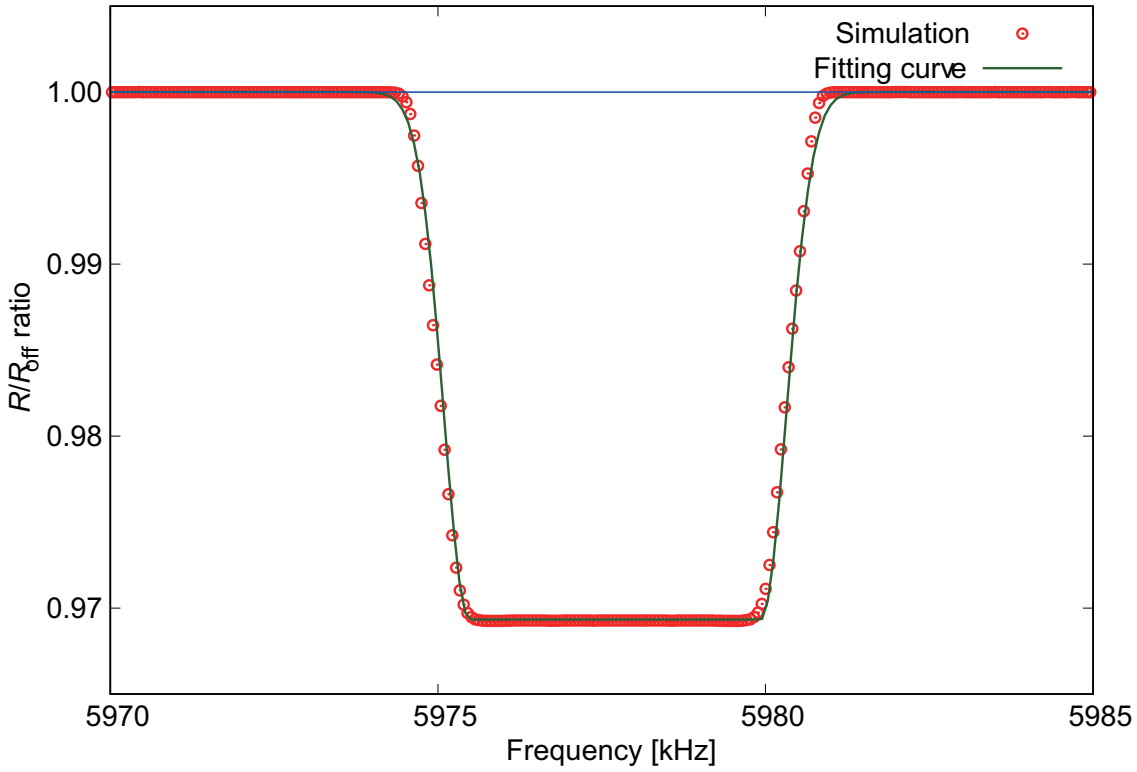

Figure C.3: Results of simulation fitting

Table C.2: Results of simulation fitting

Δx	4.4484 ± 0.2799
σ_{AFP}	0.3917 ± 0.1120

Then, σ_{AFP} and Δx were fixed, and the experimental data were fitted with $F_{\mathrm{AFP}}(x)$. The results are shown in Figs. C.4 and Table C.3. Based on the above analysis, the center frequency was obtained as follows:

$$\nu_{\mathrm{L}} = 5978.28 \pm 1.38(\text{statistic error}) \pm 4.45(\text{systematic error}).$$

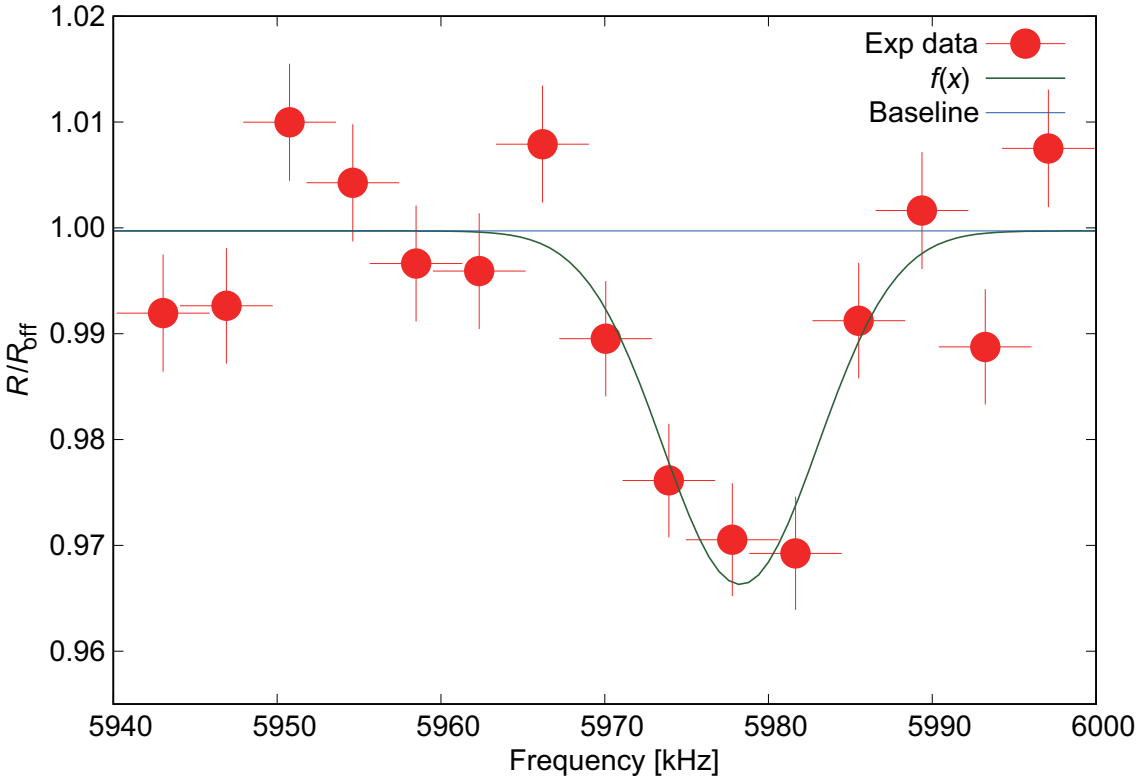

Figure C.4: Results of experimental data fitting

Table C.3: Results of experimental data fitting

A_0	-0.0730 ± 0.01768
X_0	5978.28 ± 1.38
σ_{blur}	4.4482 ± 1.316
Baseline	0.9997 ± 0.0025
reduced χ^2	1.78

Appendix D

The circuit of the data acquisition system

Figures D.1–D.3 show the circuit diagrams with the data acquisition system. The U1PMT–U3PMT and D1PMT–D3PMT denote the photo-multiplier tubes attached to the each plastic scintillators located above and below the stopper.

Tables D.1 and D.2 show the signals output from the TTL signal output ports of PSG for AFR and β-NMR, respectively.

Table D.1: PSG output port allocation table used for AFR measurement.

Output ch	State control
1	Beam gate
2	B_0 sweep gate
3	Count gate
4	Spin Up
5	B_0 Up
6	nop
7	Rotation request

Table D.2: PSG output port allocation table used for AFP-NMR measurement.

Output ch	State control
1	Beam gate
2	RF trigger
3	Count gate
4	RF jump
5	SW jump
6	SW increment
7	nop
8	nop
9	RF ID1
10	RF ID2
11	RF ID3
12	RF ID4
13	nop
14	nop
15	nop
16	nop

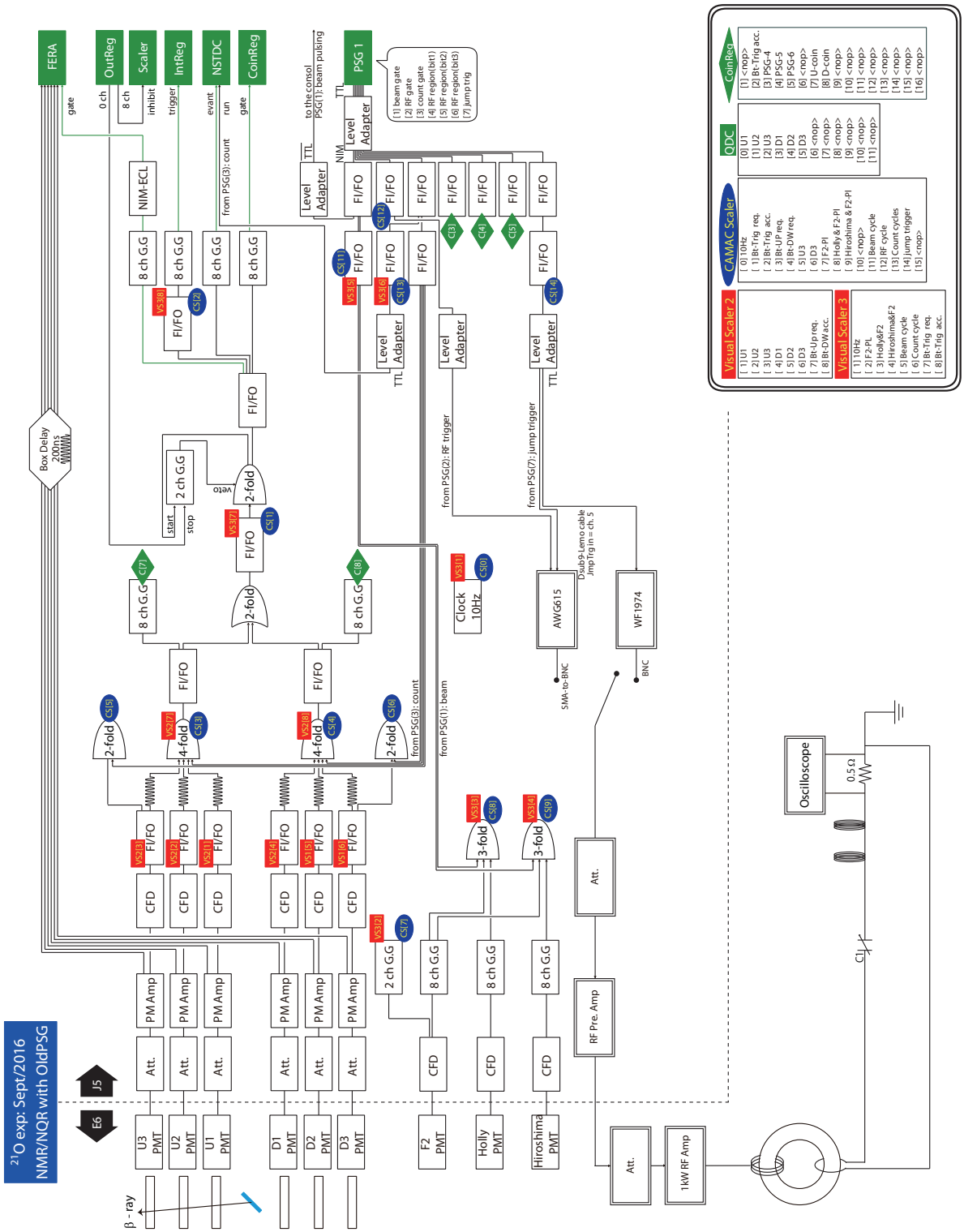

Figure D.1: The circuit of the data collection system for AFP measurement using conventional PSG

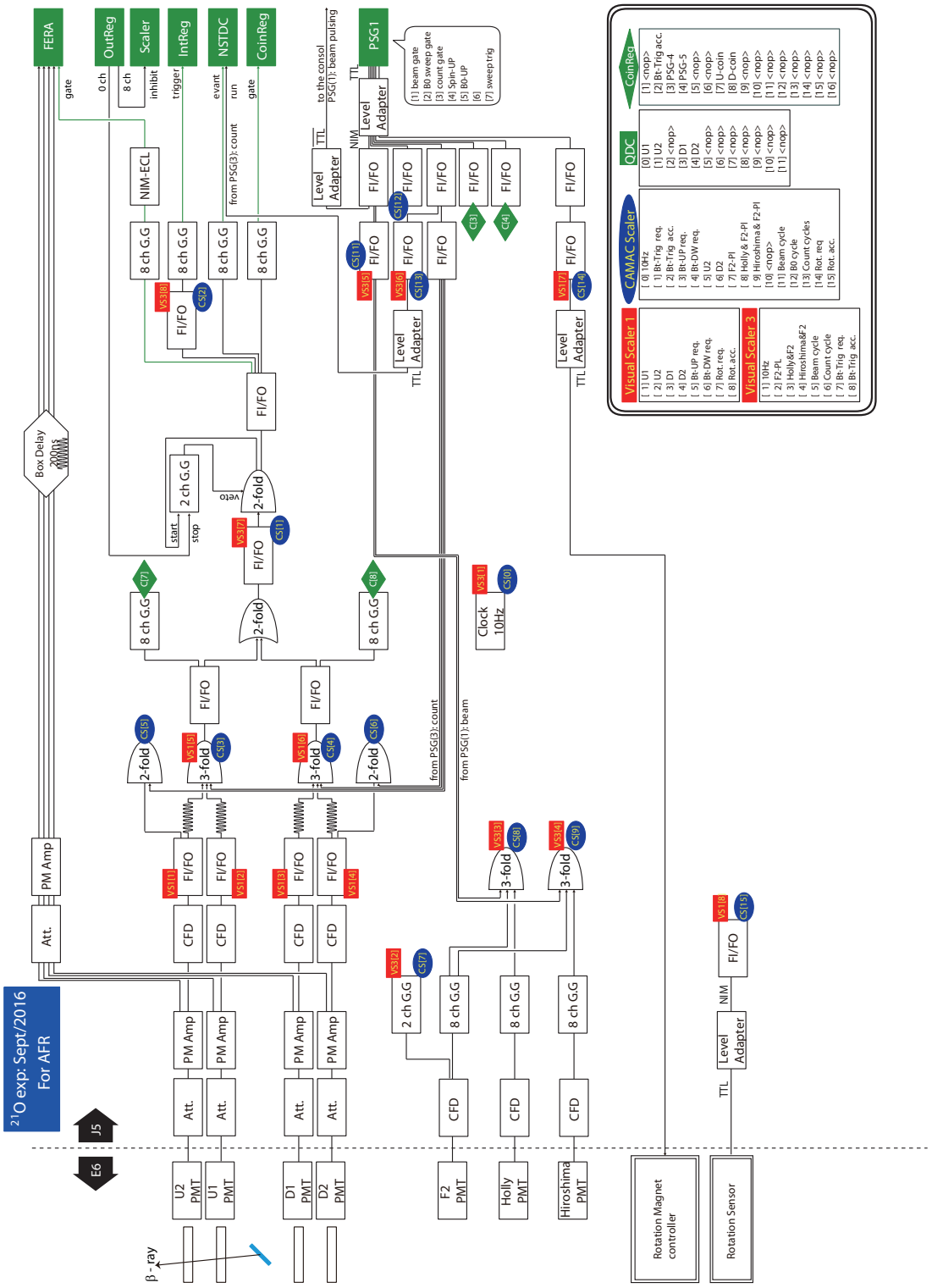

Figure D.2: The circuit of the data collection system for AFR measurement

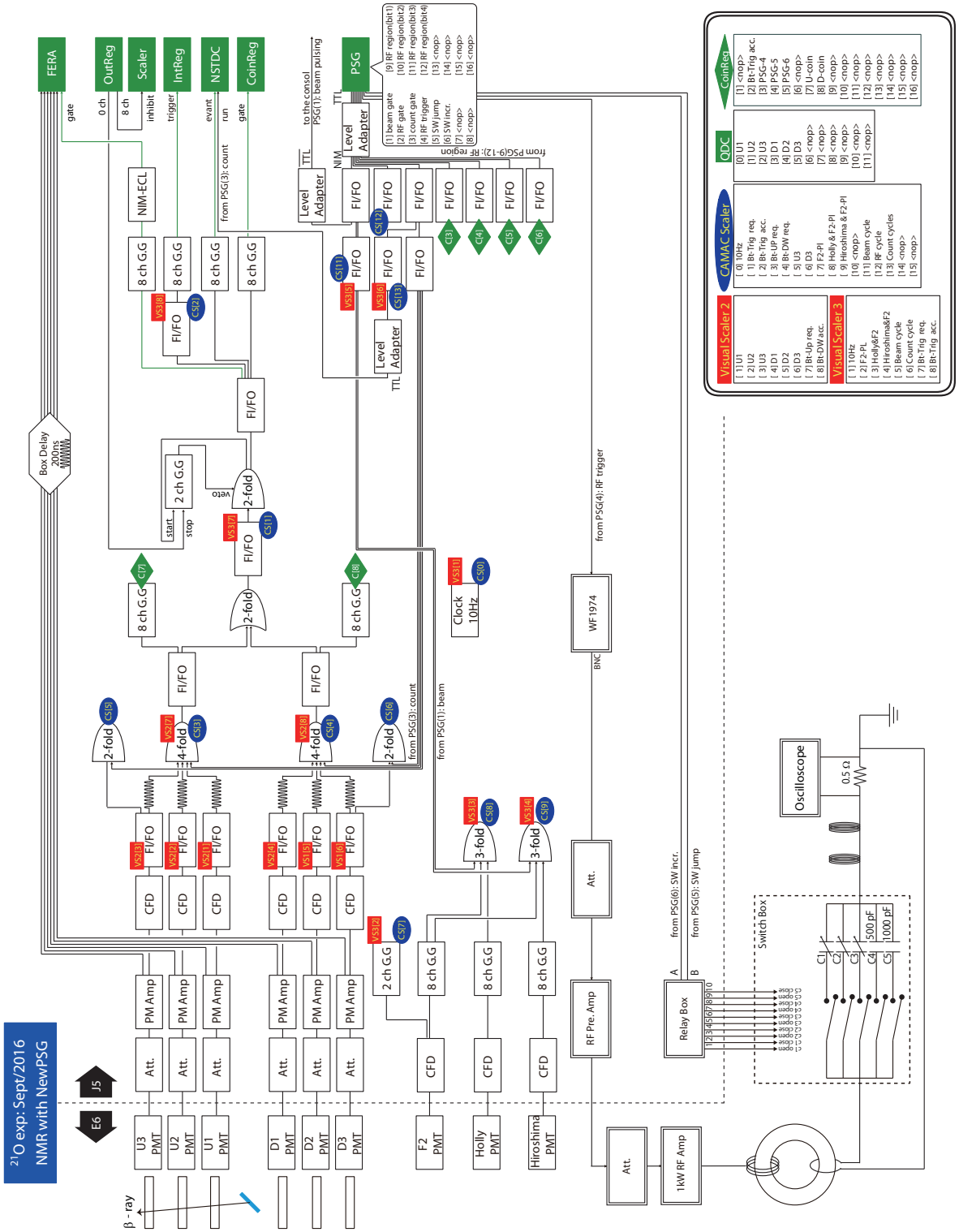

Figure D.3: The circuit of the data collection system for AFP measurement

References

[1] http://www.riken.jp/en/pr/press/2013/20131120_1/

[2] A. Ozawa, T. Kobayashi, T. Suzuki, K. Yoshida, and I. Tanihata, Phys. Rev. Lett. **84** (2000) 5493

[3] D. Steppenbeck, S. Takeuchi, N. Aoi, P. Doornenbal, M. Matsushita, H. Wang, H. Baba, N. Fukuda, S. Go, M. Honma, J. Lee, K. Matsui, S. Michimasa, T. Motobayashi, D. Nishimura, T. Otsuka, H. Sakurai, Y. Shiga, P.-A. SÃűderstrÃűm, T. Sumikama, H. Suzuki, R. Taniuchi, Y. Utsuno, J. J. Valiente-DobÃşn and K. Yoneda, Nature **502** (2013) 207

[4] H. Sakurai, S.M. Lukyanov, M. Notani, N. Aoi, D. Beaumel, N. Fukuda, M. Hirai, E. Ideguchi, N. Imai, M. Ishihara, H. Iwasaki, T. Kubo, K. Kusaka, H. Kumagai, T. Nakamura, H. Ogawa, Yu.E. Penionzhkevich, T. Teranishi, Y.X. Watanabe, K. Yoneda and A. Yoshida, Phys. Lett. B **448** (1999) 180

[5] B. H. Wildenthal, Prog. Part. Nucl. Phys. **11**, (1984) 5.

[6] B. A. Brown and W. A. Richter, Phys. Rev. C **74** (2006) 034315

[7] Y. Utsuno, T. Otsuka, T. Mizusaki, and M. Honma, Phys. Rev. C **60** (1999) 054315

[8] Z. Elekes, Zs. Dombradi, N. Aoi, S. Bishop, Zs. Fulop, J. Gibelin, T. Gomi, Y. Hashimoto, N. Imai, N. Iwasa, H. Iwasaki, G. Kalinka, Y. Kondo, A. A. Korsheninnikov, K. Kurita, M. Kurokawa, N. Matsui, T. Motobayashi, T. Nakamura, T. Nakao, E. Yu. Nikolskii, T. K. Ohnishi, T. Okumura, S. Ota, A. Perera, A. Saito, H. Sakurai, Y. Satou, D. Sohler, T. Sumikama, D. Suzuki, M. Suzuki, H. Takeda, S. Takeuchi, Y. Togano, and Y. Yanagisawa, Phys. Rev. Lett. **98** (2007) 102502

[9] C. R. Hoffman, T. Baumann, D. Bazin, J. Brown, G. Christian, P. A. DeYoung, J. E. Finck, N. Frank, J. Hinnefeld, R. Howes, P. Mears, E. Mosby, S. Mosby, J. Reith, B. Rizzo, W. F. Rogers, G. Peaslee, W. A. Peters, A. Schiller, M. J. Scott, S. L. Tabor, M. Thoennessen, P. J. Voss, and T. Williams, Phys. Rev. Lett. **100** (2008) 152502

[10] M. Fauerbach, D. J. Morrissey, W. Benenson, B. A. Brown, M. HellstrÃűm, J. H. Kelley, R. A. Kryger, R. Pfaff, C. F. Powell, and B. M. Sherrill, Phys. Rev.C **53** (1996) 647

[11] A. Ozawa, O. Bochkarev, L. Chulkov, D. Cortina, H. Geissel, M. HellstrÃűm, M. Ivanov, R. Janik, K. Kimura, T. Kobayashi, A.A. Korsheninnikov, G. MÃijnzenberg, F. Nickel, Y. Ogawa,
A.A. Ogloblin, M. PfÃijtzner, V. Pribora, H. Simon, B. SitÃąr, P. Strmen, K. SÃijmmerer, T. Suzuki, I. Tanihata, M. Winkler, and K. Yoshida, Nucl. Phys. A **691** (2001) 599

[12] R. Kanungo, A. Prochazka, M. Uchida, W. Horiuchi, G. Hagen, T. Papenbrock, C. Nociforo, T. Aumann, D. Boutin, D. Cortina-Gil, B. Davids, M. Diakaki, F. Farinon, H. Geissel, R. Gernhauser, J. Gerl, R. Janik, ÃŸ. Jensen, B. Jonson, B. Kindler, R. Knobel, R. Krucken, M. Lantz, H. Lenske, Y. Litvinov, B. Lommel, K. Mahata, P. Maierbeck, A. Musumarra, T. Nilsson, C. Perro, C. Scheidenberger, B. Sitar, P. Strmen, B. Sun, Y. Suzuki, I. Szarka, I. Tanihata, H. Weick and M. Winkler Phys. Rev. C **84** (2011) 061304(R)

[13] K. Asahi, M. Ishihara, N. Inabe, T. Ichihara, T. Kubo, M. Adachi, H. Takanashi, M. Kouguchi, M. Fukuda, D. Mikolas, D.J. Morrissey, D. Beaumel, T. Shimoda, H. Miyatake, N. Takahashi, Phys. Lett. B **251** (1990) 488.

[14] A. S. Goldhabor, Phys. Lett. B **53** (1974) 306

[15] G. A. Souliotis, D. J. Morrissey, N. A. Orr, B. M. Sherrill, and J. A. Winger, Phys. Rev. C **46** (1992) 1383

[16] K. Turzo, P. Himpe, D. L. Balabanski, G. Belier, D. Borremans, J. M. Daugas, G. Georgiev, F. de Oliveira Santos, S. Mallion, I. Matea, G. Neyens, Yu. E. Penionzhkevich, Ch. Stodel, N. Vermeulen, and D. Yordanov, Phys. Rev. C **73** (2006) 044313.

[17] D. Bazin, O. Tarasov, M. Lewitowicz, O. Sorlin, Nucl. Instrum. Methods Phys. Res. A **482** (2002) 307.

[18] D. E. Groh, P. F. Mantica, A. E. Stuchbery, A. Stolz, T. J. Mertzimekis, W. F. Rogers, A. D. Davies, S. N. Liddick, and B. E. Tomlin, Phys. Rev. Lett. **90** (2003) 202502

[19] A. Abragam. The principle of nuclear magnetism, claredon, oxford,.(1961)

[20] N. Bloembergen, Physica **15** (1949) 386.

[21] T. Minamisono, Hyperfine interactions **35** (1987) 979.

[22] J. H. Van Vleck, Phys. Rev **74** (1948) 1168.

[23] F. D. Feiock, W. R. Johnson, Phys. Rev. Lett. **21** (1968) 785.

[24] K. Sugimoto, A. Mizobuchi, K. Nakai and K. Matuda, Phys. Lett. **18** (1965) 38.

[25] T. Minamisono, T. Ohtsubo, I. Minami, S. Fukuda, A. Kitagawa, M. Fukuda, K. Matsuta, Y. Nojiri, S. Takeda, H. Sagawa, and H. Kitagawa, Phys. Rev. Lett. **69** (1992) 2058

[26] T. D. Lee and C. N. Yang, Phys. Rev. **104**, (1956) 254.

[27] R. B. Firestone, Nuclear Data Sheets **127** (2015) 1.

[28] R. Brun, F. Carminati, CERN Application Software Group, geant3.2, CERN Program Library, Writeup Report No. W5013, 1994.

[29] H. Ogawa, K. Asahi, K. Sakai, A. Yoshimi, M. Tsuda, Y. Uchiyama, T. Suzuki, K. Suzuki, N. Kurokawa, M. Adachi, H. Izumi, H. Ueno, T. Shimoda, S. Tanimoto, N. Takahashi, W.-D. Schmidt-Ott, M. SchÃďfer, S. Fukuda, A. Yoshida, M. Notani, T. Kubo, H. Okuno, H. Sato, N. Aoi, K. Yoneda, H. Iwasaki, N. Fukuda, N. Fukunishi, M. Ishihara, and H. Miyatake, Phys. Lett. B **451** (1999) 11.

[30] http://www.comcraft.co.jp/products/kilovac/k40p.html

[31] N-RL 200 Programed Sequence Generator, Technoland Co. Ltd., Tokyo, Japan.

[32] N. Yoshida, Master thesis. Department of physics, Tokyo Institute of technology. (20013)

[33] Y. Ishibashi, N. Yoshida, H. Ueno, A. Yoshimi, Y. Ichikawa, Y. Abe, K. Asahi, M. Chikamori, T. Fujita, T. Furukawa, E. Hikota, D. Nagae, Y. Ohtomo, Y. Saito, H. Shirai, T. Suzuki, X.F. Yang, and N. Sakamoto, Nucl. Instr. Meth. B **317** (2013) 714.

[34] H. Okamura, H. Sakai, N. Sakamoto, T. Uesaka, S. Ishida, H. Otsu, T. Wakasa, K. Hatanaka, T. Kubo, N. Inabe, K. Ikegami, J. Fujita, M. Kase, A. Goto, and Y. Yano, AIP Conf. Proc. **293**, 84 (1993).

[35] K. Matsuta, Y. Tagishi, T. Nagatomo, A. Ozawa, M. Yamaguchi, H. Fujiwara, T. Yasuno, A. Chiba, R. Matsumiya, M. Mihara, M. Fukuda, K. Minamisono and T. Minamisono, Uttac **73** (2005)14

[36] N. Yoshida, H. Ueno, A. Yoshimi, Y. Ishibashi, Y. Ichikawa, Y. Abe, K. Asahi, M. Chikamori, T. Fujita, T. Furukawa, E. Hikota, D. Nagae, Y. Ohtomo, Y. Saito, H. Shirai, T. Suzuki, and X.F. Yang, Nucl. Instr. Meth. B **317** (2013) 705.

[37] K. Halbach, Nucl. Instrum. Meth. **169** (1980) 1

[38] K. Matsuta, T. Onishi, M. Fukuda, T. Minamisono, H. Akai, M. Sasaki, T. Yamaguchi, T. Miyake, K. Sato, K. Minamisono, F. Ohsumi, Y. Muramoto, S. Oui, C. Ha, K. Tanaka, K. Kidera, A. Morishita, A. Kitagawa, M. Torikoshi, M. Kanazawa, T. Nishio, S. Koda, T. Ohtsubo, S. Fukuda, Y. Nojiri, S. Momota, A. Ozawa, K. Yoshida, T. Suzuki,

T. Kobayashi, I. Tanihata, S.S. Hanna, J.R. Alonso, G.F. Krebs, and T.J.M. Symons, Hyperfine Interactions **120/121** (1999) 673

[39] T. Kubo, M. Ishihara, N. Inabe, H. Kumagai, I. Tanihata, K. Yoshida, T. Nakamura, H. Okuno, S. Shimoura, and K. Asahi, Nucl. Instr. Meth. B **70** (1992) 309.

[40] http://lise.nscl.msu.edu/lise.html

[41] K. Matsuta, T. Minamisono, M. Tanigaki, M. Fukuda, Y. Nojiri, M. Mihara, T. Onishi, T. Yamaguchi, A. Harada, M. Sasaki, T. Miyake, K. Minamisono, T. Fukao, K. Sato, Y. Matsumoto, T. Ohtsubo, S. Fukuda, S. Momota, K. Yoshida, A. Ozawa, T. Kobayashi, I. Tanihata, J. R. Alonso, G. F. Krebs and T. J. M. Symons, Hyperfine Interactions **97/98** (1996) 519.

[42] T. Minamisono, Y. Nojiri, K. Matsuta, M. Fukuda, K. Sato, M. Tanigaki, A. Morishita, T. Miyake, Y. Matsumoto, T. Onishi, K. Ishiga, F. Ohsumi, H. Kitagawa, and H. Sagawa, Phys. Lett. B **457** (1999) 9

[43] D. Nagae, PhD thesis. Department of physics, Tokyo Institute of technology. (2007)

[44] C.J.Jameson, in: Nucl. Mag. Res., Vol. 12, Specialist Periodical Reports (Royal Chemical Society, London, 1983)

[45] G.L. Turner, S.E. Chung, and E. Oldfield, J. Mag. Res **64** (1985) 316

[46] T. Nakamura, N. Fukuda, T. Kobayashi, N. Aoi, H. Iwasaki, T. Kubo, A. Mengoni, M. Notani, H. Otsu, H. Sakurai, S. Shimoura, T. Teranishi, Y. X. Watanabe, K. Yoneda, M. Ishihara, Phys. Rev. Lett. **83**, 1112 (1999).

[47] W. N. Catford, L. K. Fifield, N. A. Orr, C. L. Woods Nucl. Phys. A **503**, 263 (1989).

[48] M. Stanoiu, F. Azaiez, Zs. Dombrádi, O. Sorlin, B. A. Brown, M. Belleguic, D. Sohler, M. G. Saint Laurent, M. J. Lopez-Jimenez, Y. E. Penionzhkevich, G. Sletten, N. L. Achouri, J. C. Angélique, F. Becker, C. Borcea, C. Bourgeois, A. Bracco, J. M. Daugas, Z. Dlouhý, C. Donzaud, J. Duprat, Zs. Fülöp, D. Guillemaud-Mueller, S. Grévy, F. Ibrahim, A. Kerek, A. Krasznahorkay, M. Lewitowicz, S. Leenhardt, S. Lukyanov, P. Mayet, S. Mandal, H. van der Marel, W. Mittig, J. Mrázek, F. Negoita, F. De Oliveira-Santos, Zs. Podolyák, F. Pougheon, M. G. Porquet, P. Roussel-Chomaz, H. Savajols, Y. Sobolev, C. Stodel, J. Timár, A. Yamamoto, Phys. Rev. C **69**, 034312 (2004).

[49] E. Sauvan, F. Carstoiu, N. A. Orr, J. S. Winfield, M. Freer, J. C. Angélique, W. N. Catford, N. M. Clarke, N. Curtis, S. Grévy, C. Le Brun, M. Lewitowicz, E. Liégard, F. M. MarquÃľs, M. Mac Cormick, P. Roussel-Chomaz, M.-G. Saint Laurent, M. Shawcross, Phys. Rev. C **69**, 044603 (2004).

[50] B. Fernández-Domínguez, J. S. Thomas, W. N. Catford, F. Delaunay, S. M. Brown, N. A. Orr, M. Rejmund, M. Labiche, M. Chartier, N. L. Achouri, H. Al Falou, N. I. Ashwood, D. Beaumel, Y. Blumenfeld, B. A. Brown, R. Chapman, N. Curtis, C. Force, G. de France, S. Franchoo, J. Guillot, P. Haigh, F. Hammache, V. Lapoux, R. C. Lemmon, F. Maréchal, A. M. Moro, X. Mougeot, B. Mouginot, L. Nalpas, A. Navin, N. Patterson, B. Pietras, E. C. Pollacco, A. Leprince, A. Ramus, J. A. Scarpaci, N. de Séréville, I. Stephan, O. Sorlin, G. L. Wilson, Phys. Rev. C **84**, 011301(R) (2011).

[51] Evaluated Nuclear Structure Data File Search and Retrieval (ENSDF), `https://www.nndc.bnl.gov/ensdf/`.

[52] A. Arima, K. Shimizu, W. Bentz, and H. Hyuga, Adv. Nucl. Phys. **18**, 1 (1987).

[53] I.S. Towner, Phys. Rep. **155**, 263 (1987).

[54] B.A. Brown and B.H. Wildenthal, Nucl. Phys. A **474**, 290 (1987).

[55] F. Alder and F. C. Yu Phys. Rev. **81**, 1067 (1951).

[56] N. Shimizu, "Nuclear shell-model code for massive parallel computation KSHELL", arXiv:1310.5431 [nucl-th] (2013).

[57] E. K. Warburton, J.A. Becker, B. A. Brown, Phys. Rev. C **41** (1990) 1147.

[58] H. Noya, A. Arima and H. Horie, Suppl. Prog. Theor. Phys. **8**, 33 (1958).

[59] Y. Utsuno *et al.*, Phys. Rev. C **60** (1999) 054315.

[60] G. Co', V. De Donno, M. Anguiano, R. N. Bernard, A. M. Lallena, Phys. Rev. C **92**, 024314 (2015).

[61] J. F. Berger, M. Girod, D. Gogny, Comput. Phys. Commun. **63**, 365 (1991).

[62] S. Goriely, S. Hilaire, M. Girod, S. Péru, Phys. Rev. Lett. **102**, 242501 (2009).